Jumping Silicon Microrobots With Electrostatic Inchworm Motors and Energy Storing Substrate Springs

by

Craig Schindler

A dissertation submitted in partial satisfaction of the

requirements for the degree of

Doctor of Philosophy

in

Engineering – Electrical Engineering and Computer Sciences

in the

Graduate Division

of the

University of California, Berkeley

Committee in charge:

Professor Kristofer S. J. Pister, Chair
Professor Ming C. Wu
Professor Sanjay Govindjee

Spring 2020

Jumping Silicon Microrobots With Electrostatic Inchworm Motors and Energy Storing Substrate Springs

Abstract

Jumping Silicon Microrobots With Electrostatic Inchworm Motors and Energy Storing Substrate Springs

by

Craig Schindler

Doctor of Philosophy in Engineering – Electrical Engineering and Computer Sciences

University of California, Berkeley

Professor Kristofer S. J. Pister, Chair

Jumping microrobots are a burgeoning area of autonomous microelectromechanical systems (MEMS). This dissertation presents background, theory, designs, and results of the first jumping microrobots fabricated in a silicon-on-insulator (SOI) process using electrostatic inchworm motors etched into the device layer silicon and energy storing springs etched into the silicon substrate. Substrate silicon is much thicker than device layer silicon, and can therefore store a lot more mechanical energy per unit area than can device layer silicon. New high force density electrostatic inchworm motors designed to stretch and store energy in substrate springs are presented.

The first ever SOI robot to use electrostatic inchworm motors to store energy in a substrate spring is presented. While this robot was unable to use its electrostatic inchworm motors to store enough energy to jump, it was able to store enough energy to kick both a 0.6 milligram 0402 capacitor and a 2.5 gram mass (which weighed more than 25 times that of the robot). Additionally, the robot was able to vertically jump 4cm when its substrate spring was manually compressed with tweezers. A redesigned robot is then presented which used its on-board electrostatic inchworm motor to store energy in its substrate spring and vertically jump 3.6mm. To date, this is the highest jumping SOI based microrobot as well as the only one to store mechanical energy in substrate silicon.

Finally, steps towards integration of the robot with a CMOS brain and high voltage solar cells for full autonomy is presented, along with design improvements needed to achieve a one meter high vertical jump.

To Allen and Henry,
For giving me the strength to do anything and teaching me to never stop questioning.

Contents

List of Figures

List of Tables

Acknowledgments

Thank you to my advisor, Kristofer Pister, for letting me work on microrobots, and a myriad of other fun research topics. I have learned a tremendous amount, both technical and non-technical, under your tutelage.

Thank you to the members of my qualifying exam and dissertation committees, Ana Arias, Ming Wu, and Sanjay Govindjee.

Thank you to the Pister Group members who came before me, and for mentoring me in my early days of graduate school: Travis Massey, Joey Greenspun, Dan Contreras, Dan Drew, David Burnett, Brad Wheeler, and Fil Maksimovic.

Thank you to Hani Gomez and Brian Kilberg, my fellow Pister Group members who have been on this journey with me since Day One. Thank you for being amazing friends and colleagues. I am forever grateful that we were able to experience and navigate the highs and lows and the successes and failures of graduate school together.

Thank you to the next crop of Pister Group members: Nathan Lambert, Alex Moreno, Lydia Lee, Dillon Acker-James, and Daniel Teal. It has been a pleasure working with you all and I hope that I have been of help to you as you began your graduate school journeys.

Thank you, Thomas Watteyne, for mentoring me from afar during my early days of graduate school.

Thank you to my undergraduate researchers over the years: Felipe, Ahad, Arvind, Alex, James, Dinesh, and Arjun. I learned so much from you, and I hope you learned something from me.

Thank you to the staff and members of the Marvell Nanofabrication Laboratory for your endless help with my research.

Thank you to the BSAC and EECS Department staffs, for being helpful and supportive at every stage of my graduate school experience.

Thank you to my grandfathers for igniting a spark of curiosity within me, and for cultivating and nurturing my love of science.

Thank you, Mom, Dad, and Dana, for always supporting me in all my endeavors, and for being the best parents and sister anyone could ever ask for.

Thank you to all my family and friends, both near and far.

Thank you, Beth, for going on the roller coaster journey of graduate school with me, and for always being there for me. I couldn't ask for a better partner-in-crime.

Chapter 1

Background and State of the Art

1.1 What Are Microrobots and Why Make Them Jump?

Robots are all around us. They manufacture widgets in factories, assist surgeons, clean our homes, and help us explore space, just to name a few. While there are many definitions of microrobots, for the purpose of this dissertation they are defined as millimeter to centimeter scale robots with critical dimensions down to the micrometer scale. Because microrobots are small, they have the potential to explore hard to reaches places that traditional larger robots cannot, as well as consume less power. Additionally, if they can be batch fabricated (i.e. many can be made at the same time) then they have the potential to be significantly less expensive than traditional robots. Finally, small robots have the potential to work together as swarms, and work in large groups like ant and termite colonies do; while a single microrobot may not be very useful by itself, tens, thousands, or even millions of them can potentially accomplish very difficult and complicated tasks [1, 2, 3, 4, 5, 6]. Potential use cases for microrobots are manufacturing, disaster recovery, artificial pollination, search and rescue, space exploration, and internal medicine, just to name a few [7, 8, 9, 10]. Research efforts thus far have pushed forward the frontiers of many microrobot locomotion modalities such as jumping [11, 12, 13, 14, 15, 16], walking [17, 18, 19, 20, 21, 22], and flying [23, 24, 25, 26].

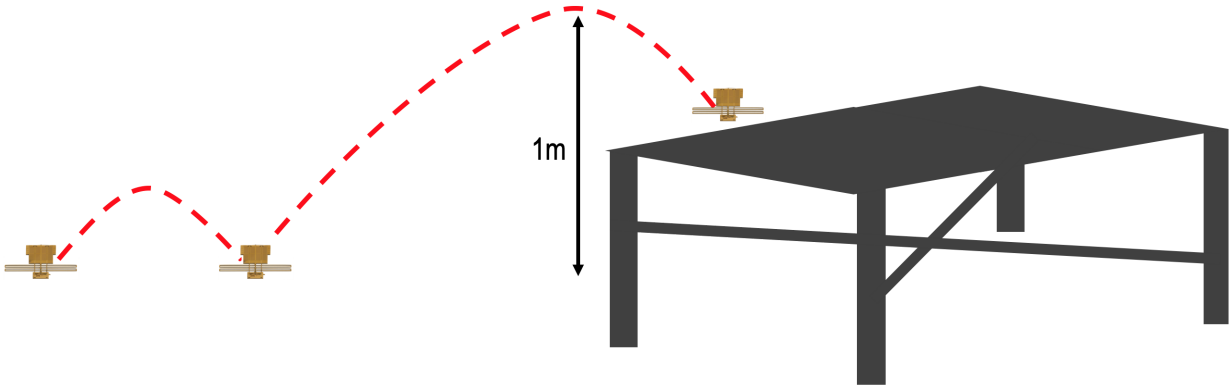

Figure 1.1: A microrobot [16] hypothetically jumping 1m onto a table.

Jumping is a locomotion modality which would allow microrobots to traverse terrain that may not be possible by walking — fleas and crickets do this in the natural world [27, 28, 29, 30, 31]. This dissertation presents work towards developing autonomous jumping microrobots. The microrobot platform presented was developed with the explicit goal of being able to vertically jump 1m. Fig. 1.1 shows a microrobot [16] hypothetically jumping 1m into the air and landing on a table. Getting from the floor to the top of a table is a task that is much easier to do by jumping rather than walking, and much less energy intensive than flying. Additionally, it is an example task that might be a common everyday occurrence in a world filled with microrobots.

1.2 Previous Work on Jumping Microrobots

The ideal jumping microrobot can be made using batch fabrication in a standard process, has integrated motors and mechanisms, and consumes only a small amount of power so that it can survive on scavenged energy. An autonomous microrobot with 1cm^2 of solar cells in direct sunlight would receive approximately 100mW of incident power [32]. Assuming 20% efficiency from solar energy to electrical energy, the robot would be able to harness 20mW of power. If the robot needs to operate in darkness or other secluded areas, it also needs to store the energy it receives. Recent state of the art thin film batteries (with thicknesses on the order of hundreds of μm) are able to store $6.98\frac{\text{mWh}}{\text{cm}^2}$ [33]. The difficulty of storing large amounts of energy at the small scale necessitates the need for actuators that consume very little power, ideally on the order of 1mW or less. For example, if a robot has 1cm^2 of a battery capable of storing $6.98\frac{\text{mWh}}{\text{cm}^2}$, then after approximately 20 minutes in the sun the battery will have stored enough energy to run an actuator consuming 1mW for approximately 7 hours. This will allow the robot to move and actuate for a significant portion of the day without requiring any light source at all. Chapter 3 presents low power electrostatic actuators that consume less than 1mW and provide 15mN of force.

One of the first attempts at making a silicon based jumping microrobot used electrostatic inchworm motors made in the device layer of a silicon on insulator (SOI) process, and custom built micro rubber bands to store energy for jumping [11]. The robot and micro rubber bands had to be assembled together manually, rendering full batch fabrication impossible. The robot was never able to jump on its own using its motors, but was able to store enough energy to kick a 0.6mg 0402 capacitor. A similar follow-up design then used a silicon skeleton with PDMS energy storing springs [12]. This made batch fabrication possible, but the PDMS deposition required fabrication steps not found in a standard process. While the robot was able to store 100μJ of energy, it did not have any integrated motors or mechanisms and could only jump if energy was stored in the springs manually by a human.

Noh et al. created a jumping microrobot using shape memory alloy [13] which had an elastic energy to kinetic energy efficiency of 26%. While the robot was able to vertically jump 64cm, part of its actuation sequence required 0.6A of current for 15s. This is unfeasible for an autonomous microrobot.

A more recent robot made in a standard SOI process used the device layer silicon for both electrostatic inchworm motors and energy storing springs [14]. When this robot was manually primed with tweezers and electrostatically latched it stored and released 4μJ of energy and vertically jumped 7mm. When it used its onboard electrostatic inchworm motors to store energy it was able to store and release 1μJ of energy and vertically jump 1mm.

A nanoporous silicon based robot [12] jumped with 250μJ of kinetic energy, but was only able to jump one time due to the unrecoverable nature of the depleted onboard chemical energy used to jump.

Finally, a microrobot using an electromagnetic actuator and a laser cut steel spring to store energy was able to jump 8mm but required 6.4mW of power and was fabricated and hand assembled from entirely individually made components [15].

A summary of these microrobots is shown in Table 1.1.

1.3 The Jumping Microrobots in This Dissertation

The jumping microrobots presented in Chapters 4 and 5 of this dissertation follow a similar design principle to the robot in [14] — namely, use a standard fabrication process that allows for batch manufacturing as well as a path towards integration with a power supply [34] and CMOS brain and radio [35]. While both the robot in [14] and the robots in Chapters 4 and 5 use an SOI process, the robot in [14] uses the device layer silicon for motors, mechanisms, and mechanical energy storage, while the robots in Chapters 4 and 5 use the device layer silicon for motors and mechanisms and the *silicon substrate* for energy storage.

Because substrate silicon is so much thicker than device layer silicon it can store significantly more energy per unit area of layout which is crucial for designing springs and motors that meet the energy storage requirements for high vertical jumps. Chapter 2 discusses the details of these springs. High force electrostatic inchworm motors capable of producing 15mN of

Table 1.1: A comparison of different jumping microrobots.

Reference	Batch Fabrication	Standard Process	Energy Storage Method	Stored Energy	Actuation Method [1]	Electrical Input Power	Jump Height
[11]	X	X	Micro Rubber Bands	4.9nJ	EIWM	$<1\mu$W	N/A
[12]	✓	X	PDMS	100μJ	M	N/A	32cm
[12]	X	X	Sodium Perchlorate	250μJ	RH	0.9W	8cm
[13]	X	X	SMA	40mJ	SMA	1W	64cm
[14]	✓	✓	Device Layer Silicon	1μJ 4μJ	EIWM M	30μW N/A	1mm 7mm
[15]	X	X	Steel Spring	11.25μJ	MA	6.4mW	8mm
Chapter 4	✓	✓	Substrate Silicon	0.5μJ 100μJ	EIWM M	30μW N/A	N/A 4cm
Chapter 5	✓	✓	Substrate Silicon	8μJ	EIWM	30μW	3.6mm

[1] EIWM = electrostatic inchworm motor, M = manually by a human, RH = resistive heating, SMA = shape memory alloy, MA = magnetic actuator

force at 100V were designed and fabricated to store energy in substrate springs, the details of which are presented in Chapter 3.

Chapters 4 and 5 then present two different robots that use energy storing substrate springs and high force electrostatic inchworm motors to store energy and jump. The robot in chapter Chapter 4 was the first SOI based robot to use electrostatic inchworm motors to store energy in a substrate spring. While unable to store enough energy and jump on its own, it was able to store enough energy using its motors to kick a 2.5 gram mass (more than 25 times the mass of the robot) a distance of 80μm and kick a 0.6 gram mass a distance of 7mm. The robot was also able to vertically jump 4cm when its substrate spring was manually compressed with tweezers. Chapter 5 presents a redesigned robot which was able to store enough energy in its substrate spring using its electrostatic inchworm motor to vertically jump 3.6mm, more than tripling the previous vertical jump height of an SOI based microrobot [14]. A summary of the robots presented in this dissertation are also summarized in Table 1.1.

1.4 The Advantages of a Standard Process

While there are many microrobots fabricated using custom or exotic processes, or even fabricated by hand, standard processes allow designers to focus on design, without worrying about the minutiae of the process. This model has been extremely successful in the world of integrated circuits, where designers are given design rules by a foundry, and as long as they follow the design rules, they can expect to receive back fabricated devices that exactly match their designs. This model allows for iterative designs, without worry about how the process will change from run to run. A silicon-on-insulator process is an example of such a standard process for MEMS. For example, the SOIMUMPS [36] service by MEMSCAP Inc. uses four masks and is run four times every year. Motors, mechanisms, linkages, and energy storage elements can all be made in an SOI process, allowing for very complicated designs to be realized with only a few masks. Additionally, commerical SOI processes are used to make CMOS [37], potentially providing a convergent process for making CMOS and MEMS in the same process [38]. While commercial standard processes such as SOIMUMPS exist, all fabrication for the work in this dissertation was completed in the Marvell Nanofabrication Laboratory on the University of California, Berkeley campus. The flow for the SOI process used is in this dissertation is explained in Section 1.5 and the details are shown in Appendix A.

1.5 The Three Mask SOI Process Used In This Dissertation

The three mask process used in this dissertation is summarized in Fig. 1.2 and consists of four major fabrication steps. The process begins with an SOI wafer with a 40μm single crystal silicon device layer, a 2μm buried oxide, and a 550μm silicon substrate. A 50nm

chromium seed layer and 500nm gold layer is then deposited, patterned, and removed via liftoff. Next, the 40μm device layer is patterned and etched using deep reactive ion etching (DRIE). Afterwards, the 550μm substrate is patterned and etched using deep reactive ion etching. Finally, movable structures are released from the buried oxide using a timed vapor hydrofluoric acid etch. The details of the entire process flow are given in Appendix A.

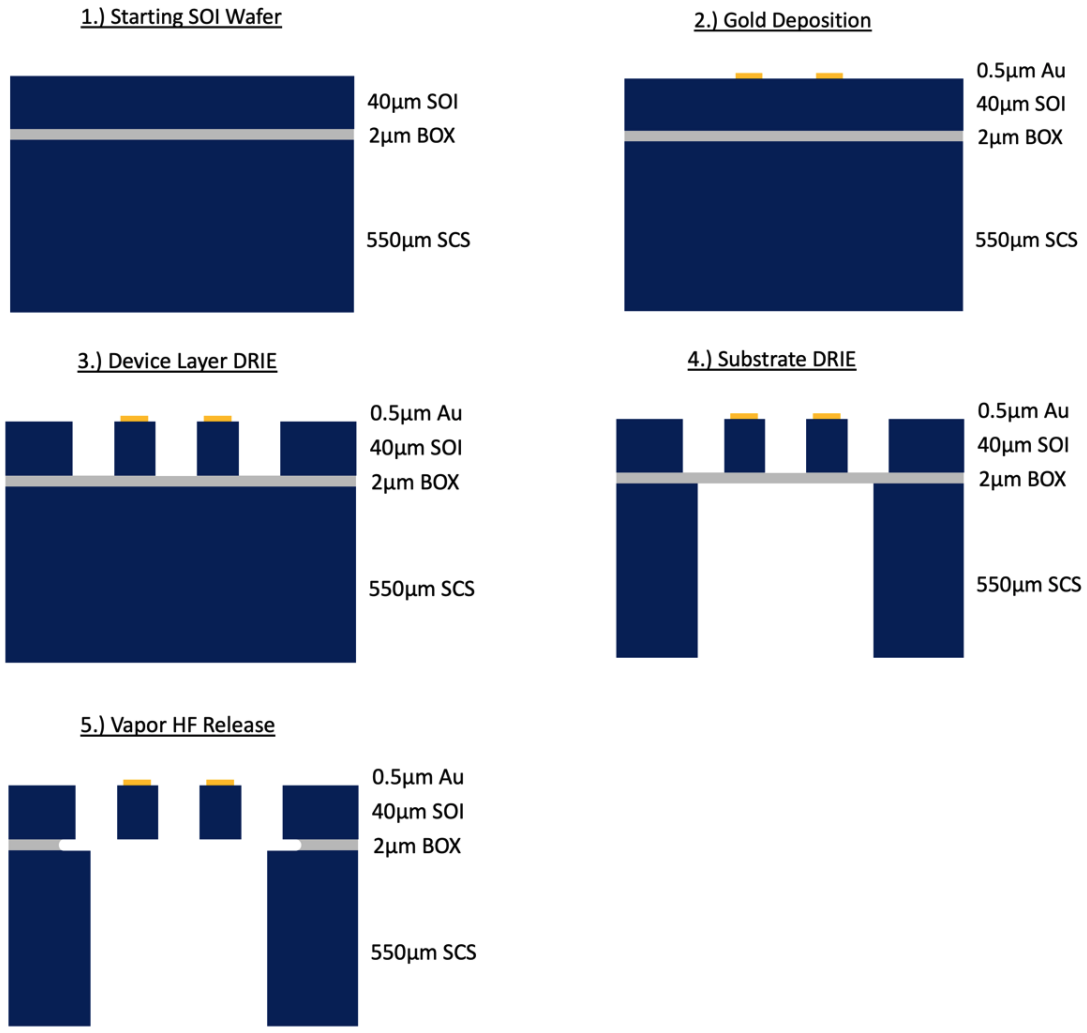

Figure 1.2: The three mask SOI process used in this dissertation. Details of the entire process flow are given in Appendix A.

Chapter 2

Energy Storing Substrate Springs

2.1 The Energy Density of Silicon

A piece of material stretched uni-axially with a Young's modulus E, strain ϵ, and stress $\sigma(\epsilon) = E\epsilon$ has a strain energy density equal to

$$U_d = \int_0^\epsilon \sigma(\epsilon')d\epsilon' = \int_0^\epsilon E\epsilon' d\epsilon' = \frac{1}{2}E\epsilon^2 \quad \left[\frac{\mathrm{J}}{\mathrm{m}^3}\right]. \tag{2.1}$$

While single crystal silicon is known to have a yield strain of up to 3.7% [39], the yield strain ϵ_{max} of single crystal silicon structures fabricated in the SOI process in this dissertation has been measured to be 0.5% [40]. Evaluating the above expression with the Young's modulus of <110> silicon, 169GPa [41], results in a maximum energy density of $2.1\frac{\mathrm{J}}{\mathrm{cm}^3}$. This figure can be compared to other materials, for example resilin ($E = 0.002$GPa and fracture strain $\epsilon_{max} = 1.9$) and high-tensile steel ($E = 200$GPa and fracture strain $\epsilon_{max} = 0.008$), which have a maximum energy density of $3.6\frac{\mathrm{J}}{\mathrm{cm}^3}$ and $6.4\frac{\mathrm{J}}{\mathrm{cm}^3}$, respectively [42]. While these three materials all have energy densities in the same order of magnitude, the ability to micromachine silicon makes it the superior material for building microrobots.

2.2 The Theoretical Maximum Jump Height of Silicon

The maximum theoretical jump height of a piece of silicon in a vacuum stretched to its strain limit ϵ_{max} is given by solving the following equation for height h, where the silicon has volume V, mass m, is subject to standard gravitational acceleration g, and density ρ_{Si}, which is equal to $2300\frac{\mathrm{kg}}{\mathrm{m}^3}$:

$$\frac{1}{2}VE{\epsilon_{max}}^2 = \frac{1}{2}\frac{m}{\rho_{Si}}E{\epsilon_{max}}^2 = mgh. \tag{2.2}$$

With E=169GPa and ϵ_{max}=0.5% the maximum jump height is calculated as

$$h = \frac{E{\epsilon_{max}}^2}{2\rho_{Si}g} = 94\text{m}. \tag{2.3}$$

While achieving this theoretical limit is impractical, the design space for making robots that rival or even beat nature's insects is quite large [27, 28, 29, 30, 31].

2.3 The Maximum Energy Storage in a Cantilever

Cantilevers are commonly used in MEMS design as support structures and energy storage elements because they are easy to fabricate and require less force to bend than uni-axially stretched beams. Cantilever-based springs are what store energy for the jumping microrobots in this dissertation. We can analyze the maximum energy density of a cantilever and compare that with the maximum energy density of a uni-axially strained piece of silicon as shown in Section 2.1.

Using Euler-Bernoulli beam theory [43], the strain ϵ of a beam can be related to the distance z away from the neutral axis, internal bending moment M, Young's modulus E, and moment of inertia I as

$$\epsilon = \frac{zM}{EI}. \tag{2.4}$$

The internal bending moment M is a function of the applied force F at the tip of the cantilever and the distance x away from the cantilever anchor point, and is equal to

$$M = F(L - x). \tag{2.5}$$

The maximum total energy stored in a cantilever is therefore

$$U_{max,cantilever} = \frac{1}{2}E \int_{x=0}^{x=L} \int_{z=-a/2}^{z=a/2} \int_{y=-b/2}^{y=b/2} \epsilon^2 \, dy \, dz \, dx \tag{2.6}$$

$$= \frac{1}{2}E \int_{x=0}^{x=L} \int_{z=-a/2}^{z=a/2} \int_{y=-b/2}^{y=b/2} \left(\frac{zF(L-x)}{EI}\right)^2 dy \, dz \, dx. \tag{2.7}$$

A cantilever such as the one shown in Fig. 2.1 will break when the strain at the top of the beam at the anchor is equal to ϵ_{max}. This occurs when

$$\epsilon_{max} = \frac{aFL}{2EI} \tag{2.8}$$

where ϵ_{max} is the yield strain, a is the height of the cantilever, b is the width of the cantilever, L is the length of the cantilever, F is the force applied to the cantilever (applied transversely

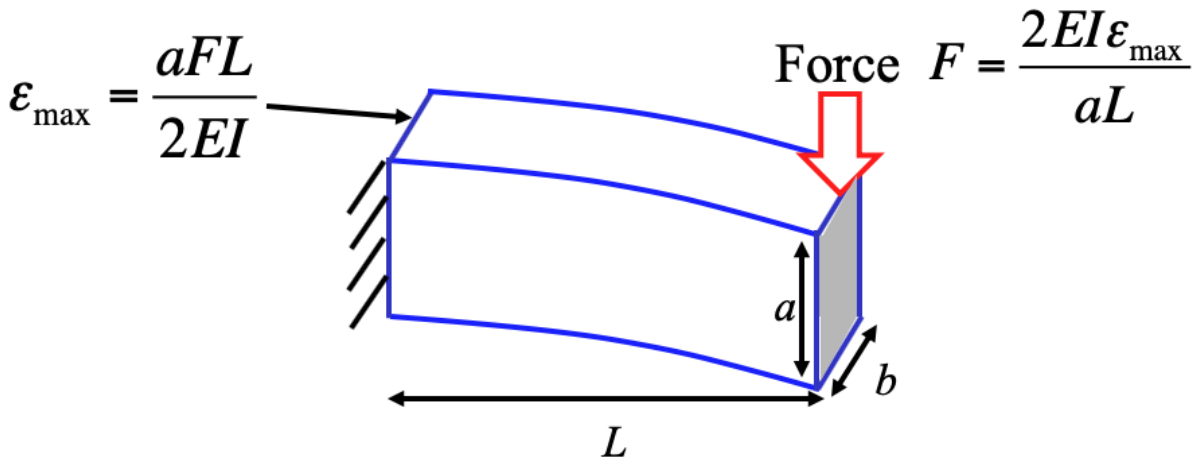

Figure 2.1: Cartoon of a cantilever being displaced by a force F which is equal to the maximum force that can be applied before the strain at the base exceeds the maximum strain limit ϵ_{max}.

to the width b), and $I = \frac{a^3 b}{12}$ is the moment of inertia of the cantilever. This relationship can be rewritten in terms of the maximum force F that can be applied before the cantilever breaks as

$$F = \frac{2EI\epsilon_{max}}{aL}. \tag{2.9}$$

We can then plug in this value for the maximum applied force to calculate the maximum energy that can be stored:

$$U_{max,cantilever} = \frac{1}{2}E \int_{x=0}^{x=L} \int_{z=-a/2}^{z=a/2} \int_{y=-b/2}^{y=b/2} \left(\epsilon_{max}\frac{2z}{aL}(L-x)\right)^2 dy\, dz\, dx. \tag{2.10}$$

The evaluation of this integral results in

$$U_{max,cantilever} = (abL)\frac{1}{18}E{\epsilon_{max}}^2. \tag{2.11}$$

We can compare the previous result to that of the maximum energy density of a uni-axially strained material with volume abL, Young's modulus E, and maximum strain ϵ_{max}, which

has a maximum energy density of

$$U_{max} = (abL)\frac{1}{2}E{\epsilon_{max}}^2. \tag{2.12}$$

The conclusion of this analysis is that a block of material strained as a cantilever stores only $1/9^{\text{th}}$ as much energy as it would if it were strained uni-axially. Despite being less energy dense, cantilevers are useful because they require less force to bend. Finding an optimal spring is discussed further in Section 2.7.

2.4 Getting a 100 Milligram Robot to Vertically Jump 1 Meter

To understand why using the silicon substrate is advantageous for making energy storing springs over the device layer, let us analyze in the absence of air resistance how much energy must be stored for a 100 milligram robot to vertically jump 1m. The jump height h of the robot is equal to

$$h = \frac{U_{stored}}{mg} \tag{2.13}$$

where m is equal to 100 milligrams and g is the standard gravitational acceleration. Solving this equation results in

$$U_{stored} = 1\text{mJ}. \tag{2.14}$$

Let us now calculate how much die area would be needed to store the 1mJ if the device layer was used and if the substrate was used. Consider an SOI wafer with device layer thickness T_{dev} and substrate thickness T_{sub}. We will assume that the max strain of the silicon is 0.5% and therefore the volumetric energy density U_d is equal to $2.1\frac{\text{J}}{\text{cm}^3}$. The areal energy density of the device layer is therefore

$$U_{d,areal,dev} = \frac{1}{9}U_d T_{dev} = 0.939\frac{\text{mJ}}{\text{cm}^2} \tag{2.15}$$

and the areal energy density of the substrate is therefore

$$U_{d,areal,sub} = \frac{1}{9}U_d T_{sub} = 12.9\frac{\text{mJ}}{\text{cm}^2}. \tag{2.16}$$

The SOI fabrication process used has a maximum die area of 2cm × 2cm. If the 40μm device layer was used, a total die area of

$$A_{dev} = \frac{U_{stored}}{U_{d,areal,dev}} = \frac{1\text{mJ}}{0.939\frac{\text{mJ}}{\text{cm}^2}} = 1.06\text{cm}^2 \tag{2.17}$$

would be needed just for the spring, which is more than 25% of the entire die area. Designing actuators, support structures, and other mechanical elements along with such a spring would be an extraordinarily difficult if not an impossible task. However, if the 550μm substrate was used, a total die area of

$$A_{sub} = \frac{U_{stored}}{U_{d,areal,sub}} = \frac{1\text{mJ}}{12.9\frac{\text{mJ}}{\text{cm}^2}} = 0.078\text{cm}^2 \tag{2.18}$$

would be needed, which is more than an order of magnitude smaller. Designing actuators, support structures, and other mechanical elements to work with such a spring is now a much more tractable task.

2.5 The First Fabricated Substrate Spring

A prototype jumping substrate spring was fabricated from an SOI wafer and is shown in Fig. 2.2. No metal deposition was needed to make this prototype spring. The only steps necessary were using DRIE to remove all of the device layer silicon on the top of the spring, and DRIE to etch the substrate. The spring constant of the "box spring" can be analyzed using the dimensions shown in Figs. 2.3 and 2.4.

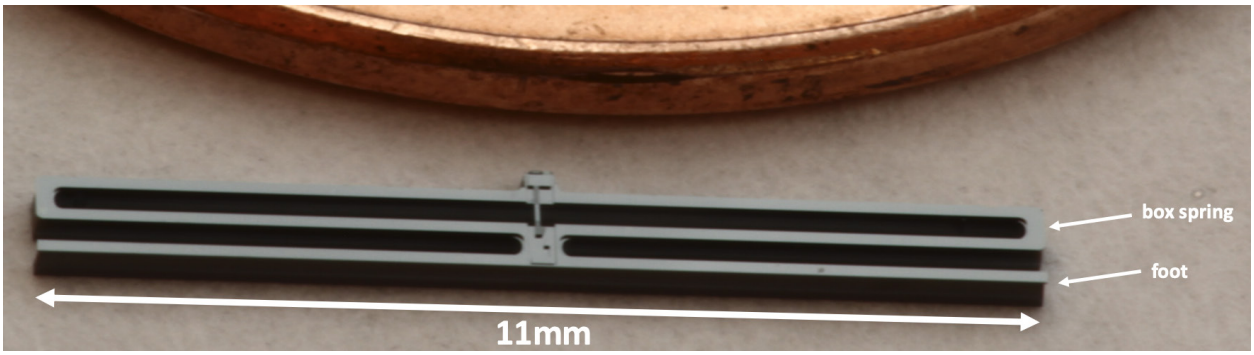

Figure 2.2: A fabricated substrate spring next to a United States penny. The spring is made from 550μm thick single crystal silicon.

The spring constant of the box spring structure can be found by analyzing one quarter of it, as shown in Fig. 2.4, and then using symmetry. Because the complete box spring consists of two parallel structures each consisting of two quarter structures in series, the entire spring constant is equal to that of the quarter structure. We assume that a force F is acting perpendicularly to L_1. Since k_{L_1} is a fixed guided beam, it has a spring constant of

$$k_{L_1} = \frac{12EI}{{L_1}^3}. \tag{2.19}$$

The applied force F generates a moment M_{L_2} on the cantilever with length L_2. Let us now define y as the distance away from the base of the cantilever with length L_2. Using the

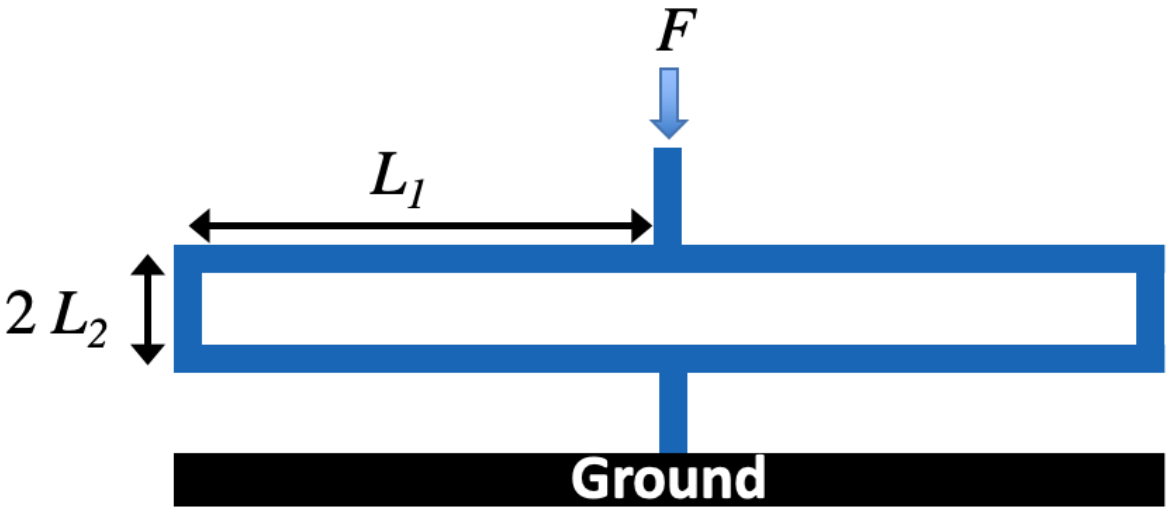

Figure 2.3: Single box spring capable of storing mechanical energy.

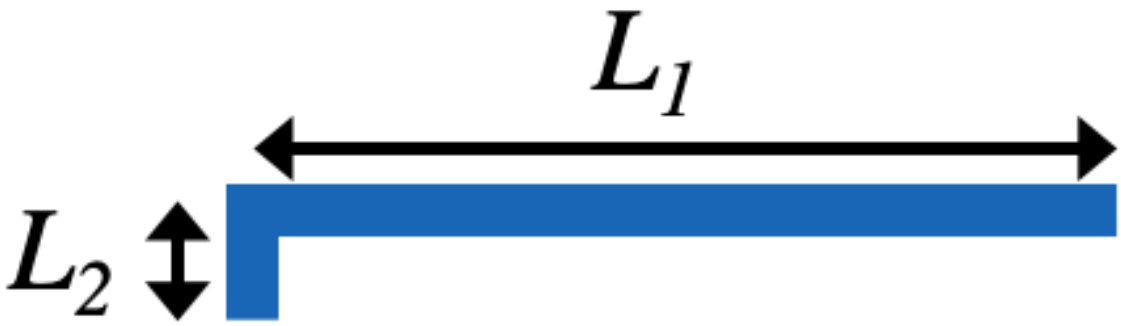

Figure 2.4: Quarter of a box spring for spring constant analysis purposes.

following result from Euler-Bernoulli beam theory, we can calculate the bending angle θ_{L_2} of the cantilever with length L_2 as

$$\theta_{L_2} = \frac{M_{L_2} y}{EI}|_{y=L_2} = \frac{F L_1 L_2}{EI}. \tag{2.20}$$

The total deflection Δy_{total} of the quarter box spring structure is equal to the nominal deflection of k_{L_1} plus the angle θ_{L_2} times the length L_1. The resulting spring constant k_{total} can then be found as

$$\Delta y_{total} = \frac{F}{k_{L_1}} + \theta_{L_2} L_1 = \frac{F}{k_{L_1}} + \frac{F {L_1}^2 L_2}{EI} = F\left(\frac{{L_1}^3}{12EI} + \frac{{L_1}^2 L_2}{EI}\right) = \frac{F}{k_{total}} \tag{2.21}$$

$$\frac{{L_1}^3}{12EI} + \frac{{L_1}^2 L_2}{EI} = \frac{1}{k_{total}} \tag{2.22}$$

$$\frac{12EI}{{L_1}^3 + 12{L_1}^2 L_2} = k_{total}. \tag{2.23}$$

The moment of inertia I of a beam cross-section with width w and thickness T is given by

$$I = \frac{w^3 T}{12} \tag{2.24}$$

where the direction of bending is transverse to the thickness T. However, for a beam with trapezoidal cross sectional area A as shown in Fig. 2.5, the moment of inertia I_{trap} around the y-axis (i.e. in the direction transverse to the thickness T) is given by

$$I_{trap} = \iint_A x^2 \, dx \, dy \tag{2.25}$$

$$= \frac{T(a+b)(a^2+b^2)}{48}. \tag{2.26}$$

It is worth noting that when $a = b = w$ the equation returns to the familiar form of

$$I = \frac{w^3 T}{12}. \tag{2.27}$$

A cross section scanning electron micrograph of a substrate spring can be seen in Fig. 2.6. The cross section is trapezoidal because of a re-entrant profile cause by deep reactive ion etching. Approximating the cross section as a trapezoid with largest and smallest width of 194μm and 172μm, respectively, the moment of inertia can therefore be calculated as

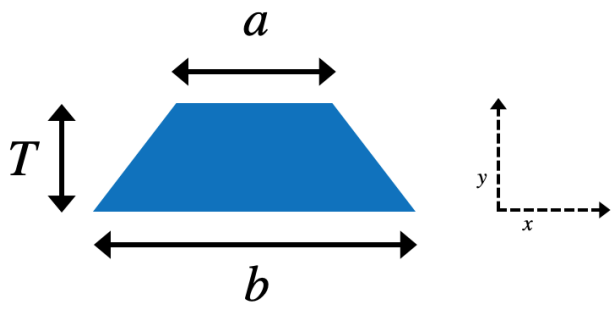

Figure 2.5: A beam with a trapezoidal cross section.

$$I_{trap} = \frac{550\mu\text{m} \times (172\mu\text{m} + 194\mu\text{m}) \times ((172\mu\text{m})^2 + (194\mu\text{m})^2)}{48} = 2.8 \times 10^{-16}\ \text{m}^4. \quad (2.28)$$

The spring constant of the substrate spring shown in Fig. 2.2 can then be calculated as:

$$k = \frac{12 \times 169\text{GPa} \times 2.8 \times 10^{-16}\ \text{m}^4}{(5000\mu\text{m})^3 + (12 \times\ (5000\mu\text{m})^2 \times 100\mu\text{m})} = 3700\frac{\text{N}}{\text{m}}. \quad (2.29)$$

Measured force vs. displacement data of a substrate spring is shown in Fig. 2.7. The data was collected using a Dage 4000 wirebond tester, which functions as a load cell that simultaneously measures applied force and displacement. The measured spring constant was approximately $3600\frac{\text{N}}{\text{m}}$, which is very close to the analytical prediction of $3700\frac{\text{N}}{\text{m}}$. The spring can be compressed at most $\Delta x = 400\mu\text{m}$ resulting in a maximum stored energy of

$$U_{spring,max} = \frac{1}{2}k\Delta x^2 = 290\mu\text{J}. \quad (2.30)$$

2.6 Jumping Model and Jumping Experiment

A simple model for the jumping substrate spring is shown in Fig. 2.8. The model contains two masses and one ideal spring. The masses in the model are the body mass m_b and the foot mass m_f.

The total mass of the substrate spring in Fig. 2.2 is 9 milligrams. The mass labeled "box spring" is 6 milligrams and the mass labeled "foot" is 3 milligrams. For the purpose of the analysis that follows, we will lump half of the box spring mass into m_b, and half into m_f. Therefore, the masses in the model are $m_b = 3$ milligrams and $m_f = 6$ milligrams.

When the substrate spring is compressed and released, all of the spring energy is converted into kinetic energy of the body mass m_b. The velocity v_b of the body mass m_b can be calculated as

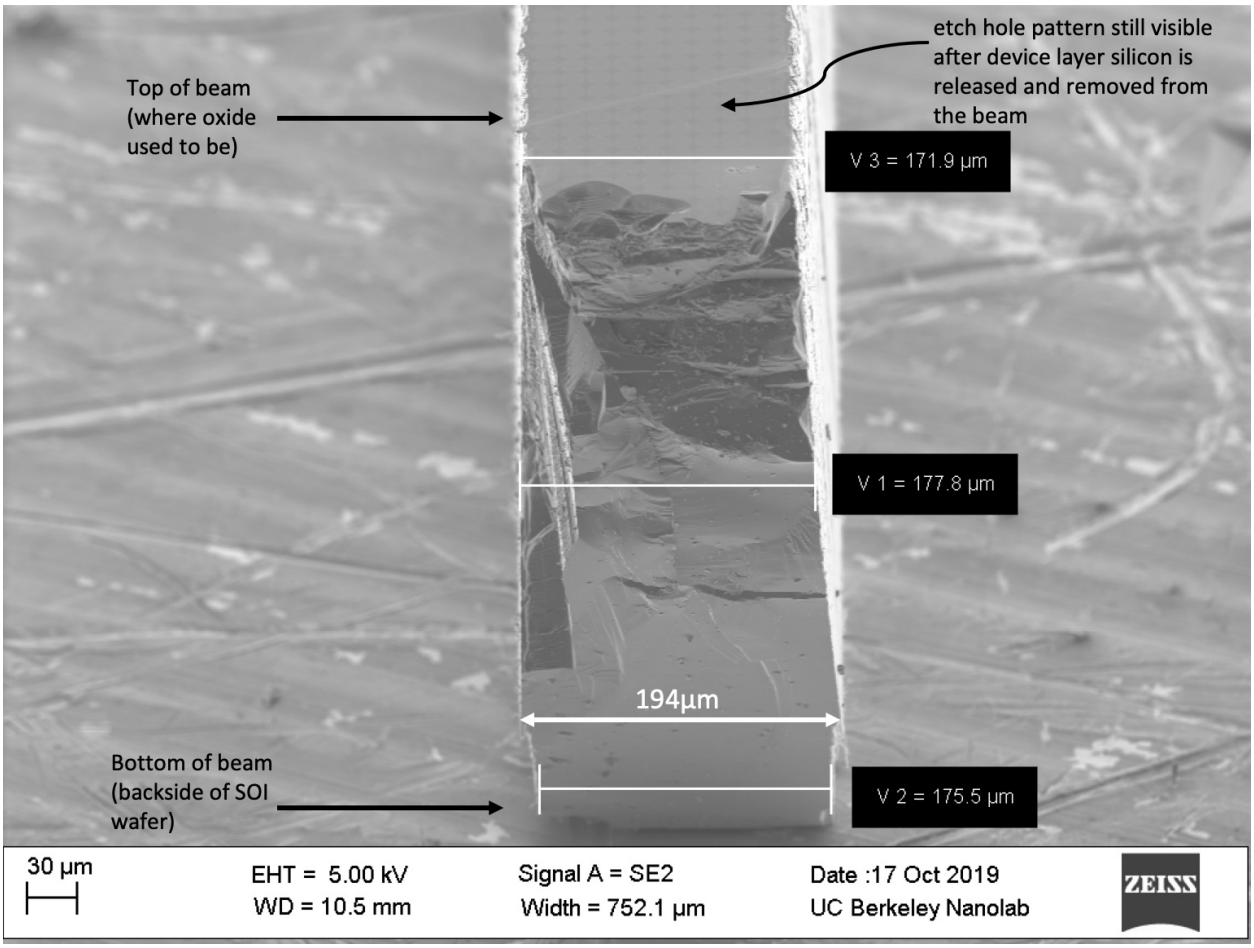

Figure 2.6: Scanning electron micrograph of the substrate spring's cross section.

$$v_b = \left(\frac{2U_{spring}}{m_b}\right)^{\frac{1}{2}} \tag{2.31}$$

$$= 14\frac{\mathrm{m}}{\mathrm{s}}. \tag{2.32}$$

The takeoff velocity v of the entire jumping substrate spring's center of mass can then be calculated as

$$v = \frac{m_b v_b + m_f v_f}{m_b + m_f}. \tag{2.33}$$

Because the foot mass does not move until the instant after take-off, its velocity at takeoff is

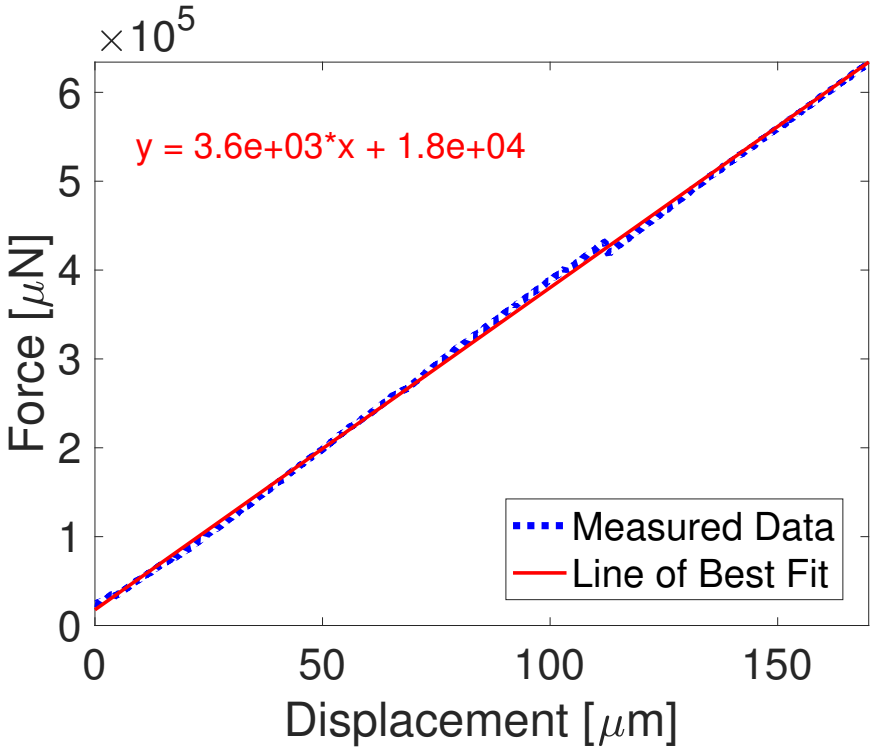

Figure 2.7: Measured force vs. displacement of the jumping substrate spring shown in Fig. 2.2. Also shown are the line of best fit and its equation.

$v_f = 0$. Therefore,

$$v = \frac{m_b v_b + 0}{m_b + m_f} \tag{2.34}$$

$$v = 4.6\frac{\text{m}}{\text{s}}. \tag{2.35}$$

The equations of motion that describe a jumper's horizontal and vertical displacement, respectively, are

$$m\frac{d^2x}{dt^2} = -\frac{1}{2}C_D\rho_{air}A_x\left(\frac{dx}{dt}\right)^2 \tag{2.36}$$

$$m\frac{d^2y}{dt^2} = -\frac{1}{2}C_D\rho_{air}A_y\left(\frac{dy}{dt}\right)^2 - mg \tag{2.37}$$

where C_D is the drag coefficient, A_x is the cross-sectional area in the horizontal direction of jumping, A_y is the cross-sectional area in the vertical direction of jumping, ρ_{air} is the density of air, $m = m_b + m_f$, and g is the standard gravitational acceleration. The maximum jump

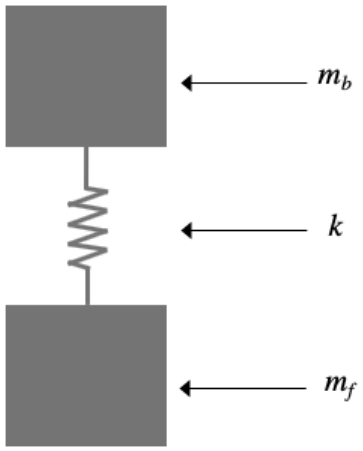

Figure 2.8: A model of the jumping substrate spring consisting of two masses and one ideal spring.

height h and horizontal distance d that are reached can be solved for analytically [44] as

$$h = \frac{m}{C_D A \rho_{air}} \ln\left(1 + \frac{C_D A \rho_{air}}{2mg}\left(v\sin(\theta)\right)^2\right) \tag{2.38}$$

$$d = \frac{2m}{C_D A \rho_{air}} \ln\left[1 + 2v\cos(\theta)\left(\frac{C_D A \rho_{air}}{2mg}\right)^{\frac{1}{2}} \operatorname{atan}\left(v\sin(\theta)\left(\frac{C_D A \rho_{air}}{2mg}\right)^{\frac{1}{2}}\right)\right] \tag{2.39}$$

where v is the takeoff velocity of the jumping substrate spring's center of mass and the takeoff angle θ is with respect to the horizontal.

Assuming the robot tumbles as it travels through the air, we can assume that $A_x = A_y = 1.65 \times 10^{-5}\text{m}^2$ and is equal to the face of the spring with the largest surface area. Using the measured spring constant of $k = 3600\frac{\text{N}}{\text{m}}$, a conservative drag coefficient of $C_D = 1.6$ [45], $\rho_{air} = 1.225\frac{\text{kg}}{\text{m}^3}$, and $\theta = 90$ degrees, the maximum jump height h is equal to 44cm.

Figs. 2.9 and 2.10 shows a fabricated substrate spring jumping after being manually compressed with tweezers. The jump was captured at 30 frames per second, and each red circle shows the location of the spring at each frame. A spring displacement of 155μm and a takeoff angle of $\theta = 80$ degrees corresponds to 43μJ of stored energy, a center of mass takeoff velocity of $1.8\frac{\text{m}}{\text{s}}$, and an approximate jump height and jump distance of 12cm and 9cm, respectively, as shown in Fig. 2.10.

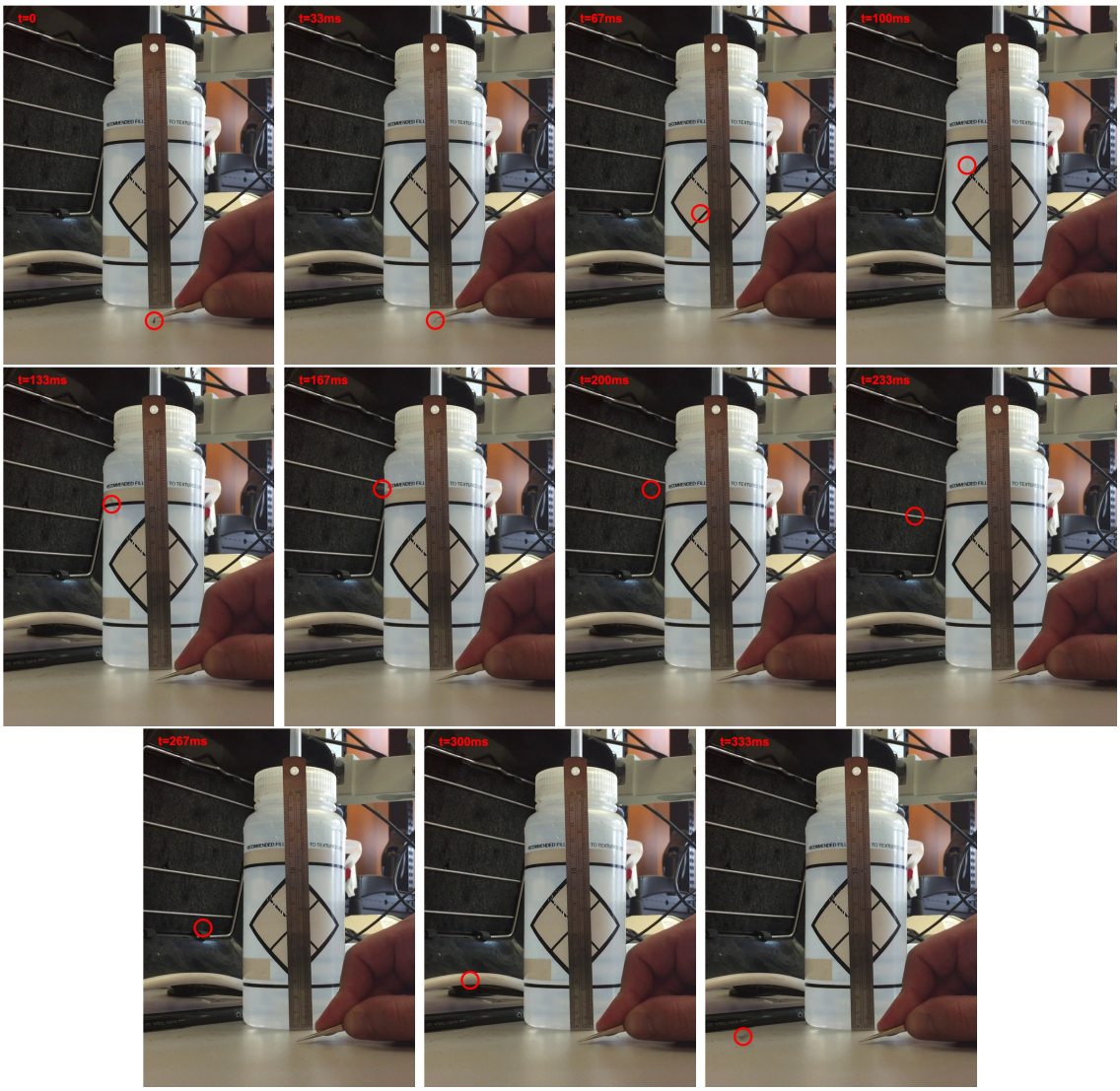

Figure 2.9: Individual frames of the substrate spring jumping. Energy was stored by compressing the spring with tweezers. Each red circle is the location of the spring.

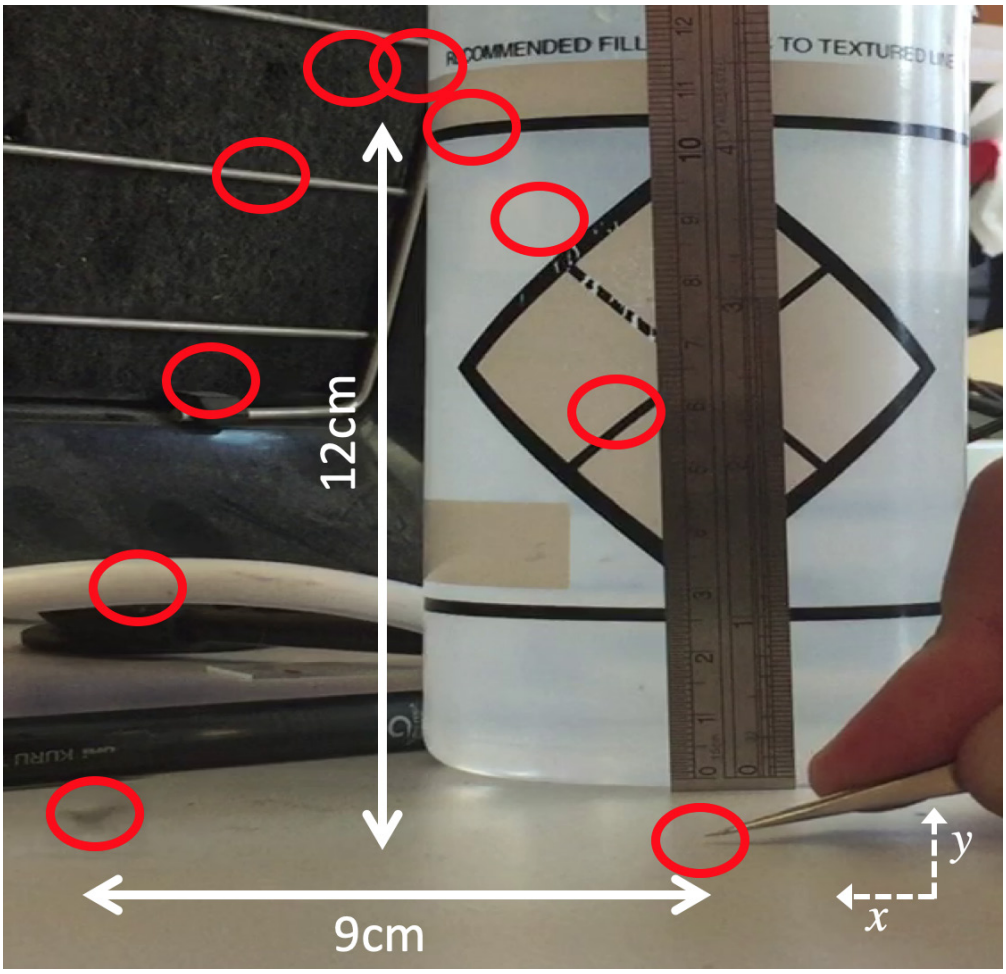

Figure 2.10: All frame measurements from Fig. 2.9 superimposed onto the final frame.

2.7 Spring Scaling and Optimization for a Force Limited Actuator

A spring with stiffness k stretched a distance Δx by an actuator producing force F will store an energy U_{spring} equal to

$$U_{spring} = \frac{1}{2}k\Delta x^2 \tag{2.40}$$

$$= \frac{1}{2}\frac{F}{\Delta x}\Delta x^2 \tag{2.41}$$

$$= \frac{1}{2}F\Delta x. \tag{2.42}$$

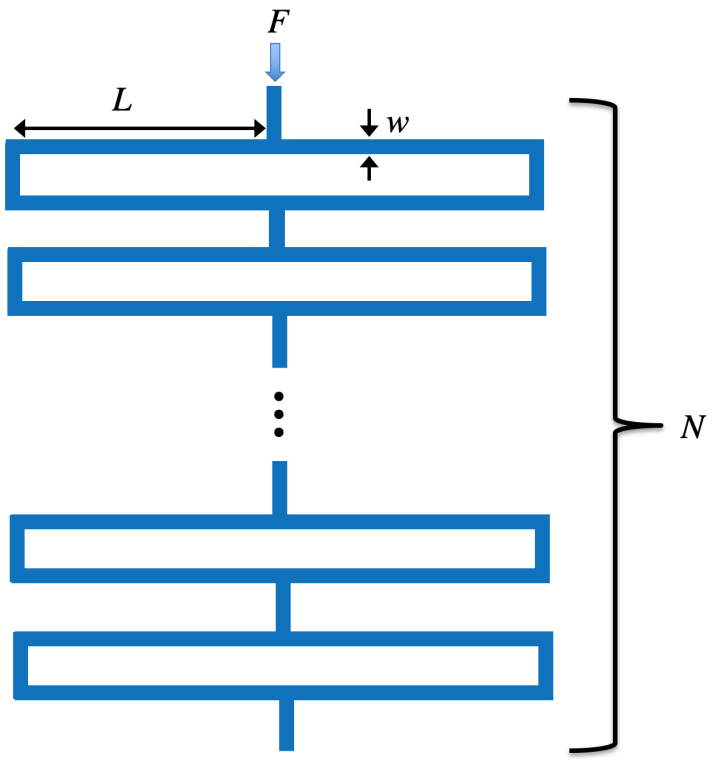

Figure 2.11: N box springs in series. The entire spring constant k is a function of the width w, length L, thickness T, and number of box springs in series N.

From this equation it can be seen that to store a desired amount of energy U_{stored}, there is a trade off between the applied force F and the displacement Δx. Specifically, if one increases, the other can decrease, and vice versa. In practice, the actuator is the limiting factor, i.e. it can produce at most a maximum force F_{max}. In this case, the stored energy will be equal to

$$U_{spring} = \frac{1}{2}k\Delta x^2 \tag{2.43}$$

$$= \frac{1}{2}k\left(\frac{F_{max}}{k}\right)^2 \tag{2.44}$$

$$= \frac{{F_{max}}^2}{2k} \tag{2.45}$$

and it is therefore optimal to design a weak spring with a long displacement. However, the spring will break if stretched too far, so the spring must also be designed with its strain limit ϵ_{max} in mind. Additionally, there will be a practical limit on the displacement with a limit of Δx_{max} and a maximum spring length of L_{max}.

Assuming the spring is displaced by a force F_{max}, consists of N box springs in series, has substrate thickness T, width w, length L, and Young's modulus E, then the stiffness k and maximum strain in the spring ϵ are given as

$$k = \frac{Ew^3T}{NL^3} \tag{2.46}$$

$$\epsilon = \frac{3LF_{max}}{2ETw^2}. \tag{2.47}$$

This optimization problem can thus be formulated as finding the parameters w, L, and N that produce the spring constant k_{best} from the set of all possible spring constants $\mathcal{K}$ where

$$k_{best} = \arg\max_{k \in \mathcal{K}} \frac{{F_{max}}^2}{2k} \tag{2.48}$$

$$\text{s.t.} \quad \epsilon \leq \epsilon_{max} \ , \ \frac{F_{max}}{k} \leq \Delta x_{max} \ , \ L \leq L_{max}. \tag{2.49}$$

The next section uses this optimization formulation to search over the (w,L,N) parameter space to find a substrate spring design that can store enough energy for a 100mg robot to jump 1 meter.

2.8 Actuator Force and Spring Constant Needed to Jump 1 Meter

Let us now make some assumptions about the design of a jumping microrobot in order to quantify the requirements on the actuators that will be used to store energy in substrate springs. Let us first assume a robot design with a total mass of 100 milligrams, with a body mass of 70 milligrams and a foot mass of 30 milligrams. The 70 milligram body includes the mass of a CMOS solar cell chip [34] for power and a CMOS brain [35] for computation and communication.

If we assume the robot has a thickness of 592μm (the total wafer thickness used in the fabrication process), a total layout area of 1cm^2, and jumps in the direction transverse to its thickness, it will aerodynamically behave as a thin plate. If 1.6mJ of spring energy is stored, Equations 2.31 and 2.33 can be used to calculate the center-of-mass takeoff velocity as $5\frac{\text{m}}{\text{s}}$. This results in a Reynolds number of

$$R_e = \frac{\rho v L}{\mu} \tag{2.50}$$

$$= \frac{1.225\frac{\text{kg}}{\text{m}^3} \times 5\frac{\text{m}}{\text{s}} \times 1\text{cm}}{18.5\mu\text{Pa} \cdot \text{s}} \tag{2.51}$$

$$= 3300 \tag{2.52}$$

where ρ is the density of air, v is the center-of-mass takeoff velocity, L is the characteristic length (1cm), and μ is the viscosity of air. A thin plate with a Reynolds number of 3300 has a drag coefficient of 0.1 [46]. Equation 2.38 can then be used to show this results in a jump height of 1m.

As a design choice let us also assume the height of the body is approximately 7mm. If we assume the robot is fabricated with a supportive frame around its perimeter to serve as a foot, then the spring can displace up to 13mm (because the maximum die area is 2cm $\times$ 2cm). This is illustrated in Fig. 2.12. Using Equations 2.40 and 2.42 to determine the force and spring constant required to store the necessary 1.6mJ results in **250mN** and $\mathbf{19}\frac{\mathbf{N}}{\mathbf{m}}$, respectively. Assuming a 550μm thick substrate and Young's modulus of 169GPa, a search over the (w, L, N) parameter space subject to the constraints of the optimization problem presented in the previous section results in a substrate spring with $N = 4$, $L = 9.1$mm, and $w = 85\mu$m. This spring design will store 1.6mJ when displaced 13mm.

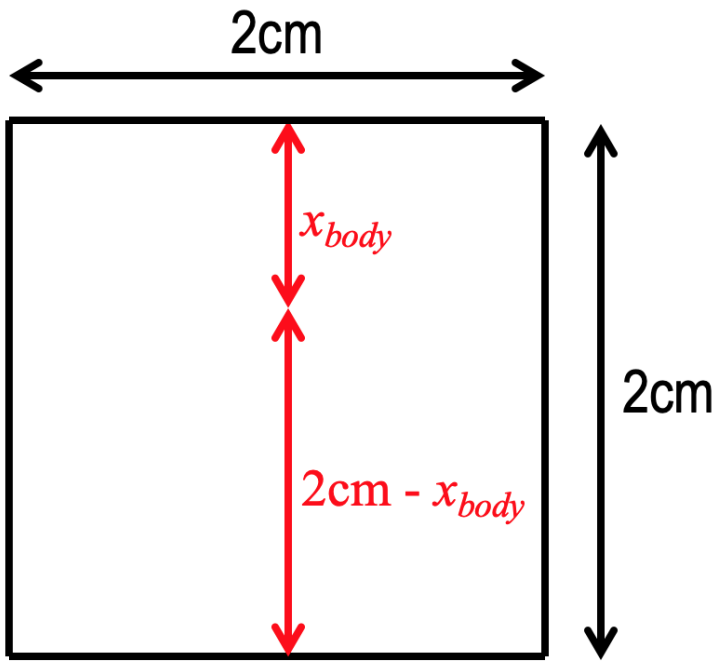

Figure 2.12: A layout view of the 2cm$\times$2cm die area available in the SOI process. If the height of the robot body is x_{body}, then the substrate spring can be displaced at most by 2cm $- x_{body}$.

Chapter 3

High Force Density Electrostatic Inchworm Motors

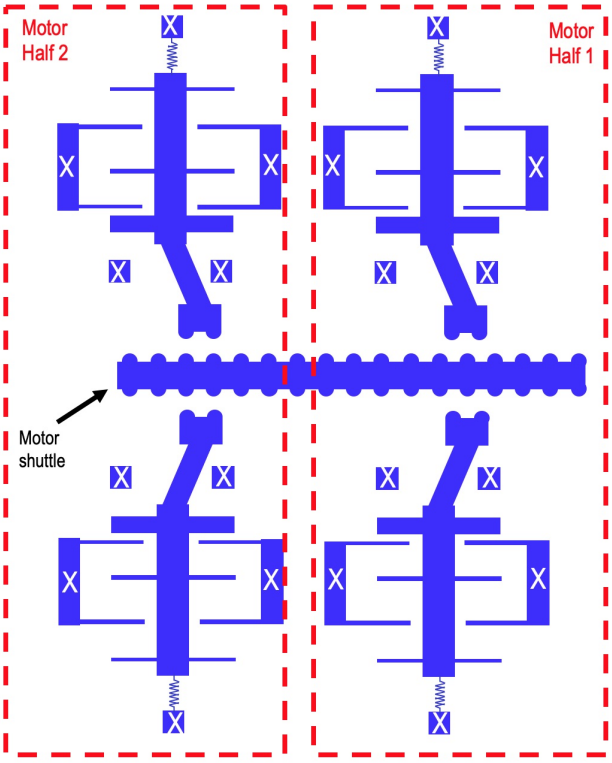

Figure 3.1: Schematic of an angled arm electrostatic inchworm motor [47]. The motor consists of two halves. The simplest design consists of two gap closing actuators per half, as shown here.

In order to store energy in a substrate spring on a jumping microrobot, an actuator is required. The rest of this chapter proceeds as follows: the operating principle of inchworm

motors is introduced, then characterization of new motors with increased actuator density is presented, and finally steps to further improve the new motors to achieve the 250mN needed for 1m jumping are shown.

3.1 Basic Inchworm Motor Operating Principle

Electrostatic inchworm motors [47, 48, 49, 50] are a type of linear micromotor that can provide millinewtons of force over millimeters of displacement. Additionally, they are very useful for microrobotic applications [21, 22, 50] because they require no static power draw and can be fabricated from a single mask using deep reactive ion etching. The operating principle

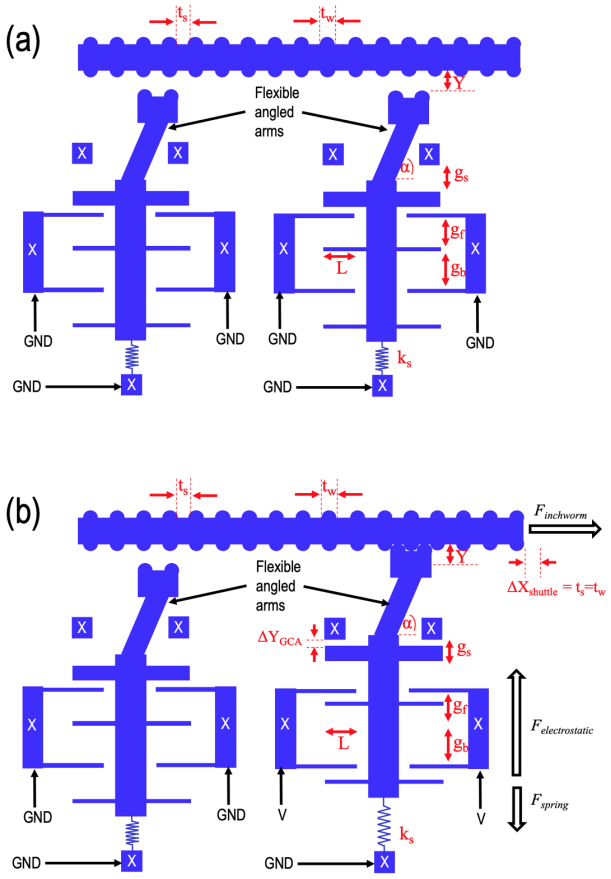

Figure 3.2: Critical dimensions of the motor are shown. Each motor half has two gap closing actuators that are always actuated simultaneously. Therefore, for illustrative purposes, only one gap closing actuator from each motor half is shown. (a) – None of the gap closing actuators have been energized. (b) – The right gap closing actuator in contact with the central shuttle. The resulting force of interest is $F_{inchworm}$, which is a function of $F_{electrostatic}$ and F_{spring}.

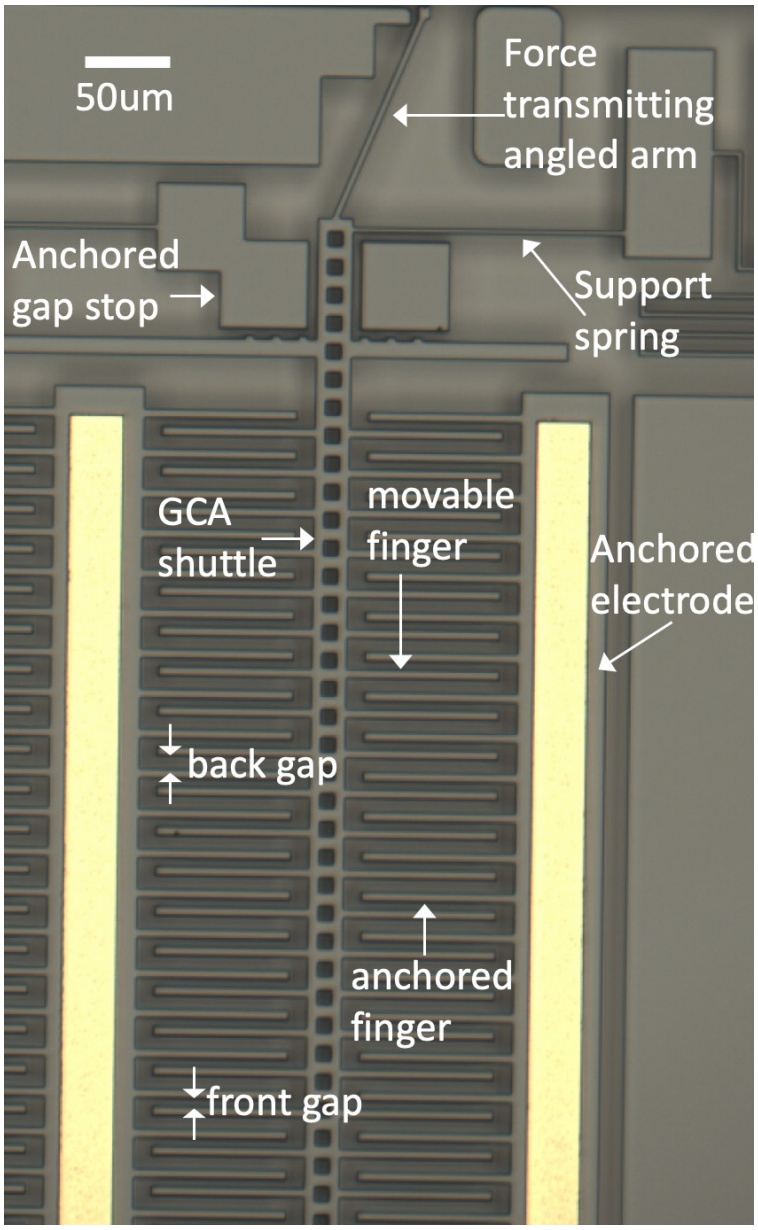

Figure 3.3: Distances and structures of interest on a fabricated gap closing actuator.

of the motors is based on the electrostatic force generated between two conductive parallel plates with surface area A, separation distance g, voltage V, charge Q, and permittivity ϵ, given by

$$F_{electrostatic} = \frac{1}{2}\epsilon V^2 \frac{A}{g^2} = \frac{1}{2}\frac{Q^2}{\epsilon A}. \tag{3.1}$$

The electrostatic inchworm motors in this work are based off the angled arm design and optimization scheme first developed by Penksiy [47] and later worked on by Contreras [50] and Greenspun [40].

A cartoon of a simple angled arm electrostatic inchworm motor is shown in Fig. 3.1. In general, an electrostatic inchworm motor consists of two motor halves, and each half contains N_a sets of parallel plate arrays (the parallel plates are also called "fingers"). Each parallel plate array is called a gap closing actuator. The motor shown in Fig. 3.1 has $N_a = 2$ gap closing actuators per motor half. Each gap closing actuator has N_f sets of parallel plates. Figs. 3.2 and 3.3 show the critical dimensions of the motor in both cartoon form and a fabricated device. The motor functions as a linear stepper motor and is designed to take individually controllable steps in increments of $\Delta X_{shuttle}$. The distance $\Delta X_{shuttle}$ is designed to be the minimum feature size of the fabrication process, which is 2μm for the work in this dissertation. The four step sequence that the motor repeatedly goes through in order to move the central shuttle is shown in Fig. 3.4.

3.2 Output Force Analysis

The output force $F_{inchworm}$ of the motor is equal to the horizontal force transmitted to the central shuttle at the moment the gap closing actuators contact it (Fig. 3.2) and is given by

$$F_{inchworm} = \frac{1}{\tan(\alpha)} \left(F_{electrostatic} - F_{spring}\right) \tag{3.2}$$

$$= \frac{1}{\tan(\alpha)} \left(\frac{1}{2}\epsilon V^2 T L N_a N_f \left(\frac{1}{(g_f - Y)^2} - \frac{1}{(g_b + Y)^2}\right) - Y k_s\right) \tag{3.3}$$

where α is the angle of the angled arm, ϵ is the permittivity, V is the actuator voltage, T is the thickness of the device layer, L is the overlap length of the fingers, N_a is the number of gap closing actuators per motor half, N_f is the number of fingers per gap closing actuator, g_f is the starting front gap of the fingers in the gap closing actuators, g_b is the starting back gap of the fingers in the gap closing actuators, Y is the distance that the gap closing actuators must travel before contacting the central shuttle, and k_s is the stiffness of the support spring structure which serves as an anchor for each gap closing actuator's shuttle. The support spring consists of two fixed-guided beams of length L_k and width w_k. The pre-factor of $\frac{1}{\tan(\alpha)}$ is from the mechanical disadvantage of the angled arm as it transmits force to the central shuttle [47].

3.3 Increased Actuator Density

Previous implementations of inchworm motors by Penskiy [47] and Contreras [21, 22] had a one-to-one mapping between the number of gap closing actuators in the cartoon of Fig 3.1 and the number of realized gap closing actuators in layout, as shown in Fig. 3.5; the left

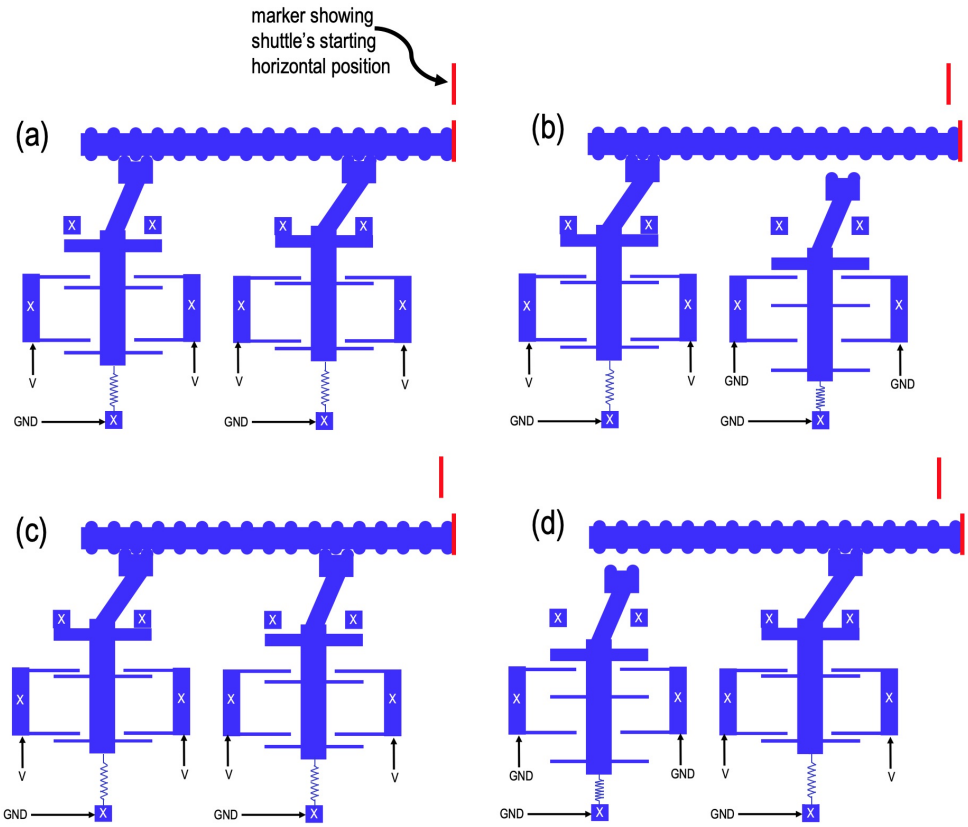

Figure 3.4: The motor moves the central shuttle forward by repeatedly iterating through the following steps. (a) – Both actuators are in contact with the central shuttle. (b) – The voltage V is removed from the right motor half and the angled arms of the left motor half flex and push the central shuttle forward by a distance $\Delta X_{shuttle} = 2\mu$m. (c) – The right motor half is actuated with voltage V. (d) – The voltage V is removed from the left motor half and the angled arms of the right motor half flex and push the central shuttle forward by a distance $\Delta x_{shuttle} = 2\mu$m. The voltage V is then applied to the left motor half and the process restarts at (a).

shows the motor cartoon and the right shows the actual layout used to fabricate the motor. The gap closing actuators in the black circles are actuated at the same time, and the motors in the red circles are actuated a the same time. Greenspun [14] increased the numbers of gap closing actuators in his motors to a two-to-one mapping, however there was still wasted layout area between adjacent actuators.

In order to create even more powerful motors to be used for storing energy in substrate springs, motors with an eight-to-one mapping, also shown in Fig. 3.5, were designed, fabricated, and tested [16, 51]. These motors were generated using tools in the MEMS Microrobot

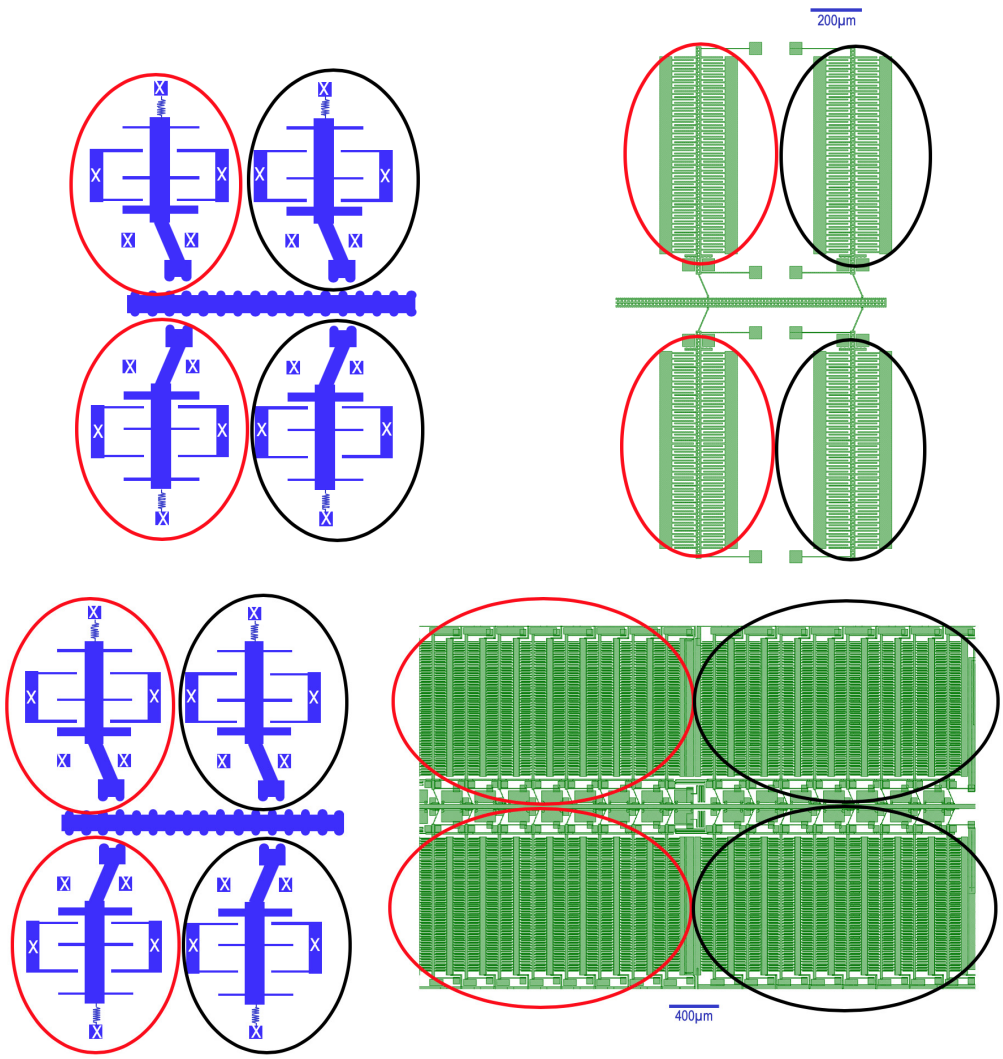

Figure 3.5: Top – A motor with a one to one mapping between the gap closing actuators in the cartoon schematic and layout. This configuration was used by Penskiy [47] and Contreras [21, 22, 50]. Bottom – A motor with an eight to one mapping between the gap closing actuators in the cartoon schematic and layout. This motor was designed for jumping microrobots with the goal of increasing actuator and force density [16, 51].

Library[1]. For each of the four gap closing actuators in the cartoon on the bottom left of Fig. 3.5, there are eight gap closing actuators in the actual design in layout, as is shown in the bottom right of Fig. 3.5. In order to have a shared ground signal as well as to sum the output force from each set of eight gap closing actuators, their trusses were combined, as shown in Fig. 3.6. Additionally, the density of the actuators was increased. The gap

[1]The MEMS Microrobot Library was created by J. Greenspun [40]. The code repository can be found at `https://github.com/pinxisimitu/MEMS_Microrobot_Library`.

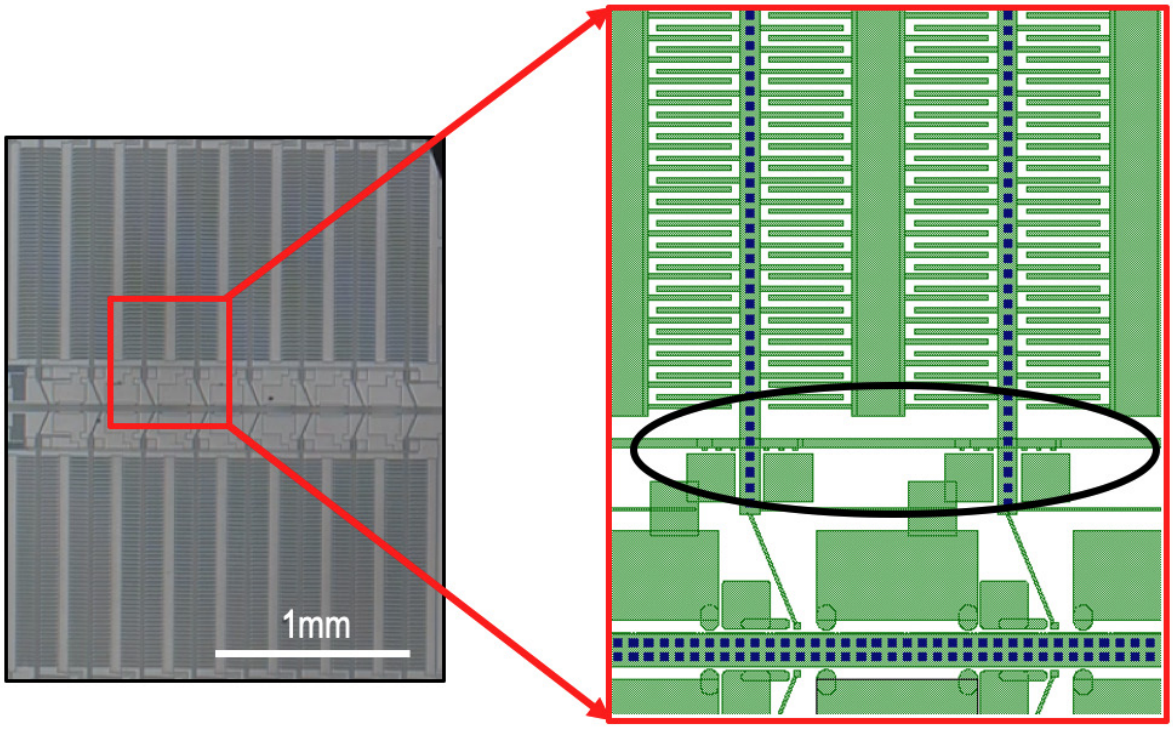

Figure 3.6: The trusses from multiple gap closing actuators have been combined to sum their output forces (black oval). Also, neighboring actuators share their anchored electrodes.

closing actuators were butted up against each other so that each each actuator shared its two anchored electrodes with its two adjacent neighbor actuators.

For a given minimum feature size (2μm for the work in this dissertation and the work of Greenspun [14, 40]), a useful metric for characterising the density of an electrostatic inchworm motor is the ratio of the total force producing capacitive finger overlap area $A_{cap,fingers}$ and the total layout area of the motor A_{layout}. For the motor with an eight-to-one mapping [16, 51], this ratio is equal to 0.69, whereas the previous two-to-one mapping motor [14] was 0.38. If only the layout area of the fingers is used in the ratio calculation, the value for the eight-to-one mapping motor is 1.4, which is the theoretical limit of the ratio if all structures except for the fingers were eliminated from the design.

Jump height decreases with increased mass, so maximizing the force density of a jumping microrobot is very important. The effects of mass on jumping can be seen in Equations 2.33 and 2.38.

Fig. 3.7 shows multiple images of the motor layout with increasing levels of resolution. Small guide bumps were used to prevent the motor shuttle from rotating in-plane while minimizing the contact surface area required to do so. Without these bumps, the teeth on

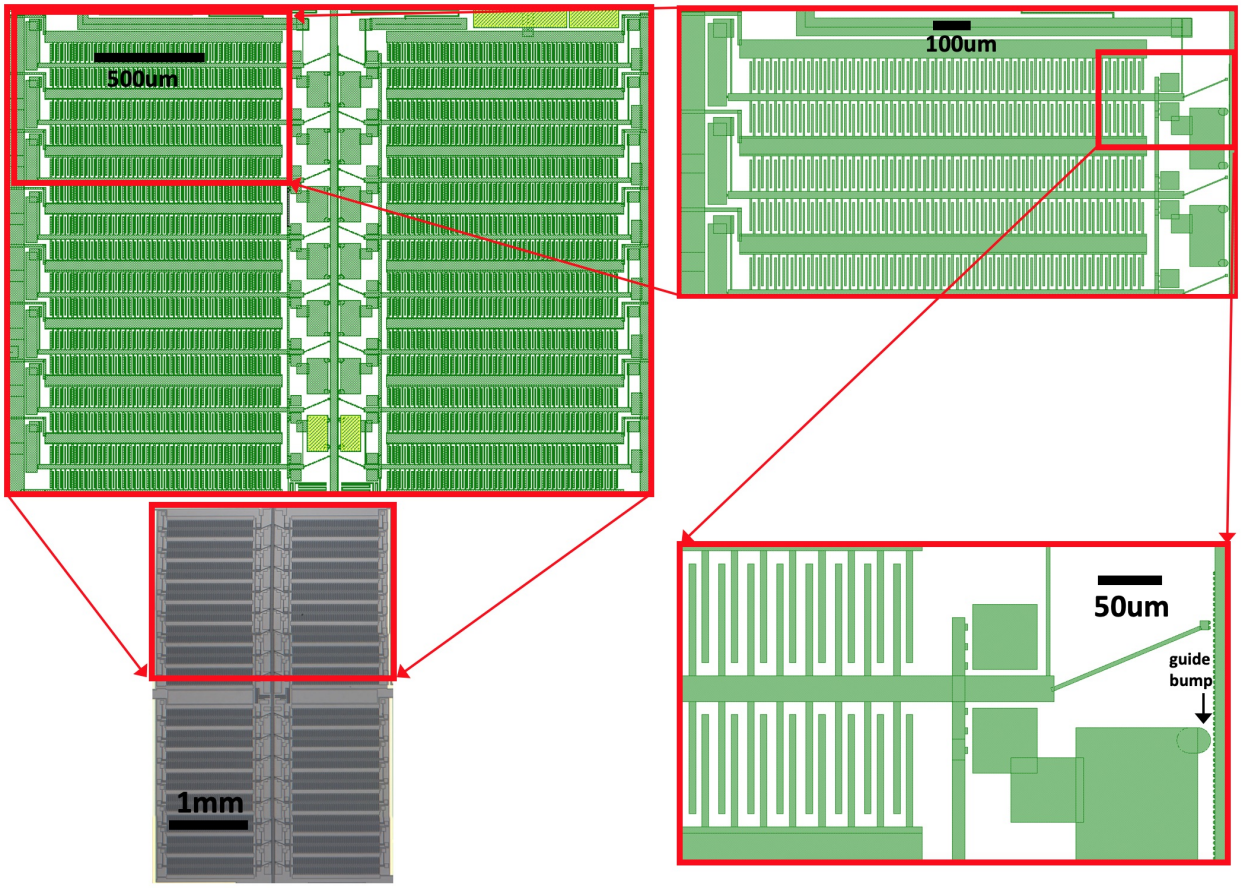

Figure 3.7: A motor with 32 gap closing actuators with multiple insets that increase in zoom. The motor can produce 15mN at 100V. Note the guide bump which keeps the motor shuttle vertically aligned and prevents it from hitting nearby silicon structures.

the central shuttle would both rub against nearby silicon as well as get caught on the corners of nearby silicon, in both cases getting damaged and jamming the motor.

A top down image of the fabricated motor taken from a probe station microscope camera is shown in Fig. 3.8. There are 32 gap closing actuators on the motor each with 96 moving fingers for a total of over 3000 moving fingers on the motor. This motor displacing its central shuttle by 2mm is shown in Fig. 3.9. The dimensions and parameter values of the motor as drawn in layout are given in Table 3.1.

3.4 Measured Force Output

The output force $F_{inchworm}$ as a function of applied voltage was measured experimentally. Motors were designed and fabricated with stiff restoring springs attached the motor's central shuttle. The stiffness of the springs was also measured using a Dage 4000 wire bond tester. A

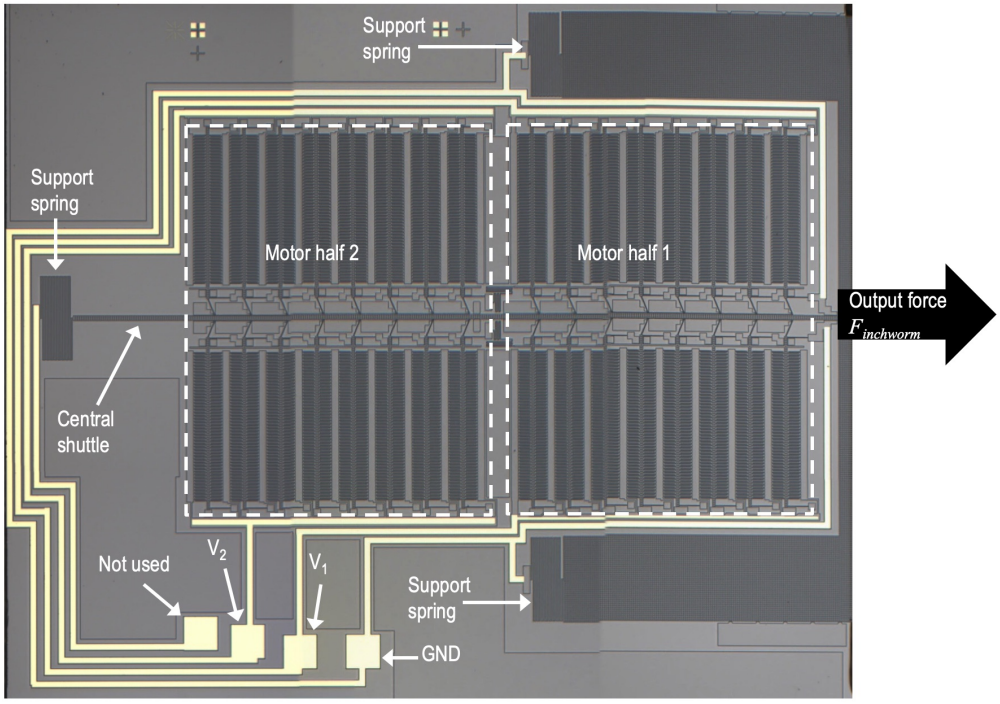

Figure 3.8: A motor with 32 gap closing actuators capable of producing 15mN of force at 100V. The entire micrograph is approximately 6mm×5mm.

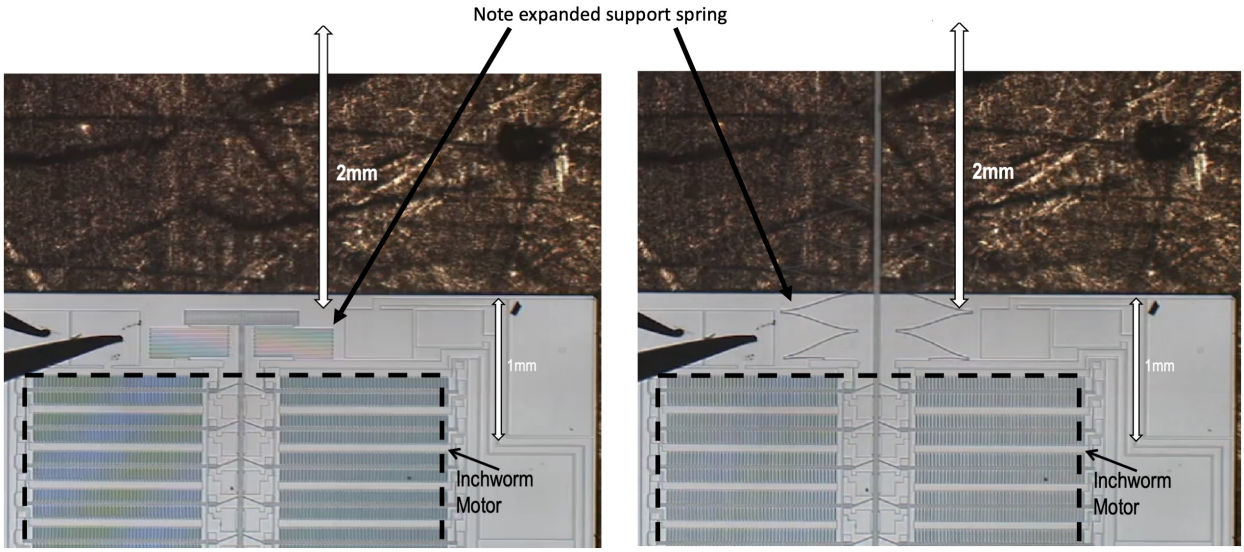

Figure 3.9: A motor with 32 gap closing actuators deflecting its shuttle by more than 2mm before it's support spring finally fractures and breaks.

Parameter	As Drawn in Layout
Actuators Per Motor Half N_a	16
Moving Fingers Per Actuator N_f	96
Tooth Width t_w	2.5μm
Tooth Separation t_s	1.5μm
Pawl to Shuttle Distance Y	3μm
Angled Arm Angle α	67 degrees
Gap Stop Distance g_s	3.833μm
Initial Front Gap Distance g_f	4.833μm
Initial Back Gap Distance g_b	7.75μm
Finger Overlap Length L	76.4μm
Support Spring Width w_k	3μm
Support Spring Length L_k	152.8μm
Angled Arm Length L_{arm}	129μm
Distance to Gap Stop After Pawls Contact Shuttle ΔY_{GCA}	0.833μm
Shuttle Step Distance $\Delta X_{shuttle}$	2μm

Table 3.1: The dimensions of the motor in Fig. 3.8 as drawn in layout.

DRIE undercut of 0.48μm was calculated by comparing measured spring stiffness to theory. The test motors were actuated with different voltages and commanded to take steps until they began to stall. Using the measured stiffness of the restoring springs and the maximum displacement of the central shuttle, the output force $F_{inchworm}$ was calculated, and is shown in Fig. 3.10. Also shown in the figure is a fit to the data using Equation 3.3, which is the equation for $F_{inchworm}$ given previously; the parameter Y, which is the distance the gap closing actuator must travel before contacting the central shuttle, was varied until the sum of the squared errors between the data and the model was minimized. The distance Y was drawn in layout as 3μm, but was estimated by the least squares minimization to be 3.4μm, corresponding to an undercut of 0.2μm in the 3μm wide drawn pawl-to-shuttle trench. Because smaller feature sizes tend to have smaller DRIE undercuts, the parameter Y was chosen to be varied because it is the smallest etch distance in the electrostatic force equation.

These motors have other potential uses in addition to stretching substrate springs for microrobots. Fig. 3.11 shows a micro gripper [51] containing one of the 32 cap closing actuator motors capable of producing 15mN at 100V, a jaw made of the 550μm silicon substrate with maximum displacement of 1mm, a capacitive sensor for force feedback, a contact sensor for determining when an object has been grabbed, and a z-axis stop to prevent the motor's central shuttle from popping out of plane. The gripper holding a 0.2 gram through-hole resistor is shown in Fig. 3.12. The gripper was able to release the 0.2 gram though-hole resistor after grabbing it. Applications for such a gripper range from an arm attachment for sub-gram robot platforms to a general tool for manual or automated microassembly of robots

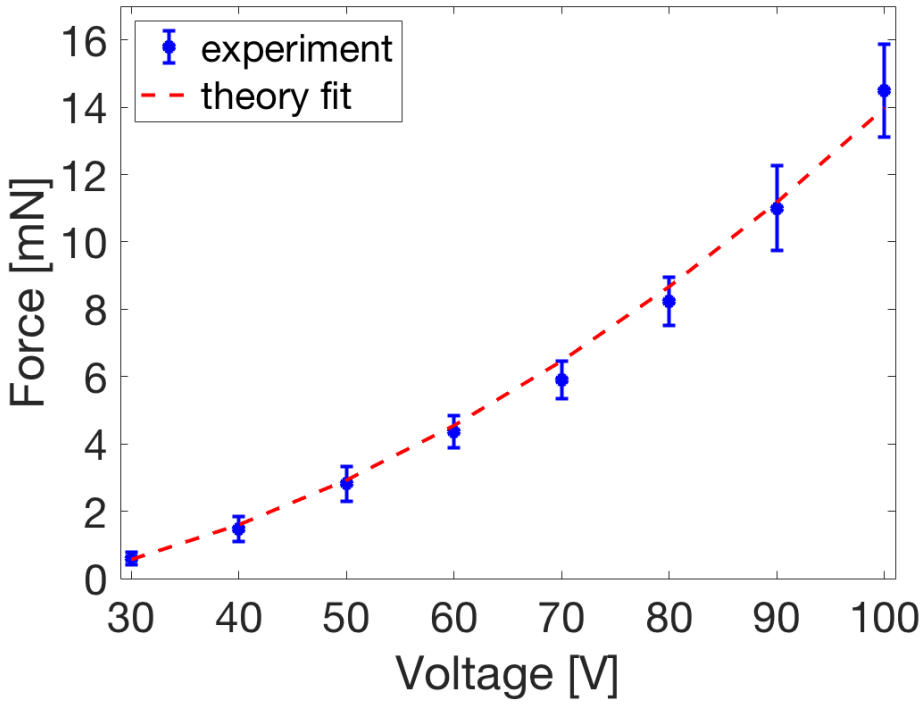

Figure 3.10: Measured force $F_{inchworm}$ vs applied voltage of the 32 gap closing actuator motor in Fig. 3.8.

or other small systems.

3.5 Input Power & Limits to Efficiency

The power required to run an electrostatic motor is given by

$$P = CV^2 f \tag{3.4}$$

where P is the input electrical power, C is the total capacitance of the motor (finger capacitance as well as parasitic capacitance), V is the applied voltage, and f is the actuator drive frequency [48].

The 15mN motors presented in this chapter contain a total of 32 gap closing actuators each with 96 moving fingers, for a total of more than 3000 moving fingers on the motor. Each time a motor half grabs and releases the motor shuttle, the motor shuttle travels 2μm. Therefore, all 32 of the gap closing actuators are charged to the applied voltage V each time 4μm of travel is accumulated. A frequency of 1Hz moves the central shuttle at a rate of 4μm per second.

Estimates for the total motor capacitance were made using the areas drawn in layout. A schematic of the variable front gap and back gap capacitances of a GCA unit cell can be seen in

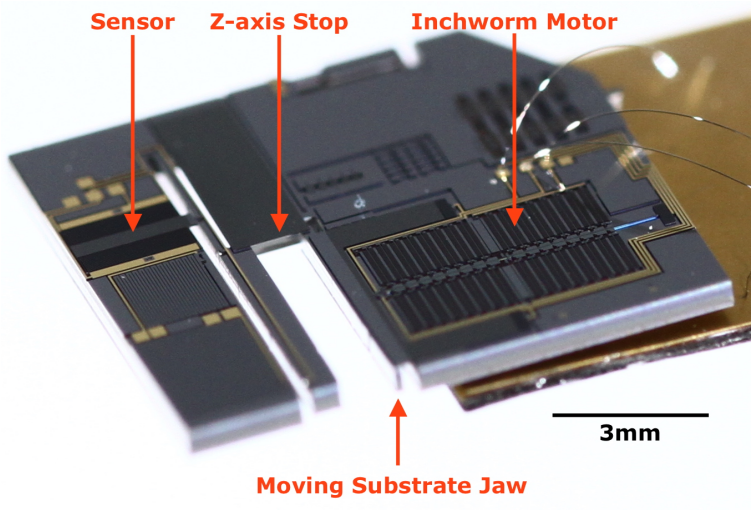

Figure 3.11: A microgripper [51] with a 32 gap closing actuator motor. There are more than 3000 moving capacitive fingers on the gripper.

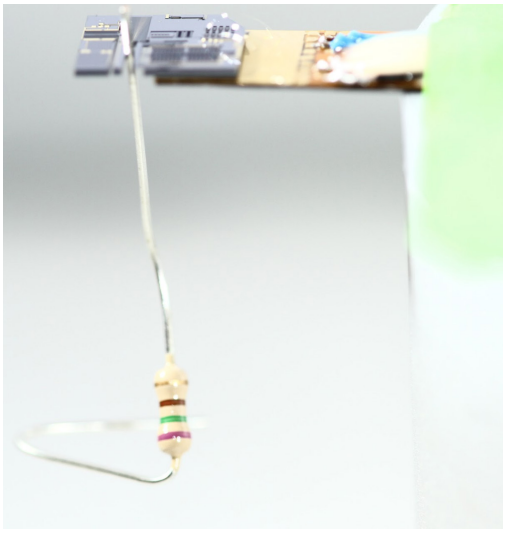

Figure 3.12: A microgipper with a 32 gap closing actuator motor holding a 0.2 gram through-hole resistor.

Fig. 3.13. The total front gap and back gap capacitance from the fingers on all 32 gap closing actuators is $C_{fingers}(x = 0) = 24$pF (i.e. when all gaps are open) and $C_{fingers}(x = g_s) = 88$pF (i.e. when all gaps are closed). In addition to this 88pF there is additional static parasitic capacitance: there is 27pF of parasitic capacitance $C_{anchored\_electrodes\_to\_substrate}$ from all of the finger anchors to the substrate, another 22pF of parasitic capacitance $C_{routes\_to\_substrate}$ from the high voltage signal routes to the substrate (i.e. the routes from the bond pads to all 32 GCAs), and 2pF of parasitic capacitance $C_{bondpads\_to\_substrate}$ from the two high voltage

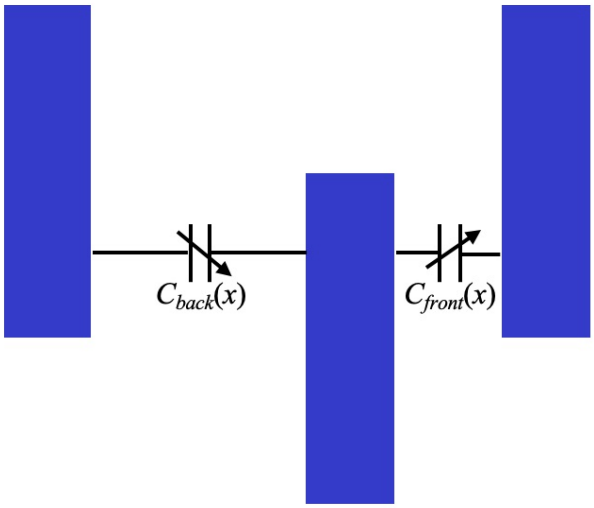

Figure 3.13: A schematic of the variable front gap and back gap capacitances of a GCA unit cell. The center finger is movable and the left and right fingers are anchored. The displacement x is with respect to the relaxed position of the movable finger (i.e. no forces acting on the movable finger). The front gap capacitance C_{front} and back gap capacitance C_{back} are a function of position x. The total finger capacitance $C_{fingers}(x) = 2N_aN_f\left(C_{front}(x) + C_{back}(x)\right)$.

bondpads to the substrate. Therefore, the total estimated capacitance that is charged and discharged every time the shuttle moves a distance of 4μm is:

$$C = C_{fingers}(x = g_s) + C_{parasitic} \tag{3.5}$$

$$= 88\text{pF} + (27\text{pF} + 22\text{pF} + 2\text{pF}) = 139\text{pF}. \tag{3.6}$$

At 100V of applied voltage, 139pF of total capacitance, and an actuator frequency of 250Hz ($1\text{Hz} = 4\frac{\mu\text{m}}{s} \rightarrow 250\text{Hz} = 1\frac{\text{mm}}{s}$), the estimated input power to the motor if the capacitance is discharged to ground without charge recycling is approximately 0.3mW. The maximum efficiency η (i.e. the ratio of mechanical work out to electrical energy in) of the motor without charge recycling is

$$\eta = \frac{F_{max}\Delta x}{CV^2} \tag{3.7}$$

$$= \frac{15\text{mN} \times 4\mu m}{139pF \times (100V)^2} = 4\%. \tag{3.8}$$

If all of the parasitic capacitance could be removed, then the efficiency would be 7%.

If the DRIE undercut is improved so that it is uniformly 0.48μm among all features and trench widths, then the model predicts $F_{inchworm}$ should be 25mN at 100V. Additionally, if charge on the capacitors was recycled between itself and a storage capacitor using an ideal DC-to-DC converter each cycle, and the energy in the restoring springs is recovered each cycle, then the efficiency would be approximately 20%.

Furthermore, if adiabatic charging [52, 53] with a DC-to-DC converter was used instead of a constant voltage source then the efficiency would be approximately 70%. The DC-to-DC converter would initially put just enough charge on the fingers so that the electrostatic force was equal to the restoring spring force at the instant the angled arms would contact the shuttle. This would allow the actuators to overcome the restoring spring force as they moved toward the shuttle. At the instant the angled arms contacted the shuttle, the DC-to-DC converter would put just enough additional charge on the fingers to bring their voltage up to 100V; no additional charge would be put on the actuators throughout the rest of the stroke, resulting in a constant load force of approximately 25mN, as predicted by the model. The energy stored in the capacitors when the gaps fully closed would be recovered by the DC-to-DC converter.

The maximum efficiency of an electrostatic motor [52] is limited only by the efficiency of DC-to-DC conversion, parasitic capacitance, efficiency of the mechanisms used in the design, and fabrication constraints.

3.6 Increasing Motor Force by Insulating the Fingers

The motors presented in this chapter with an eight-to-one mapping can be further improved to significantly increase the force density. Currently, the moving fingers have a 1μm final front gap when they are pulled-in to prevent them from shorting to the electrified anchored fingers. This 1μm final gap could be eliminated by depositing a thin layer of alumina on the fingers, which would serve as an insulating layer and prevent the grounded and electrified fingers from shorting when they touch [40].

If the need to have a 1μm final gap was eliminated, then the quantity $g_f - Y$, which is equal to the front gap of the fingers at the instant the angled arm contacts the central shuttle, could be 1μm smaller than it currently is. Currently, the angled arms are designed to contact the motor shuttle when the front gap is 1.8μm. If instead the angled arms were designed to contact the motor shuttle with a front gap of 0.8μm, then the electrostatic force would increase by a factor of approximately

$$\frac{(1\ /\ 0.8\mu\text{m})^2}{(1\ /\ 1.8\mu\text{m})^2} = 5. \tag{3.9}$$

Additionally, the applied voltage to the actuators could be increased because catastrophic finger pull-in and shorting would no longer be a problem [54]. Increasing the applied voltage from 100V to 200V would increase the electrostatic force by another factor of 4. In summary, a total force increase of approximately 20 should be possible by coating the motor fingers in an insulating alumina layer and decreasing the initial front gap distance g_f by 1μm, resulting in an actuator that can produce the 250mN needed to jump 1m.

3.7 Increasing Gap Closing Actuator Force and Speed Using Thinner Device Layers

Let us now analyze the dynamics and scaling effects of a single gap closing actuator subject to electrostatic force $F_{electrostatic}$, spring force F_{spring}, and damping force $F_{damping}$ consisting of squeeze film damping $b_{squeeze}$ [55] and Couette flow damping $b_{couette}$ [43]. The differential equation describing the position x of the actuator from its relaxed (i.e. no forces) position is given by

$$F_{electrostatic} - F_{spring} - F_{damping} = m\ddot{x} \tag{3.10}$$

where

$$F_{electrostatic} = \frac{1}{2}\epsilon V^2 LT\left(\frac{1}{(g_f - x)^2} - \frac{1}{(g_b + x)^2}\right) \tag{3.11}$$

$$F_{spring} = \frac{2E{w_k}^3 T}{{L_k}^3}x = kx \tag{3.12}$$

$$F_{damping} = \mu LT^3\beta\left(\frac{1}{(g_f - x)^3} + \frac{1}{(g_b + x)^3}\right)\dot{x} + \frac{\mu A_b}{d}\dot{x} = b_{squeeze}\dot{x} + b_{couette}\dot{x} = b\dot{x} \tag{3.13}$$

with capacitive overlap length of the fingers L, applied voltage V, permittivity ϵ, Young's modulus E, support spring width w_k, support spring length L_k, device layer thickness T, viscosity of air μ, initial front gap g_f, initial back gap g_b, device layer to oxide separation distance d, correction factor β [55], total actuator shuttle and movable finger layout area A_b, and total actuator shuttle and movable finger mass m.

The minimum feature size λ that can be achieved with DRIE is related to the maximum achievable aspect ratio of the DRIE etch, R, by $\lambda = T/R$, where T is the device layer thickness. Scaling benefits can be seen by looking at what happens to the electrostatic force $F_{electrostatic}$ as T and R change, assuming the smallest the gap can be is the minimum feature size of the process λ. For the analysis that follows, we will ignore the effects on the system dynamics due to the back gap g_b under the assumption that the system dynamics are dominated by the effects from the front gap g_f. Analyzing the electrostatic force we find

$$F_{electrostatic} = \frac{1}{2}\epsilon_0 V^2\frac{LT}{\lambda^2} = \frac{1}{2}\epsilon_0 V^2\frac{LR^2}{T} \propto \frac{R^2}{T}. \tag{3.14}$$

Therefore, decreasing the device layer thickness allows stronger motors to be designed. Likewise, the benefits to actuator speed can be seen by looking at what happens to squeeze film damping (the dominating damping term).

$$b_{squeeze} = \mu_{air} LT^3\beta\frac{1}{\lambda^3} = \mu_{air} L\beta R^3 \propto R^3 \tag{3.15}$$

If the squeeze film damping term is what dominates the maximum achievable speed, the velocity of the actuator can be approximated as

$$\dot{x} \approx \frac{F_{es}}{b_{squeeze}} \propto \frac{1}{RT}. \tag{3.16}$$

The actuator has to travel the gap λ in order to close, and therefore the time Δt it takes to do so is

$$\Delta t \approx \frac{\lambda}{\dot{x}} \propto T^2. \tag{3.17}$$

Therefore, decreasing thickness increases the actuator pull-in speed.

3.8 Simulated Motor Performance as a Function of Device Layer Thickness

The model and thickness optimization scheme presented in [50] was used to simulate performance of GCAs designed for use in angled arm electrostatic inchworm motors. The initial conditions for pull-in were $x = 0$ and $\dot{x} = 0$, and the initial conditions for pull-out were $x = g_f - x_f$ and $\dot{x} = v_{init}$, where x_f is the final front gap distance, g_f is the initial front gap distance, and v_{init} is an initial shuttle velocity during pull-out due to strain energy stored in the fingers and shuttle. To explore the effects of scaling a GCA similar to those on the previously presented high force motors (i.e. adjacent GCAs can share their anchored fingers' electrodes), the following values were used in the Matlab model: number of fingers $N = 96$, pawl to shuttle distance $Y = 2\lambda$, final front gap $x_f = 0.5\lambda$, angled arm angle $\alpha = 67$ degrees, initial front gap $g_f = \lambda/\tan(\alpha) + Y + x_f$, initial back gap $g_b = 1.5g_f$, device layer to oxide separation distance $d = T/10$, finger width $w_f = 2\lambda$, finger overlap length $L = 40\lambda$, support spring width $w_k = \lambda$, and support spring length $L_k = 75\lambda$. The shuttle width was made equal to the minimum value that ensures it neither buckles nor fractures under the maximum electrostatic force exerted on it after pull-in occurs. The width of the angled arm was made equal to 4λ and the length of the angled arm was designed with safety factor of 10 to prevent buckling. The width of the stationary fingers' anchors was made equal to 25λ. For thin device layers, the electrostatic force after pull-in is strong enough to bend the fingers a distance greater than x_f. Therefore, the maximum deflection of each finger was limited to x_f when computing the initial velocity v_{init} of the shuttle during pull-out. Simulated results (using Matlab's ode45 solver) for applied voltages of 100V and 200V using $R = 20$ and $R = 40$ are shown in Fig. 3.14. Performance was plotted as a function of device layer thickness. The maximum GCA frequency f_{max} is defined as

$$f_{max} = \frac{1}{t_{pullin} + t_{pullout}}. \tag{3.18}$$

The area used to calculate force density is a bounding box around the actuator, including periphery such as the stationary finger electrodes, support springs, and angled arm.

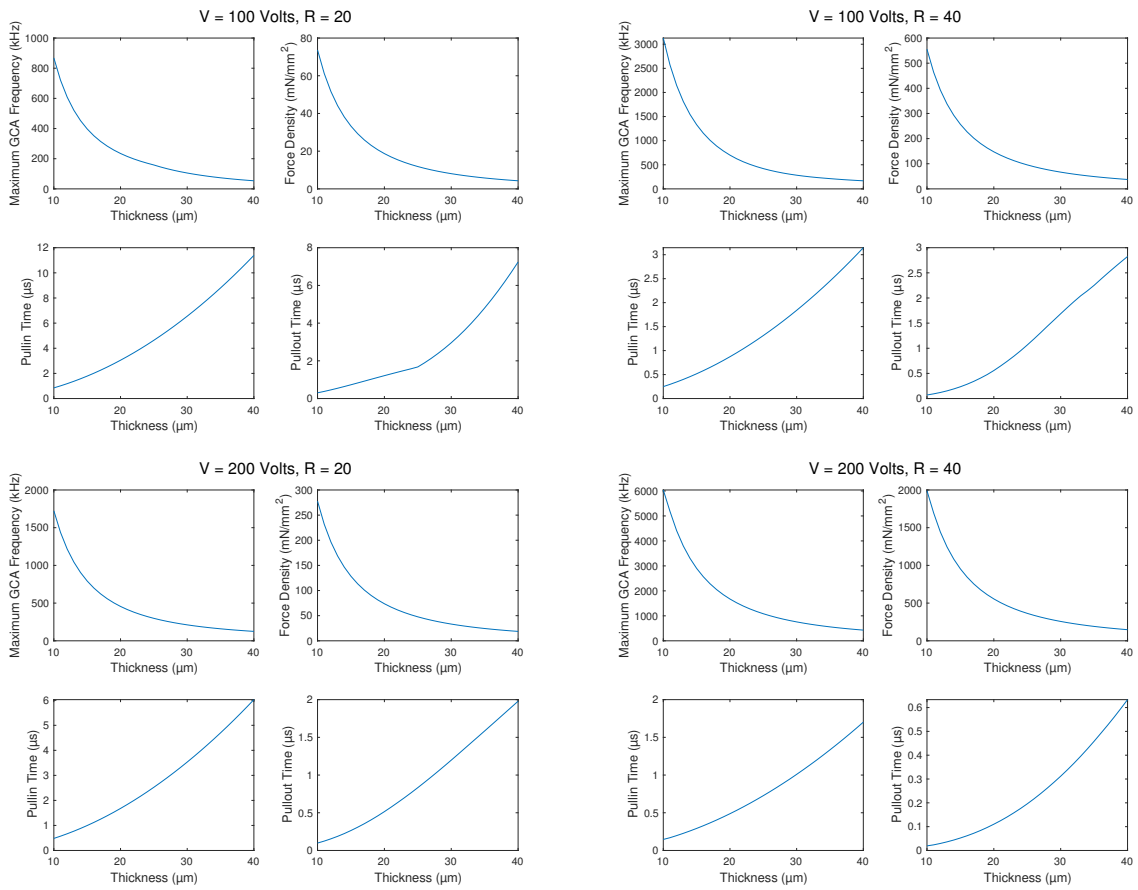

Figure 3.14: Simulations of gap closing actuator performance as a function of device layer thickness, applied voltage, and aspect ratio.

3.9 Speed and Mechanical Power Output of Loaded Gap Closing Actuators

Test structures were designed with a 40μm device layer and 2μm minimum feaure size (i.e. $R = 20$) so that speed and mechanical power output of loaded GCAs could be measured directly. Each test structure consists of a spring which when pre-loaded with a probe tip provides a near constant load force against the GCA shuttle throughout the entirety of pull-in. Let us define the distance that the shuttle travels during pull-in as Δx_{shut}. If the desired constant load force is F_{load}, then the spring is designed to have a stiffness k so that it exerts a force $F_{spring} = 100k\Delta x_{shut} = F_{load}$ when stretched a distance of $100\Delta x_{shut}$. The relative

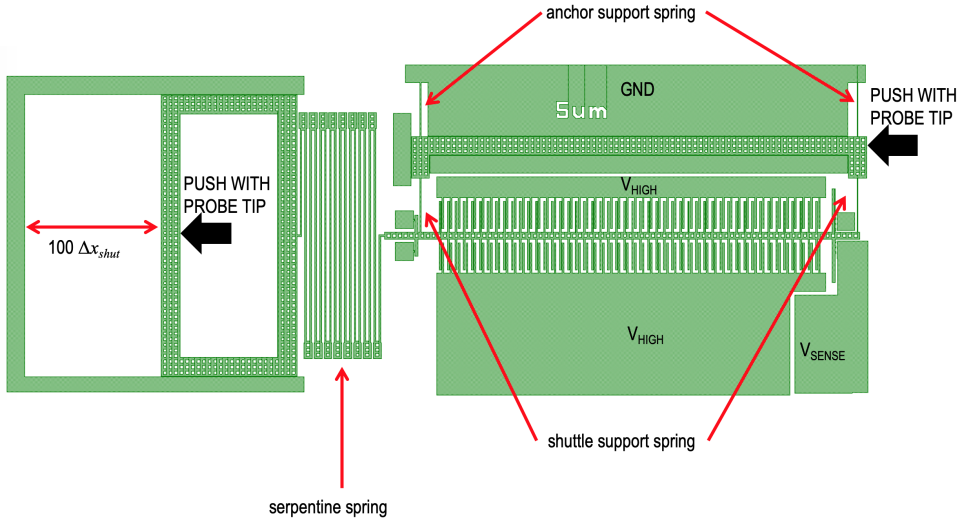

Figure 3.15: Layout of a test structure used to measure pull-in time and mechanical power output of a GCA.

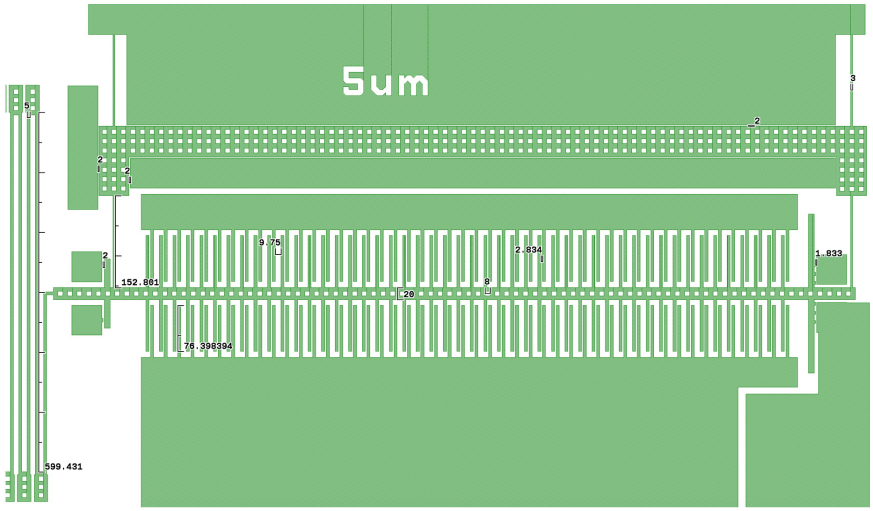

Figure 3.16: Layout and drawn dimensions of a test structure designed to load the GCA with 50μN of force.

change throughout pull-in is then

$$\frac{\Delta F_{spring}}{F_{load}} = \frac{101k\Delta x_{shut} - 100k\Delta x_{shut}}{100k\Delta x_{shut}} \tag{3.19}$$

$$= \frac{k\Delta x_{shut}}{100k\Delta x_{shut}} = 1\%. \tag{3.20}$$

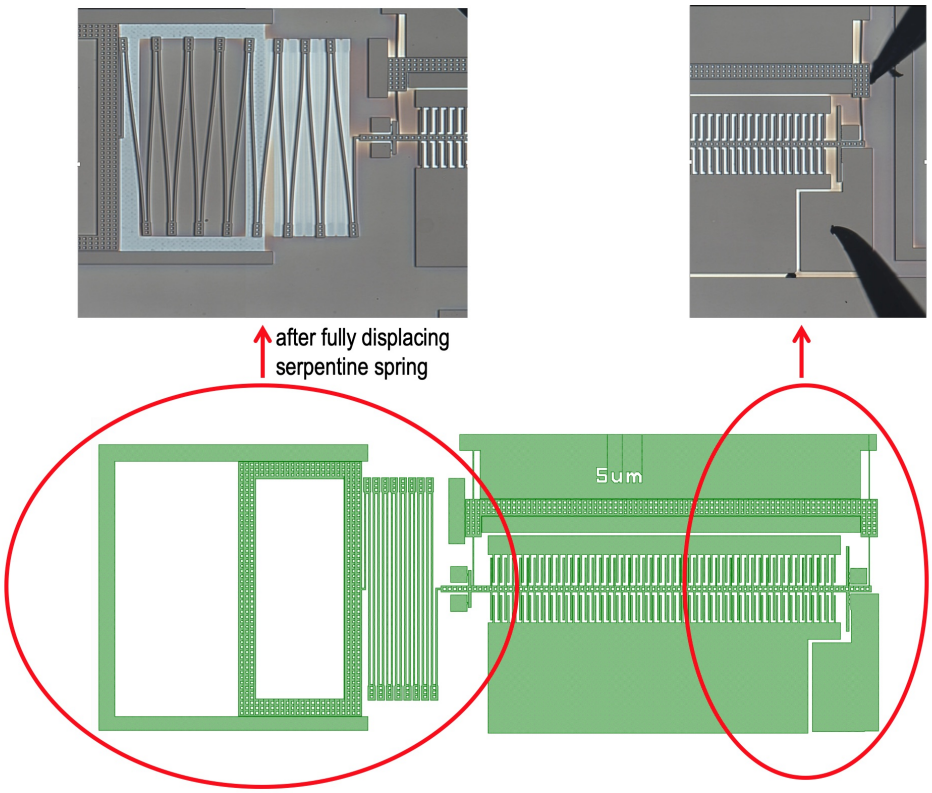

Figure 3.17: Images of a real test structure after the serpentine spring has been fully displaced a distance of $100\Delta x_{shut}$.

Fig. 3.15 shows an example test structure. Six probe tips are needed for actuation and testing: one to pull back the serptine spring a distance of $100\Delta x_{shut}$, two to provide the V_{HIGH} signal, one to provide ground, one to push back the shuttle's movable anchor, and one for sensing pull-in on the V_{SENSE} pad.

Fig. 3.16 shows layout and dimensions of a test structure designed to provide a 50μN load force. Another test structure designed to provide 100μN of load force has exactly the same dimensions, except the drawn beam width of the serpentine spring is 6.04μm instead of 5μm. A no load structure (i.e. with no serpentine spring) was also fabricated and has exactly the same dimensions as the GCAs used in the high force density motor in the previous sections.

The structures were sputtered with approximately 50nm of TiN to lower the sidewall resistance of the structures. When the grounded shuttle contacts the V_{SENSE} pad which is pulled up to 5V with a resistor, the signal gets pulled to ground. Fig. 3.17 shows images from a real 50μm load force test structure. Note the unsputtered areas which were shadowed by the serpentine spring and the movable box structure attached to the serpentine spring. One third of the serpentine spring mass (i.e. the spring's effective mass) is added to GCA mass m for the loaded simulations.

Fig. 3.18 shows experimentally measured pull-in times and power-to-mass ratios for no

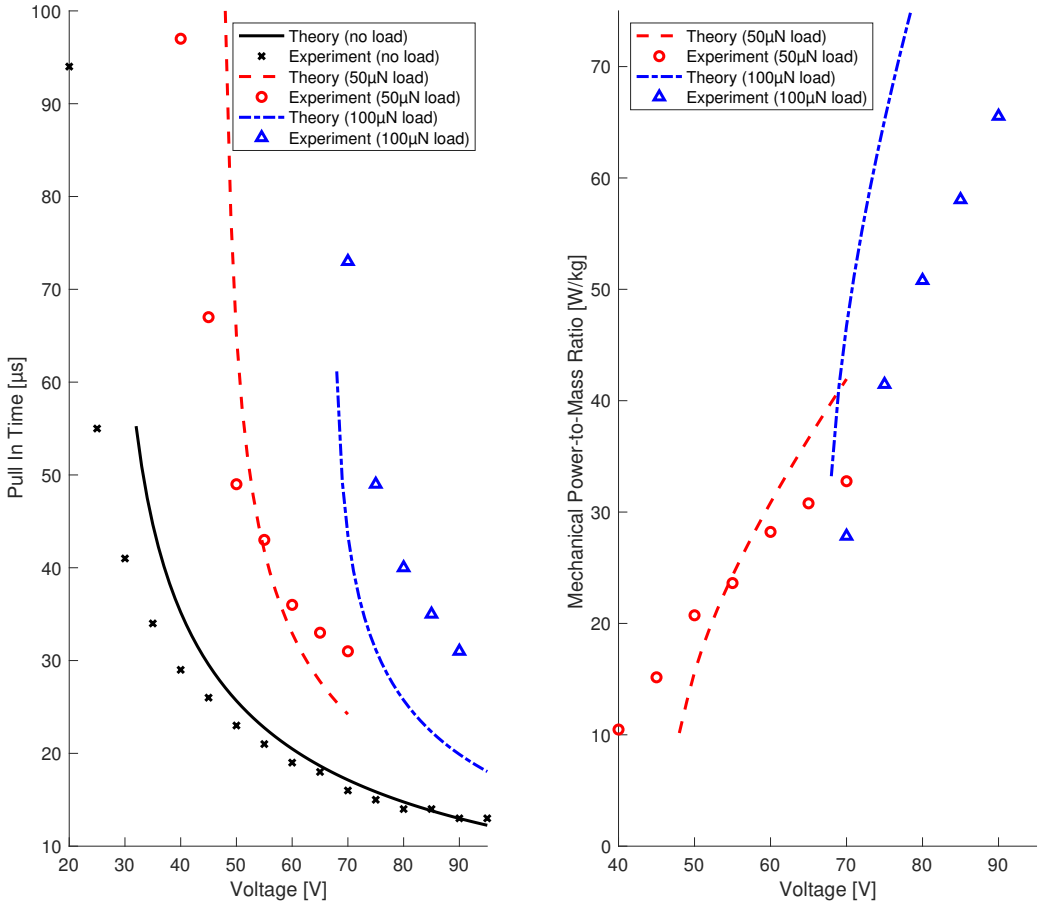

Figure 3.18: Measured pull-in times and mechanical power-to-mass ratios of gap closing actuators.

load, 50μN load force, and 100μN load force test structures, as well as simulations generated by solving Equation 3.10 in Matlab using the ode45 solver. Included in the model was a 0.48μm lateral DRIE undercut for all trenches greater than 4μm and 0.2μm lateral DRIE undercut for all trenches less than 4μm (as was estimated in Section 3.4). The mechanical power-to-mass ratios were calculated as

$$\frac{P_{mech}}{M} = \frac{F_{load}\Delta x_{shut}}{t_{pullin}}\frac{1}{M} \tag{3.21}$$

where M is the entire mass of the device layer GCA plus the mass of a rectangular bounding box made from substrate (and the substrate is assumed to have been thinned down to a thickness of 200μm).

The physics model of the loaded structures should be further investigated to understand the deviation from theory. Only three structures were tested in total (one for no-load, one for 50μN, and one for 100μN), possibly explaining the deviation.

Additionally, the power-to-mass ratio is inversely proportional to pull-in time, and therefore very sensitive to small deviations. Disagreements in pull-in time between the data and the simulation therefore show up as larger disagreements between power-to-mass data and simulation.

Chapter 4

The First Robot: Storing Energy in a Substrate Spring With Two On-board Electrostatic Inchworm Motors

4.1 System Overview

The purpose of this first robot [16], shown in Fig. 4.1 was to serve as a prototype platform and proof-of-concept capable of storing energy in a substrate spring using on-board electrostatic inchworm motors. Although the design was far from optimal, this robot was the first to achieve this goal. The robot has a mass of 90mg and is made in the SOI process from Section 1.5.

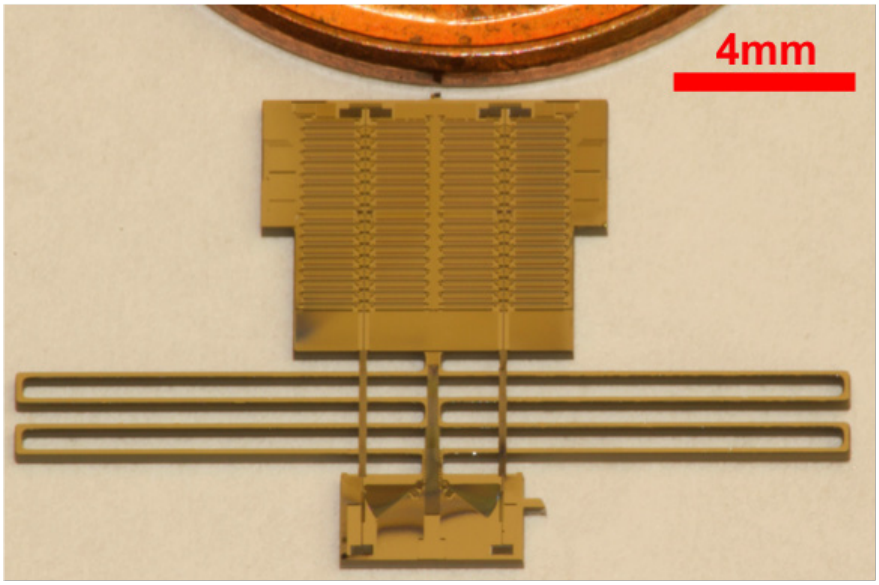

Figure 4.1: The robot next to a US penny.

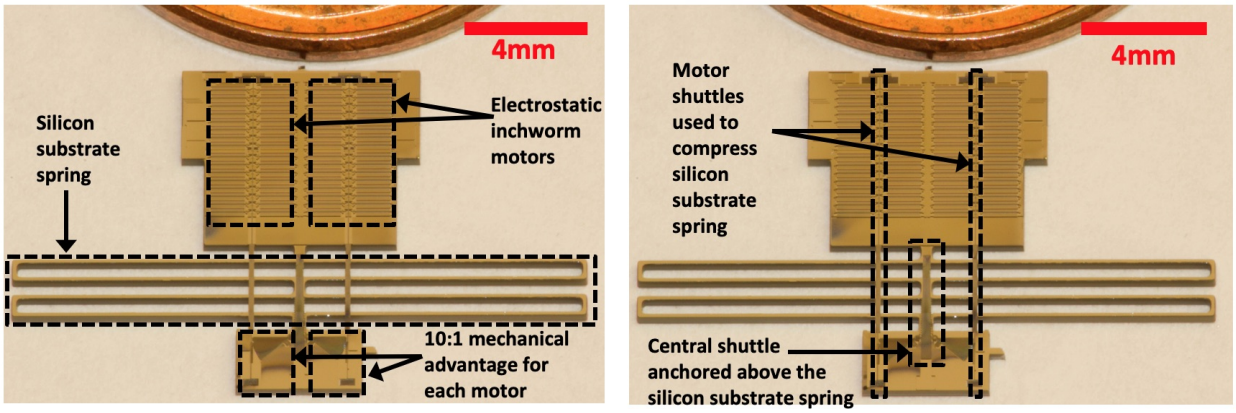

Figure 4.2: The robot's subsystems.

The robot's various subsystems can be seen in Fig. 4.2 and 4.3. Two electrostatic inchworm motors each with 32 gap closing actuators (as described in Section 3.3 of Chapter 3), two 10:1 mechanical advantage lever mechanisms [14], and the robot's central shuttle are made in the device layer. An energy storing spring designed to be compressed is etched into the substrate.

Each motor shuttle is coupled to a 10:1 mechanical advantage lever mechanism to increase the force used to compress the substrate spring. Each motor was designed to move its shuttle 900μm in total before resetting. The motors were designed to operate as follows: The first motor displaces its shuttle 500μm, at which point the beak on the lever it is coupled to contacts the robot's central shuttle (which is anchored to the robot above the substrate spring, and released below it). The first motor continues to displace its shuttle another 400μm. Because the lever provides a 10:1 mechanical advantage, the robot's central shuttle has displaced 40μm. The second motor now begins to actuate, and when the lever it is coupled to contacts the robot's central shuttle, the first motor resets. This process continues, and these 40μm displacements are accumulated; this accumulation of steps using electrostatic inchworm motors is called an "inchworm of inchworms [14]." The robot was designed to compress its substrate spring and jump as shown in Fig. 4.4.

The robot requires a minimum of five external signals: two high voltage signals for the first motor, two high voltage signals for the second motor, and a ground connection. Because the motors' ground pads are not internally connected with device silicon, in practice, six external wire are needed. These six signals could be reduced to five signals with either a wire bond, or using silver epoxy and SOI-Substrate windows as shown in Fig. 4.5.

4.2 Substrate Spring

While DRIE aspect ratios greater than 100:1 have been achieved [56], the substrate spring on this robot was designed and fabricated using a 200μm minimum feature size which is the same minimum feature size used by the SOIMUMPs commercial process [36]. The minimum

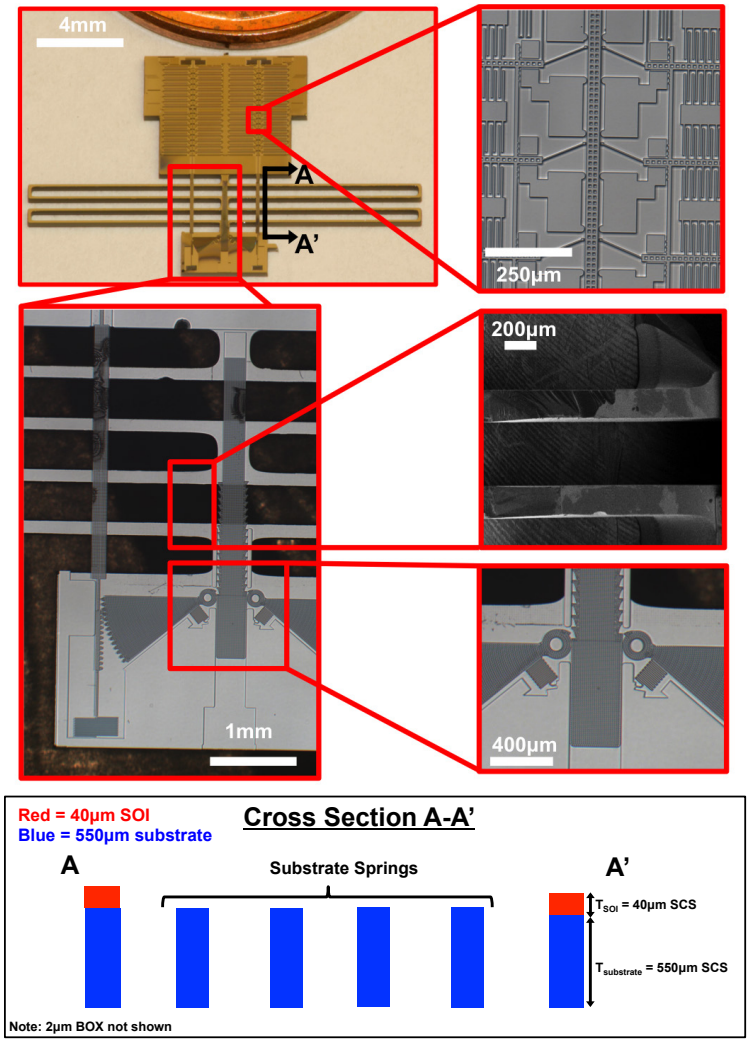

Figure 4.3: Counterclockwise starting from the top left. (1) The robot beneath a US penny. (2) The robot's left motor shuttle, both 10:1 mechanical advantage levers, central shuttle, and substrate springs are shown. (3) Cross section of A-A'. (4) Close-up of the two 10:1 mechanical advantage levers and the central shuttle. (5) SEM of a portion of the substrate springs. (6) The high density electrostatic inchworm motors used to compress the substrate springs.

feature size was reduced to 40μm for the robot in Chapter 5. Continuing to decrease the substrate DRIE minimum feature size while maintaining straight side walls [57] should be investigated by future researchers making substrate springs.

The spring on the robot was designed to have a spring constant of $380\frac{\text{N}}{\text{m}}$ with a maximum deflection of 800μm, theoretically resulting in 120μJ of stored energy. The maximum strain of the spring at a displacement of 800μm is approximately 0.15%, which is sub-optimal because

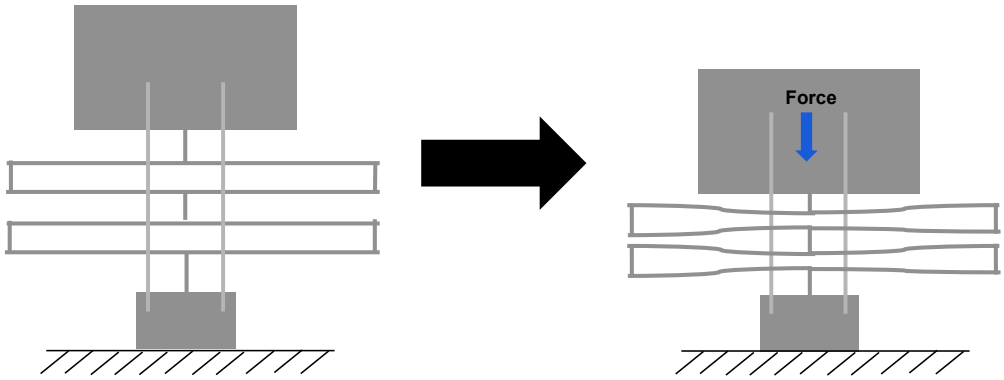

Figure 4.4: Cartoon of the robot's substrate spring (two box springs in series) being compressed and storing mechanical energy.

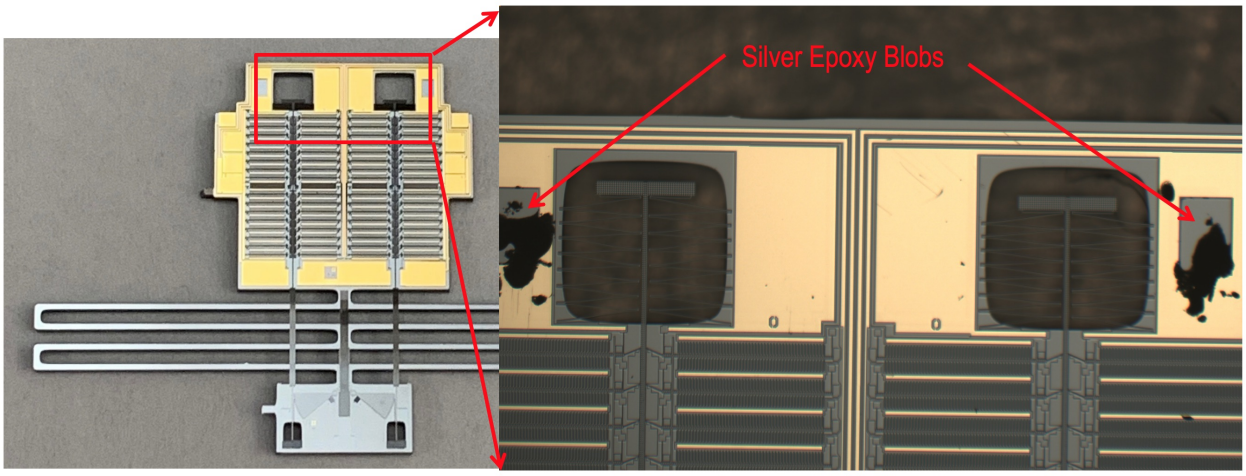

Figure 4.5: The substrate is used as a grounding plane to electrically connect two SOI pads. As a result, both SOI pads and the substrate can be grounded using a single external ground signal.

it is less than the 0.5% strain limit. Ideally, the spring would be designed to stretch to it strain limit, maximizing its stored energy per unit mass. In order to increase the maximum strain in a substrate spring, a weaker substrate spring must be designed and fabricated; this can be accomplished by using a smaller minimum substrate feature size, and this is done for the robot presented in Chapter 5.

Force vs. displacement of the silicon substrate spring on the robot was measured using a Dage 4000 wirebond tester. A plot of force vs. displacement for three fabricated substrate springs is shown in Fig. 4.6. The fitted slope of the measured data, $320\frac{\mathrm{N}}{\mathrm{m}}$, agrees to within 16% of the theoretical spring constant of $380\frac{\mathrm{N}}{\mathrm{m}}$. A spring constant of $320\frac{\mathrm{N}}{\mathrm{m}}$ displaced 800μm corresponds to 100μJ of stored energy.

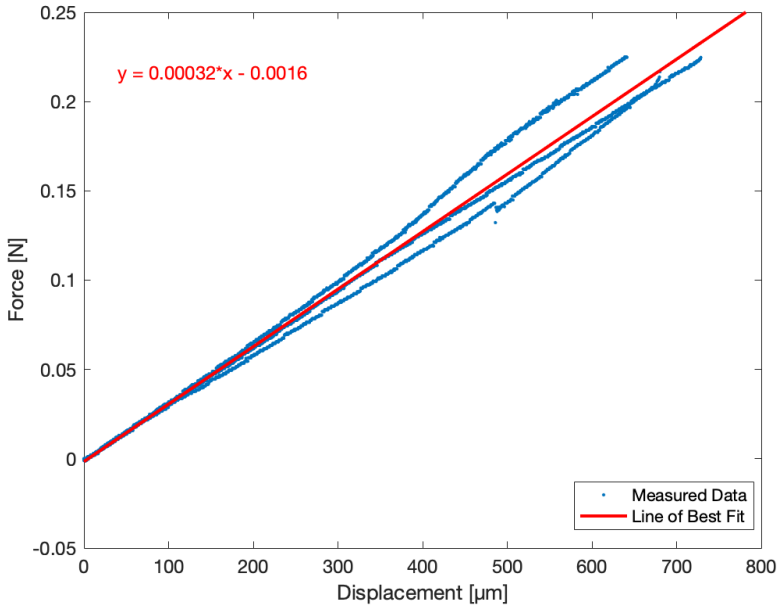

Figure 4.6: Force vs. displacement data for three measured substrate springs.

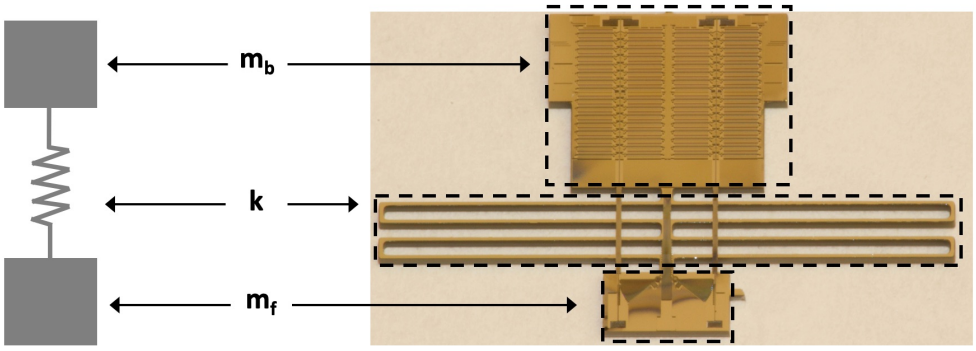

Figure 4.7: The jump model used in Equation 4.1.

4.3 Theoretical Jump Height

The two mass one spring jump model of the robot is shown in Fig. 4.7. The actual mass of the substrate spring is approximately 20 milligrams. In order to model the substrate spring as an ideal spring, its mass is split equally between the foot mass and the body mass. This results in a body mass of $m_b = 60$ milligrams and a foot mass of $m_f = 30$ milligrams. The motors on the robot can produce 15mN of force at 100V [51]. With motors that produce 15mN of force and 10:1 mechanical advantage, the robot should be able to deflect the substrate spring approximately 470μm and store 35μJ of energy.

Using Equation 2.33 to calculate the center-of-mass takeoff velocity of the robot, 35μJ of stored energy results in approximately $1\frac{\text{m}}{\text{s}}$. Equation 4.1 [58] is the limiting case of the Equation 2.38 when $C_d A \rho_{air} v^2 \sin^2(\theta) << 2mg$ (which is true for this robot). The vertical jump height h is a function of body mass m_b, foot mass m_f, substrate spring constant k, standard gravitational acceleration g, and spring displacement D.

$$h = \left(\frac{m_b}{m_b + m_f}\right)\left(\frac{\frac{1}{2}kD^2}{(m_b + m_f)g}\right) \tag{4.1}$$

If the substrate spring is manually compressed the full 800μm, the robot should be able to jump vertically about 8cm.

4.4 Manually Loaded Vertical Jump and Horizontal Mass Kick

Two experiments were conducted to test the energy storage of the robot's substrate spring: a manually loaded vertical jump, and a manually loaded horizontal penny kick (shown in Figs. 4.8 and 4.9, respectively). In both experiments the robot was constrained using glass slides to prevent out of plane motion. When compressed manually with tweezers in the vertical jump experiment, the robot jumped 4cm. While the robot should be able to jump 8cm vertically, the discrepancy is likely due to frictional losses in the glass slide setup as well as the robot contacting the tweezers during release. When compressed manually in the horizontal experiment, the robot kicked a US penny (2.5g) 7mm. The distance Δx that the penny should travel if only slowed by friction is given by

$$\Delta x = \frac{U_{\text{spring}}}{\mu_{\text{glass-penny}} m_{\text{penny}} g} \tag{4.2}$$

where U_{spring} is the energy stored in the substrate spring, $\mu_{\text{glass-penny}}$ is the coefficient of friction between the penny and the glass slide, and g is the standard gravitational acceleration. A 2.5g mass given 100μJ of kinetic energy from the substrate spring slowing only due to friction ($\mu_{\text{glass-penny}} = 0.4$, calculated by experimentally measuring the tilt angle at which the penny slides down the glass slide) should travel 10mm. The discrepancy is also likely due to frictional losses in the setup.

4.5 Electrostatically Loaded Substrate Spring and Horizontal Mass Kicks

The first demonstration of displacing a silicon substrate spring using SOI electrostatic inchworm motors is shown in Fig. 4.10. The left lever displaced the substrate spring a full 40μm, and the right lever displaced it an additional 20μm. The total displacement of 60μm

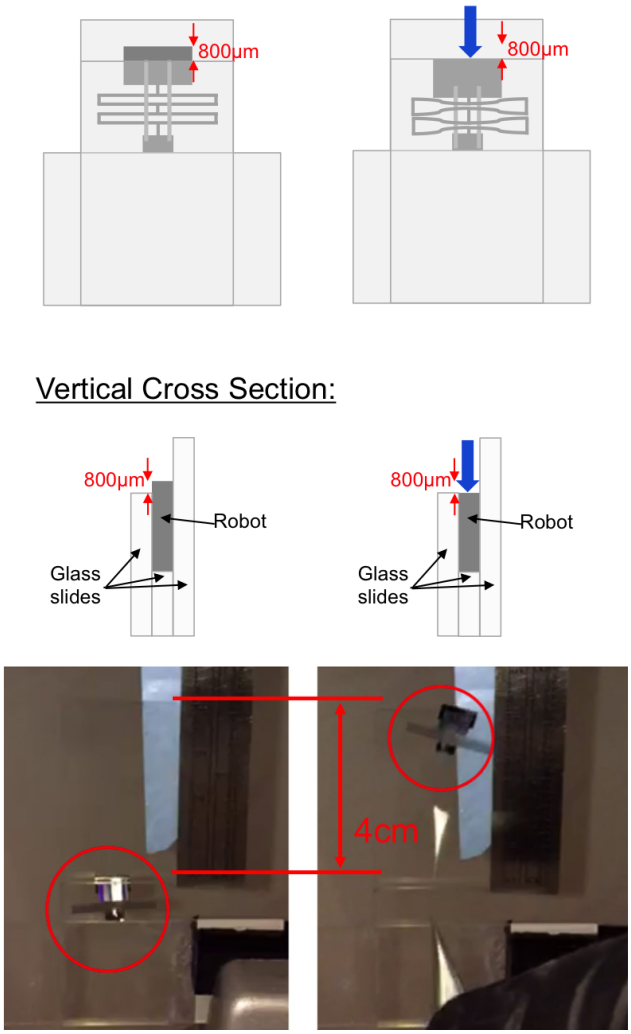

Figure 4.8: Top – Cartoon of manually compressing the robot's substrate spring with tweezers. The setup is perpendicular to the tabletop. Bottom – A fabricated robot's substrate spring is manually compressed 800μm, storing 100μJ of mechanical energy. The robot jumps 4cm.

resulted in 0.5μJ of stored mechanical energy. In this experiment, the robot was not able to compress its substrate spring any further because the left lever did not reset while the right lever was moving the central shuttle, thereby blocking it (middle bottom two images of Fig. 4.10). A 2.5 gram US penny (which is more than 25 times the mass of the robot) was placed on the probe station chuck next to the robot's foot; when the actuating voltage on the motors was removed, the energy in the substrate spring was released, and the penny was kicked 80μm. This corresponds to a coefficient of friction of about 0.3 between the penny and the metal probe station chuck.

The robot was also able to store approximately 1μJ by having its motors displace the

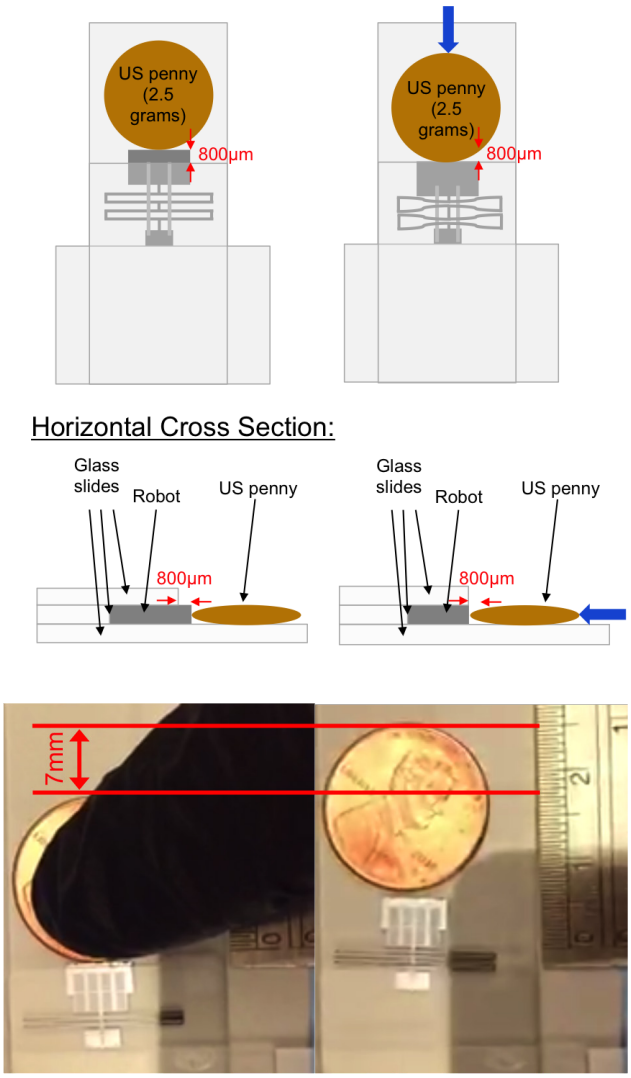

Figure 4.9: Top – Cartoon of manually compressing the robot's substrate spring with a US penny (2.5g). The setup is parallel to the tabletop. Bottom – The robot's substrate spring is manually compressed 800μm using a penny, storing 100μJ of mechanical energy. The robot kicks the penny 7mm.

robot's central shuttle two full 40μm steps (Fig. 4.11) and then kick an 0402 capacitor (0.6 milligram) a distance of 7mm (Figs. 4.12 and 4.13). The motors were only able to displace the robot's substrate spring by two 40μm steps because friction between the robot's central shuttle and the central shuttle's guide-rail prevented it from moving any further.

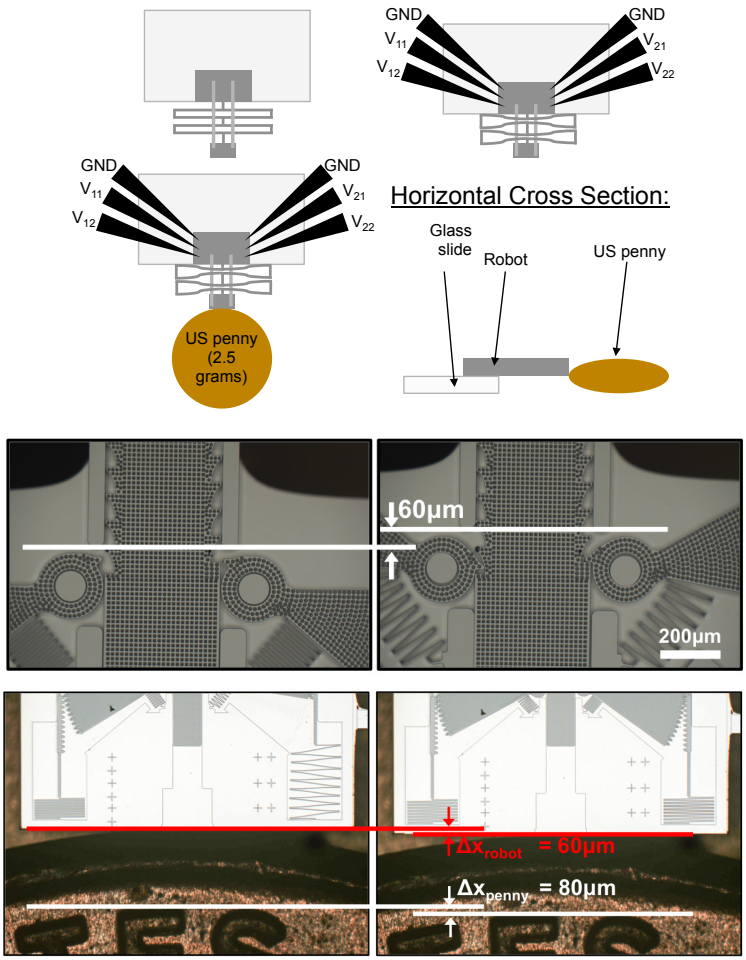

Figure 4.10: Top – Cartoon of the setup used to have the robot's electrostatic inchworm motors compress the substrate spring and kick a penny. The robot is glued to a glass slide with its substrate spring overhanging. The glass slide is put onto the probe station chuck, and micromanipulator probes apply control signals to actuate the inchworm motors. A penny is placed on the chuck next to the robot's foot. The control signals are removed, and the penny is kicked. Bottom – The robot's substrate spring is compressed 60μm. When the springs' energy is released the penny is kicked 80μm.

4.6 Lessons Learned

While this robot was never able to store enough energy using its on-board motors to jump, quite a lot was learned while developing this platform which informed many of the design decisions for the next version of the robot (Chapter 5). The main problems were:

1. Only one motor was active at a time. This meant that at any given time a significant portion of the robot's mass was not producing any useful work. If one motor could be

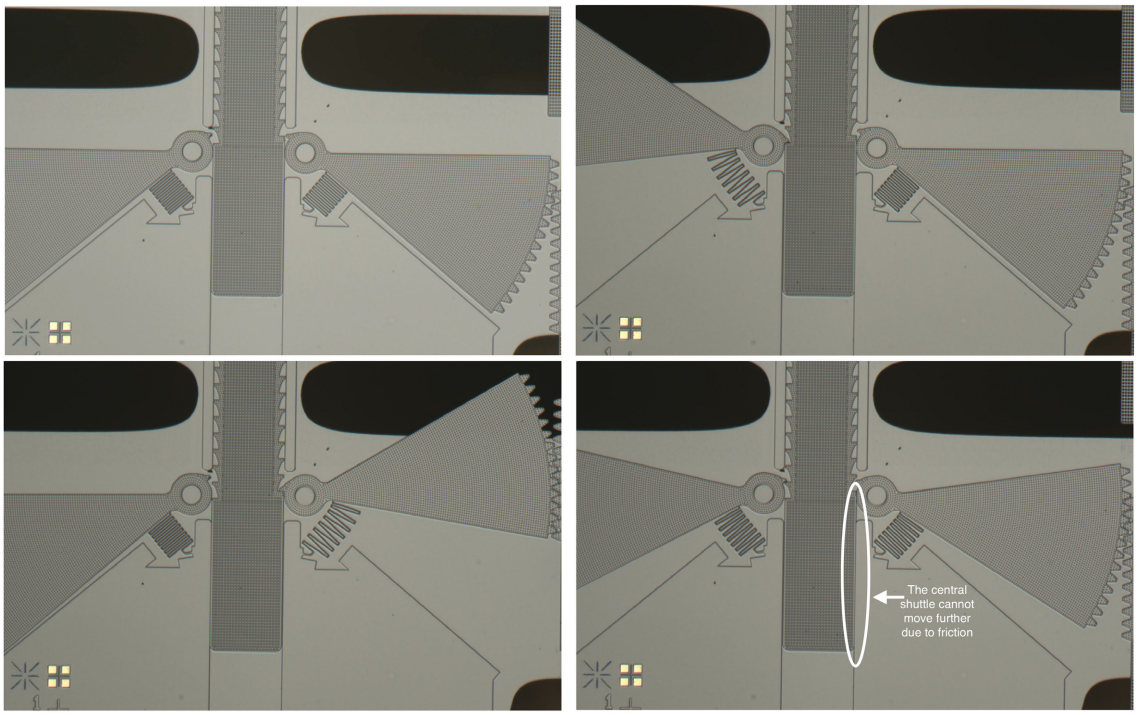

Figure 4.11: Top Left – The substrate spring is in its nominal position. Top Right – The robot's left motor displaced the substrate spring 40μm. Bottom Left – The robot's right motor displaced the substrate spring an additional 40μm for a total displacement of 80μm. Bottom Right – The left motor is unable to displace the substrate spring any further because the robot's central shuttle is jammed. Approximately 1μJ of energy was stored in the substrate spring.

removed from the design, then the decrease in weight would mean a higher jump height.

2. Five external control signals plus ground were needed. The difficulty of a attempting a successful tethered jump setup increases with each additional signal. Each additional signal requires an additional wire, wirebond, and solder joints, and all are susceptible to breaking.

3. Fabricating the robots had a low yield. The 1cm long, 34μm wide motor shuttles frequently broke during fabrication, and both motors must be functional for the robot to work as designed. The width of the motor shuttles should be made wider to make them more robust during fabrication.

4. Mechanical advantage is used to amplify the force output of the motors. This introduced additional friction into the system and prevented the robot's central shuttle from moving more than 80μm.

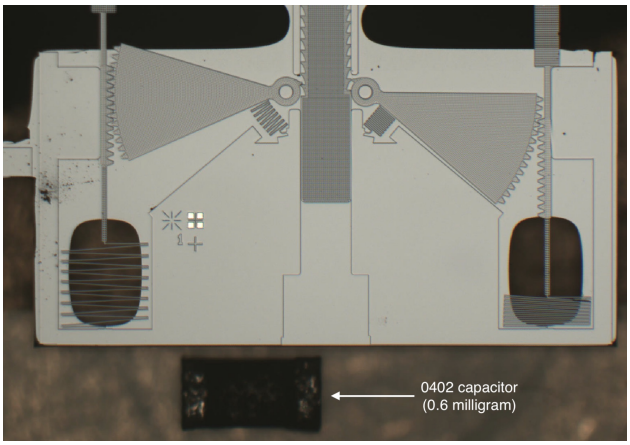

Figure 4.12: 1μJ of energy is stored to kick the 0402 capacitor.

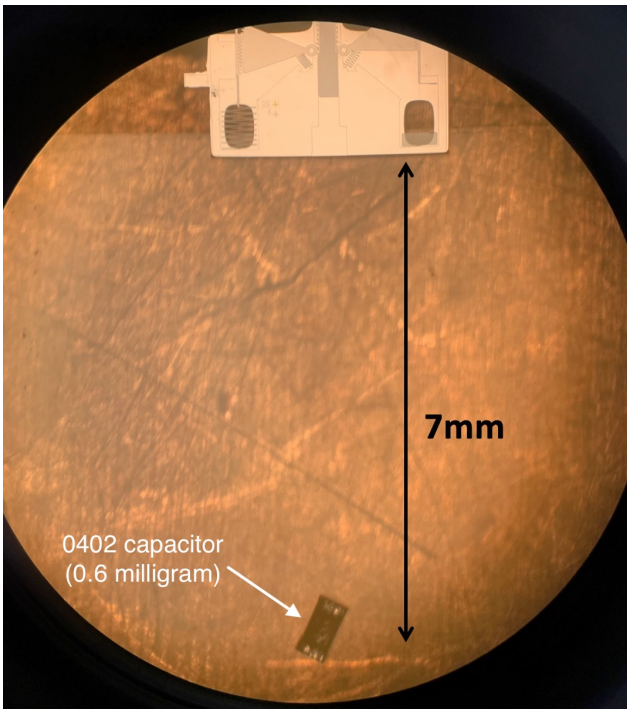

Figure 4.13: The robot kicked an 0402 capacitor (0.6 milligram) a distance of 7mm.

5. The substrate spring is very stiff because the minimum substrate DRIE feature size was 200μm. Increasing the substrate DRIE aspect ratio would allow for designing weaker springs, and in turn a larger amount of stored energy.

These problems are addressed in the design of the robot in Chapter 5.

Chapter 5

The Second Robot: Tethered Jumping Using a Substrate Spring and On-board Electrostatic Inchworm Motor

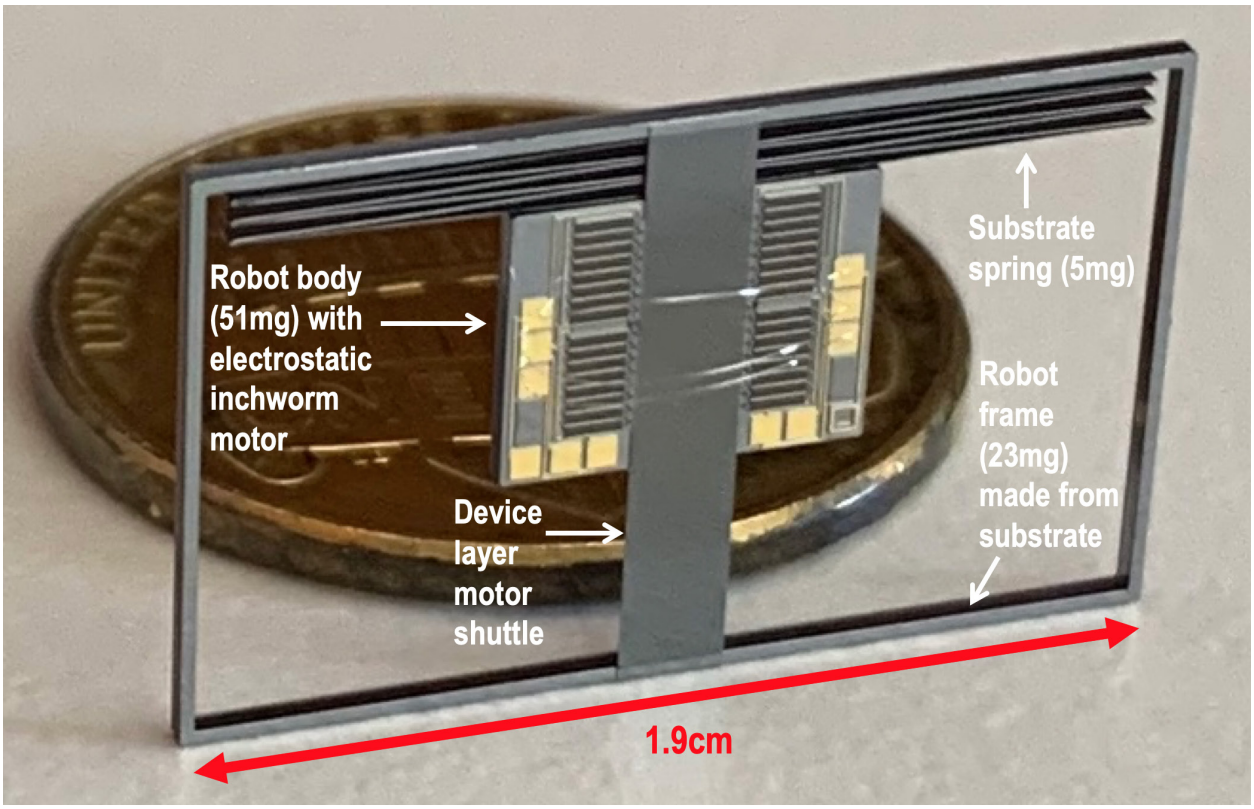

Figure 5.1: The 0.08 gram robot standing upright in front of a US Penny. The robot is approximately 1.9cm wide and 1.2cm tall.

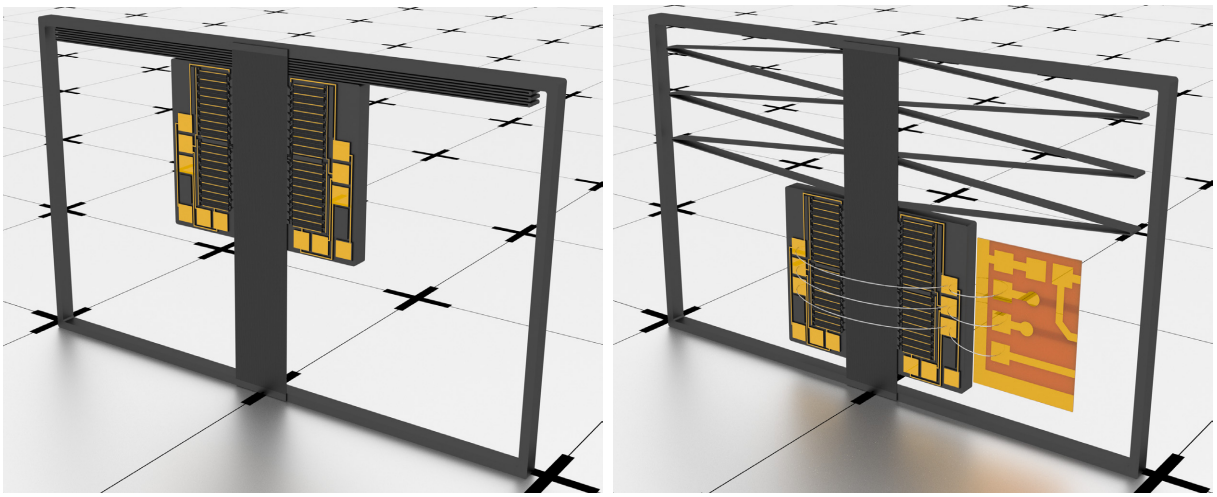

Figure 5.2: A 3D model of the robot. Left – The robot's substrate spring is in its relaxed position. Right – The robot's two motor halves are electrically connected using three wirebonds. The robot is also wirebonded to a breakout flex PCB, and the robot's electrostatic inchworm motor has displaced the substrate spring.

5.1 System Overview

The first successful jumps of a microrobot fabricated in a silicon-on-insulator process with an electrostatic inchworm motor in the device layer and an energy storing substrate spring etched into the silicon substrate are presented. The 0.08 gram silicon robot stored 8μJ of spring energy and vertically jumped more than 3mm when powered and controlled with wire tethers. The robot in this chapter (dubbed "R2") is a redesign of the robot in Chapter 4 (dubbed "R1") and addresses the issues that limited R1's performance. The main improvements of R2 are:

1. R2 has only one motor. R1 had two motors. One motor is better because it decreases the total system mass and increases the probability that the entire system works. Occasionally, during photolithography, a rogue dust particle would land on the SOI mask resulting in a bad pattern transfer to the photoresist. If this bad pattern transfer was not noticed before etching the SOI, the resulting motor would have fingers connected together that should not have been connected together. This would result in an entire GCA array not moving, and the motor would not work. The only way to fix this issue post-fabrication was to perform very careful surgery using a micromanipulator at a probe station and break the piece of silicon connecting the fingers together. One motor instead of two meant there was only half as much area for a rogue dust particle to land on and cause a catastrophic fabrication mistake.

2. R2 needs only two external control signals plus ground. R1 needed five external control signals plus ground. Requiring only three external signals instead of five significantly increases the likelihood of a successful tethered jump. This is because each additional

wire introduces additional wirebonds and solder joints into the system, which if broken are very tedious to fix, possibly resulting in a broken robot during a fix attempt. Also, each additional wire adds mass and tension to the robot as it jumps, lowering its jump height.

3. The width of the motor shuttle on R2 is 2mm, whereas the width of the motor shuttles on R1 were 34μm. Increasing the motor shuttle width increased the fabrication yield significantly. The 34μm shuttles on R1 frequently broke at locations where substrate silicon could unintentionally exert a force on them when the robots were removed from the wafer during fabrication.

4. R2 was designed to store approximately the same amount of energy that R1 was designed to store by trading less motor force for more spring displacement (5mm maximum displacement on R2 vs approximately 500μm displacement on R1). The substrate spring stiffness on R2 was designed to be approximately 100$\times$ less than the substrate spring stiffness on R1. Recall that $U_{spring} = \frac{1}{2}F\Delta x$. Unlike R1, R2 does not use any mechanical advantage and the substrate spring is directly connected to the output of the electrostatic inchworm motor. More displacement and less force means no need for mechanical advantage, which removed frictional losses in the system that prevented R1 from fully working as intended.

The microrobot's subsystems can be seen in Figs. 5.1 and 5.2. The core of the microrobot system is the electrostatic inchworm motor (capable of producing 15mN at 100V) and energy storing substrate spring, based on previous work in [51] and [16], respectively. The motor needs two high voltage signals and ground. Because the two halves of the motor on the robot are separated by the device layer motor shuttle, three wire bonds are needed to bridge the motor halves back together. Additionally, in order to interface the two high voltage signals to the robot, a small flex PCB with three 2 mil wires was wirebonded to the robot. When the robot is standing upright the motor pushes on the device layer motor shuttle, thereby separating the robot body and frame and storing energy in the substrate spring. When the substrate spring is fully displaced, its energy is quickly released causing the robot body to collide with the robot frame and jump.

5.2 Jumping Model

A dynamics model was created in MATLAB to simulate jumps. The model consists of one ideal spring with stiffness k and two point-masses: frame mass m_f and body mass m_b. The position of the frame mass x_f and the position of the body mass x_b are described by Equations 5.1 and 5.2. The initial displacement of the spring at time $t = 0$ is equal to D, and the standard gravitational acceleration is equal to g. The simulation begins with the initial conditions given by Equations 5.3 and 5.4. Each time a collision occurs between the frame mass m_f and the body mass m_b, the velocities $\dot{x_f}$ and $\dot{x_b}$ are reset according to conservation

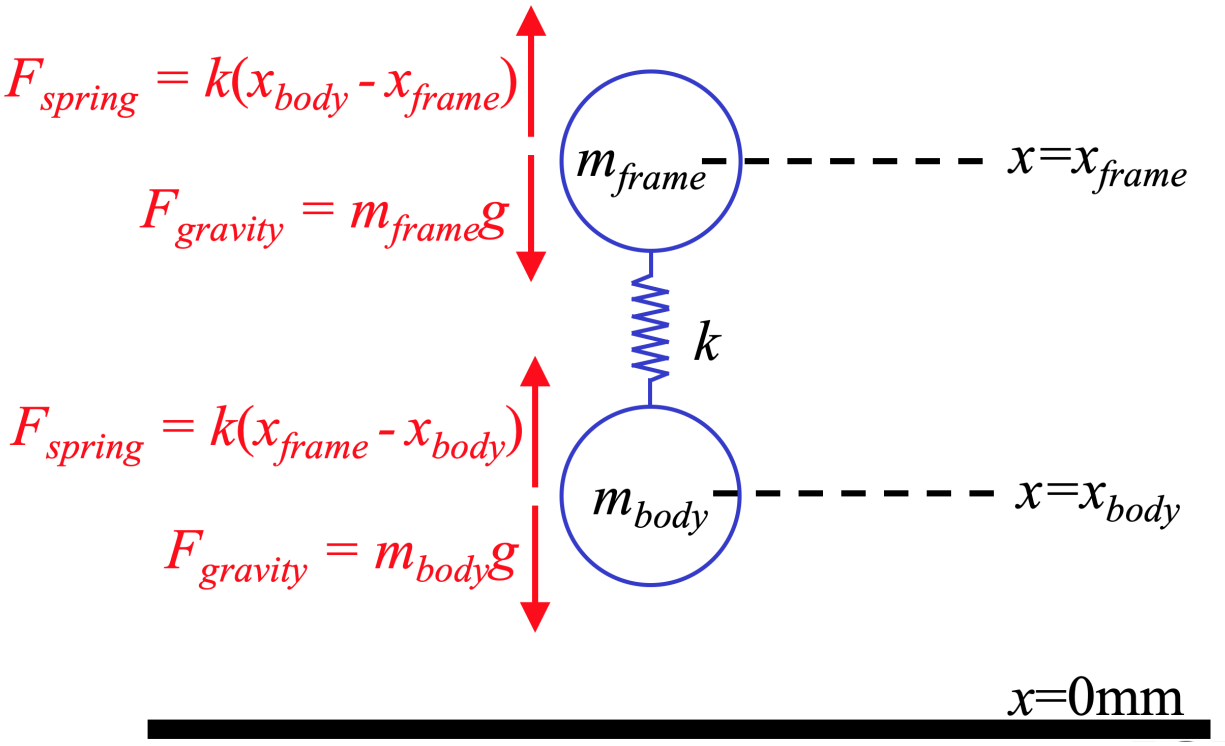

Figure 5.3: Free body diagram of the robot used in Equations 5.1 and 5.2.

of momentum with coefficient of restitution C_R, given by Equations 5.5 and 5.6. The frame mass and body mass velocities immediately after the collision, given by v_f and v_b, respectively, are functions of the frame mass and body mass velocities immediately before the collision, given by u_f and u_b, respectively. The net force on the frame mass m_f is made equal to 0 until the first collision occurs, thereby simulating the ground providing a normal force until takeoff occurs.

$$k(x_b - x_f) - m_f g = m_f \ddot{x_f} \tag{5.1}$$

$$k(x_f - x_b) - m_b g = m_b \ddot{x_b} \tag{5.2}$$

$$x_f(t=0) = D \ , \ \dot{x_f}(t=0) = 0 \tag{5.3}$$

$$x_b(t=0) = 0 \ , \ \dot{x_b}(t=0) = 0 \tag{5.4}$$

$$v_f = \frac{m_f u_f + m_b u_b + C_R m_b \left(u_b - u_f\right)}{m_f + m_b} \tag{5.5}$$

$$v_b = \frac{m_f u_f + m_b u_b + C_R m_f \left(u_f - u_b\right)}{m_f + m_b} \tag{5.6}$$

5.3 Design

A motor that produces force F_{motor} will displace a spring with stiffness k a distance $D = \frac{F_{motor}}{k}$. The energy U stored in the spring is given by Equation 5.7.

$$U = \int_0^D F_{spring}(x)\,dx = \int_0^D kx\,dx = \frac{1}{2}kD^2 = \frac{1}{2}F_{motor}D \tag{5.7}$$

The motor used in the robot design can produce 15mN of force and provide up to 5mm of travel. Therefore, the maximum energy that can be stored is 38μJ. The motor on R2 is exactly the same as the motors on R1, except that the motor shuttle was widened from 34μm to 2mm.

A spring made of 40μm wide fixed-guided beams etched into the 550μm thick silicon substrate was designed with a desired stiffness of $3\frac{\text{N}}{\text{m}}$. The spring is a box spring (Fig. 2.11) with $N = 3$, $w = 40\mu$m, and $L = 8.75$mm. The mass of the substrate spring is split in half and lumped into m_b and m_f. The mass m_b consists of the robot body silicon (51mg), flex PCB (10mg), three 2 mil wires (5mg), and half of the substrate spring silicon (3mg). The mass m_f consists of the robot frame silicon (23mg) and half of the substrate spring silicon (3mg). The parameters used in the MATLAB model to simulate the design were $m_b = 69$mg, $m_f = 26$mg, $k = 3\frac{\text{N}}{\text{m}}$, and $C_R = 1$. The simulated jump height was approximately 3cm.

5.4 Tethered Jumping

A confocal microscope was used to measure a fabricated spring's beam width (Fig. 5.4) from both the device layer side and substrate side, measured to be 21μm and 30μm, respectively. The beams were drawn in layout to be 40μm, and the reduction in width after fabrication was likely due to undercutting of the photoresist and a re-entrant etching profile during DRIE. With a trapezoidal cross-section (see Equation 2.26) and a Young's modulus of 130GPa [41] (due to a wafer manufacturing error, the Young's modulus was smaller than intended because the spring was fabricated parallel to a {100} plane of a (100) wafer instead of a {110} plane), the spring stiffness was calculated to be $0.6\frac{\text{N}}{\text{m}}$. Because the energy stored by a spring is linearly proportional to its stiffness (for a fixed distance D), the energy stored by a spring with a stiffness of $0.6\frac{\text{N}}{\text{m}}$ will store $\frac{0.6}{3} = 20\%$ of the energy stored by a spring with stiffness $3\frac{\text{N}}{\text{m}}$. This significantly reduces the theoretical jump height from a few centimeters to a few millimeters. The robot being tested in a probe station is shown in Fig. 5.5. Note that three wirebonds were used to connect the two motor halves together.

The assembly steps to prepare the robot for tethered jumping were:

1. Solder three 2 mil diameter insulated wires to three male headers. Each of the three wires was approximately 40cm. One mil diameter wire could have been used, however it was much more fragile and broke much more easily than the 2 mil diameter wire.

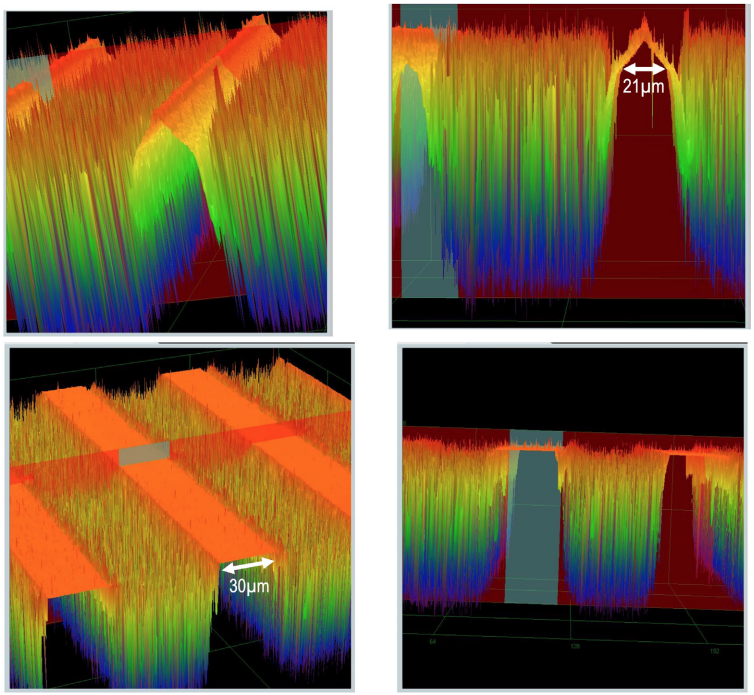

Figure 5.4: Partial 3D reconstruction of a robot's substrate spring using a confocal microscope. Top – The width of the spring's beam when measured from the top (i.e. the device side) was 21μm. Bottom – The width of the spring's beam when measured from the bottom (i.e. the substrate side) was 30μm. The "grass" is noise and appears because the microscope cannot see inside the 550μm deep trenches.

2. Attach a piece of 0.7mm thick carbon fiber stiffener to the backside of the breakout flex PCB. A very small dot of Loctite Super Glue ULTRA Gel Control was used. Because the carbon fiber is heavy, the minimum amount needed should be used. A piece equal to the size of the flex PCB was used.

3. Apply solder paste to the vias on the breakout flex PCB. With one hand, insert the first wire into its via on the flex PCB, and with the other hand, use an iron to heat the solder. An iron was used instead of a reflow oven to prevent the entire flex PCB from heating and warping. Repeat for the other two wires.

4. Place the robot and flex PCB on the wirebond chuck. Connect the two motor halves together with three wire bonds. Keep the robot on the wirebond chuck for the next step.

5. Wirebond the flex PCB to robot. Note: only one wire bond was needed for each of the three electrical connections, but four wirebonds per connection were used for extra mechanical rigidity. It was discovered that the flex PCB would very easily break off of

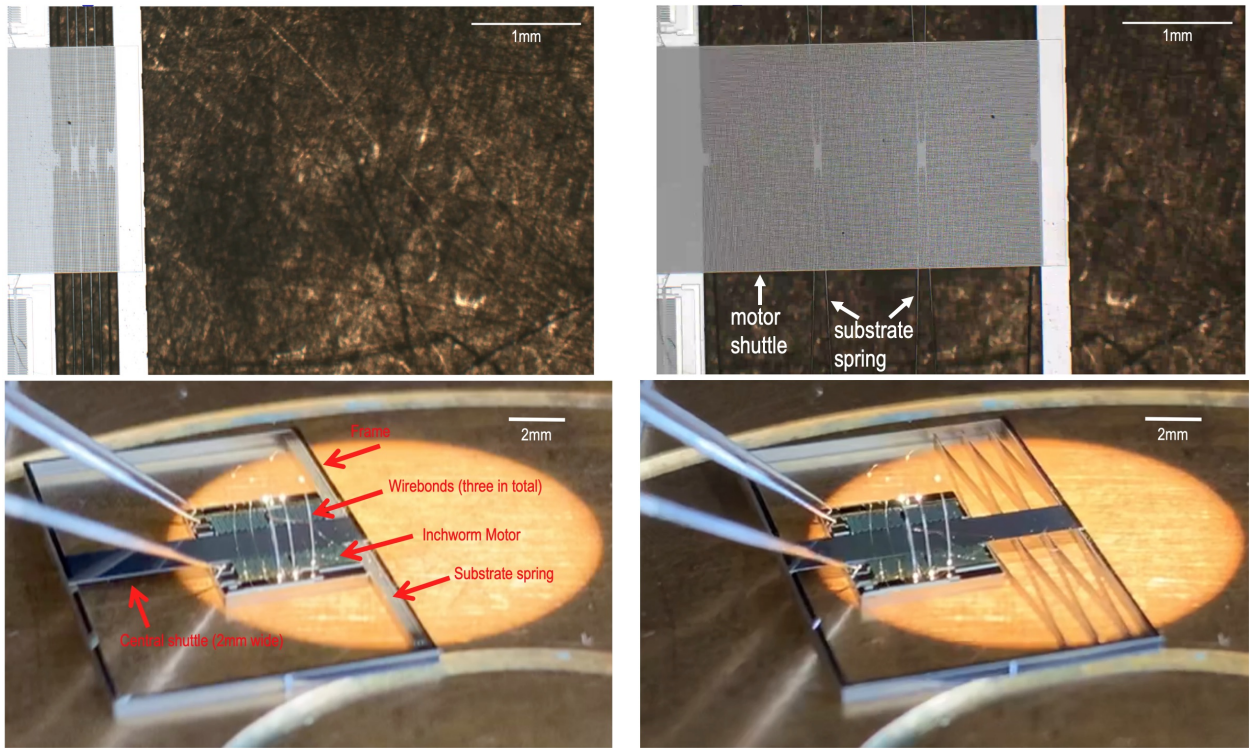

Figure 5.5: The robot being tested at a probe station. Three tungsten probe tips were used to actuate the motor: two high voltage signals and ground. The robot's on-board electrostatic inchworm motor displaced the substrate spring approximately 3mm. Top – Top down view from the probe station camera. Bottom – Perspective view from an external camera.

the robot when trying to setup the robot for tethered jumps if only one bond was used per connection.

The robot being wirebonded can be seen in Fig. 5.6. The test setup for conducting tethered jumps is shown in Fig. 5.7. The robot using its on-board motor to displace its substrate spring 5mm from its relaxed position is shown in Fig. 5.8. High speed images of a 3.6mm $\pm$ 0.2mm jump can be seen in Fig. 5.9. The simulated MATLAB model using a spring stiffness of $0.6\frac{\text{N}}{\text{m}}$ and coefficient of restitution $C_R = 0.3$, as well as an experimentally measured trajectory are shown in Fig. 5.10. The measured data matches the simulation well, with discrepancy from the MATLAB model possibly due to unmodeled friction between the robot and the paper used for measuring jump height. Using its on-board electrostatic motor, this robot has jumped more than 3$\times$ higher than the the previous best jumping SOI microrobot [14].

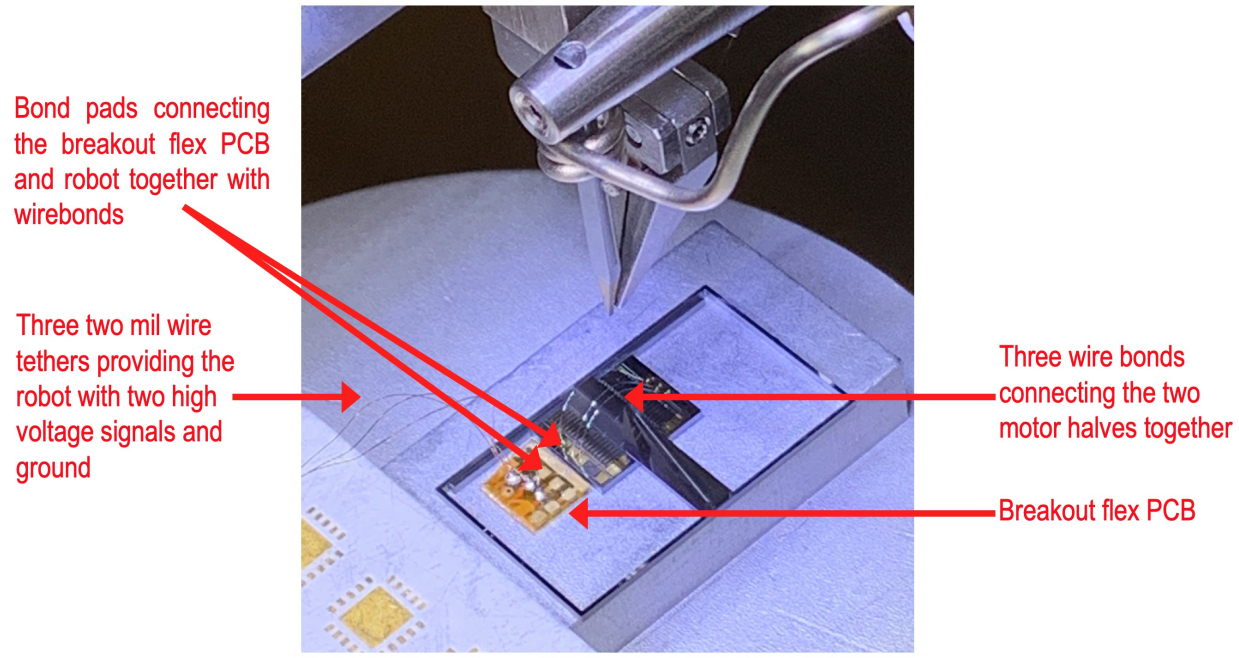

Figure 5.6: The robot lying flat on a wirebonding chuck. The robot is being joined to the breakout flex PCB with wirebonds.

5.5 Conclusion

The same robot has successfully jumped five times, proving itself to be resilient to the repeated impulse imparted to it, physically falling over, and operating for multiple hours outside of a cleanroom environment.

The immediate next step is to change the design and/or fabrication process to create a substrate spring with a stiffness of $3\frac{\mathrm{N}}{\mathrm{m}}$ so that this robot design can jump 3cm.

Following a successful 3cm jump, the fabrication process will have an alumina atomic layer deposition step added [40] as mentioned in Section 3.6 of Chapter 3. This step will insulate the electrostatic motor's capacitive fingers. If the fingers are insulated, they will not short if touched; this would allow the motor to be designed with much smaller gaps, and therefore much higher force output. Additionally, because the fingers will not bend and short, the actuation voltage may be increased from 100V to 200V, further increasing the force output of the motors. The combined effects of a smaller initial front gap and increased applied voltage can increase the motor force output by a factor of 20. As explained in Section 2.8 of Chapter 2, the output force of this motor would be strong enough (>250mN) to displace a substrate spring with a spring constant of $19\frac{\mathrm{N}}{\mathrm{m}}$ a distance of 1.3cm; this would result in enough stored energy for this robot to jump 1 meter vertically into the air.

Finally, integrating the robot with solar cells [34] for power and a CMOS brain [35] will make it a truly autonomous system. This is discussed in Chapter 6.

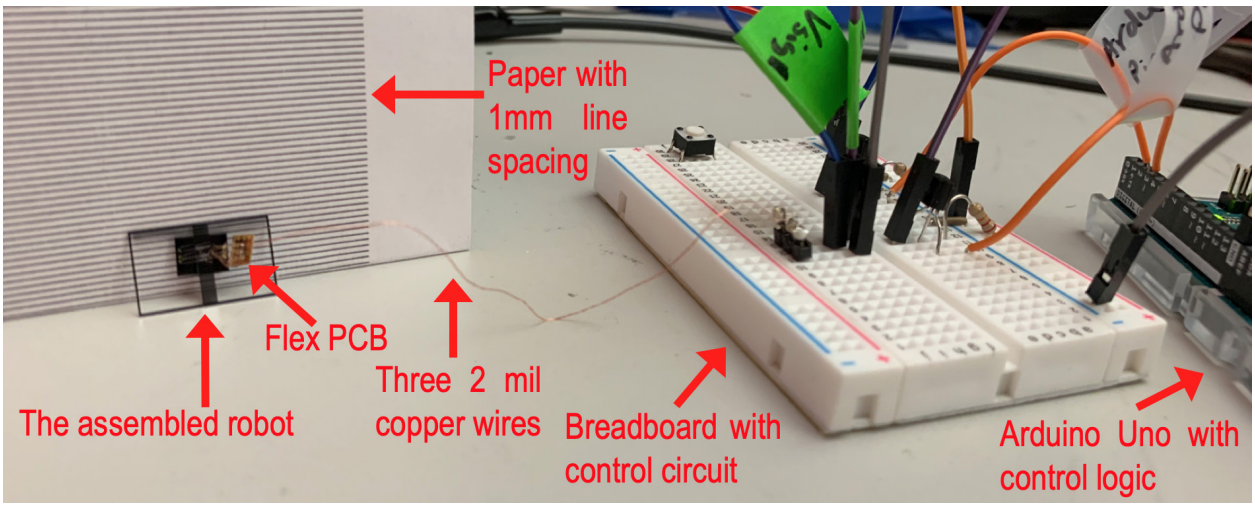

Figure 5.7: The test setup for conducting tethered jumps. A flex PCB is wire bonded to the robot's signal pads. Power is provided by the control circuit via the three 2 mil wires connected to the flex PCB.

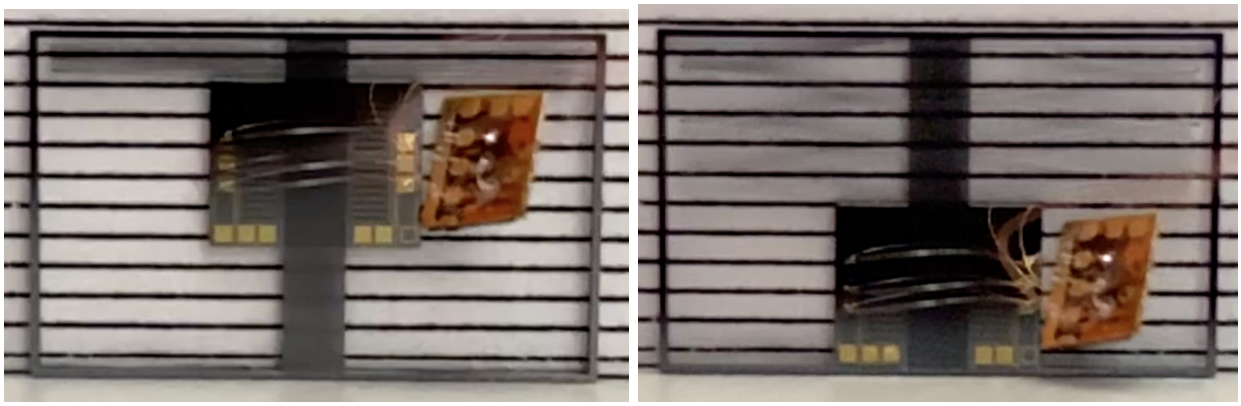

Figure 5.8: The robot used its on-board motor to stretch its substrate spring in a tethered jump setup. The robot is standing upright in front of a piece of paper with 1mm vertical line spacing. Left – The robot has not yet used its on-board motor to stretch the substrate spring. Note the approximately 1mm droop of the substrate spring from its relaxed position due to the weight of the robot body silicon, flex PCB, and three 2 mil wires. Right – The robot's electrostatic inchworm motor has displaced the substrate spring 5mm from its fully relaxed position. The spring stored approximately 8μJ of energy.

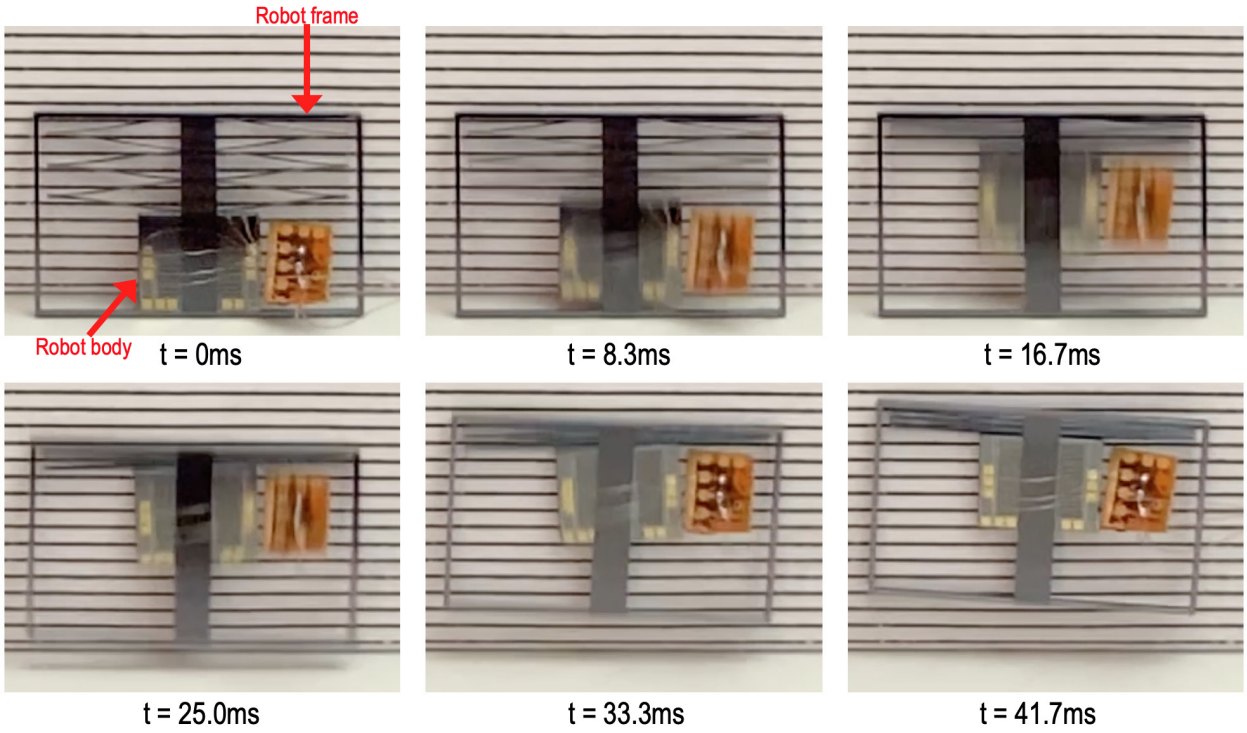

Figure 5.9: Six high speed (240 frames per second) images of a tethered jump in front of a piece of paper with 1mm vertical line spacing. Top Left – The robot used its electrostatic inchworm motor to displace its substrate spring by 5mm at a rate of 100μm/s. An estimated 8μJ of spring energy was stored. Top Center – The robot body accelerated upwards towards the robot frame. Top Right – The robot body collided with the robot frame. Bottom Left – The robot began jumping into the air. Bottom Center – The robot continued to travel upwards. Bottom Right – The robot jumped 3.6mm $\pm$ 0.2mm.

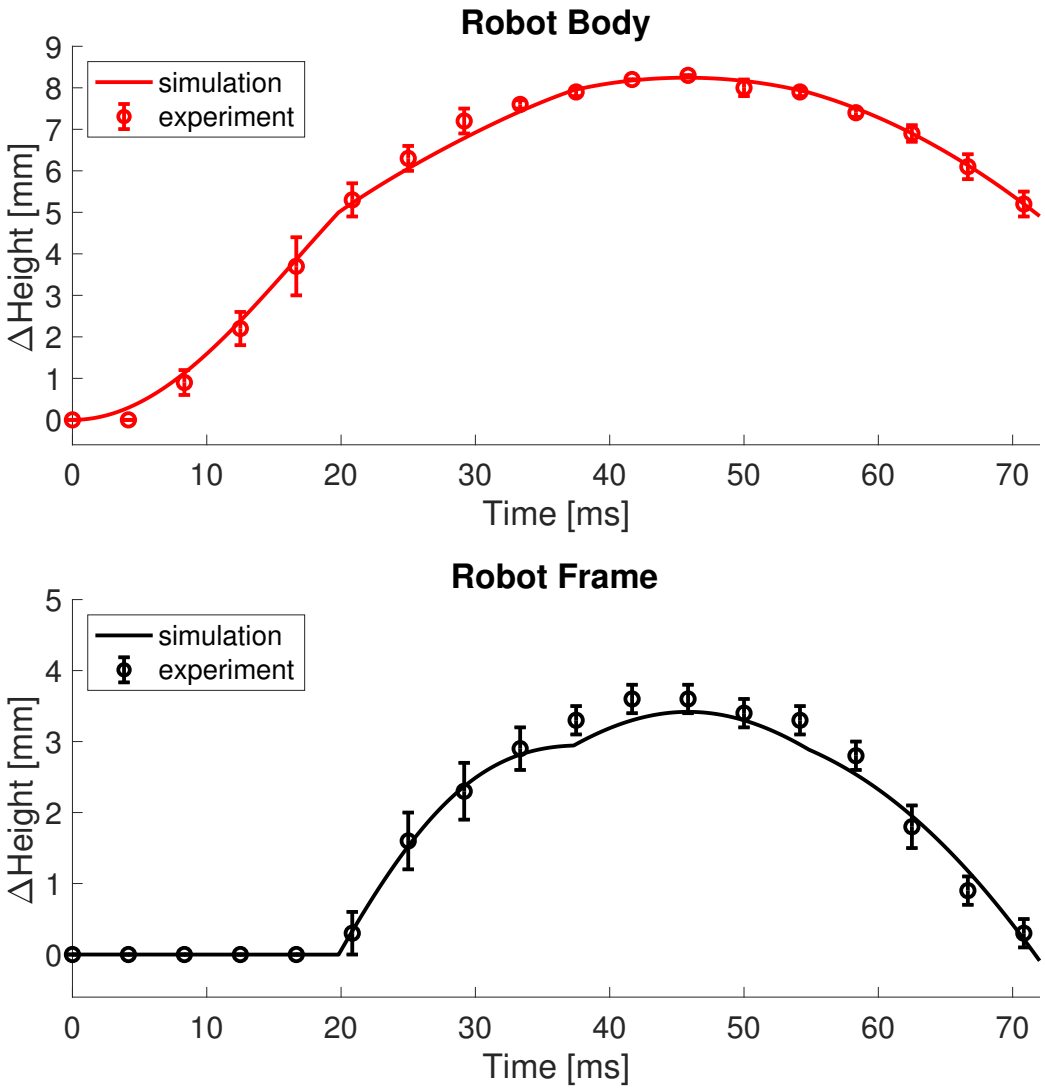

Figure 5.10: MATLAB simulated and experimentally measured height changes of the robot body and robot frame during the jump shown in Fig. 5.9. The error bars show position uncertainty ranges (measured with 0.1mm resolution) due to image blurring and the data points show the midpoints of the ranges.

Chapter 6

Towards Autonomy

6.1 Three Chip Integration: MEMS Robot, CMOS Solar Cells, and CMOS Microprocessor and Radio

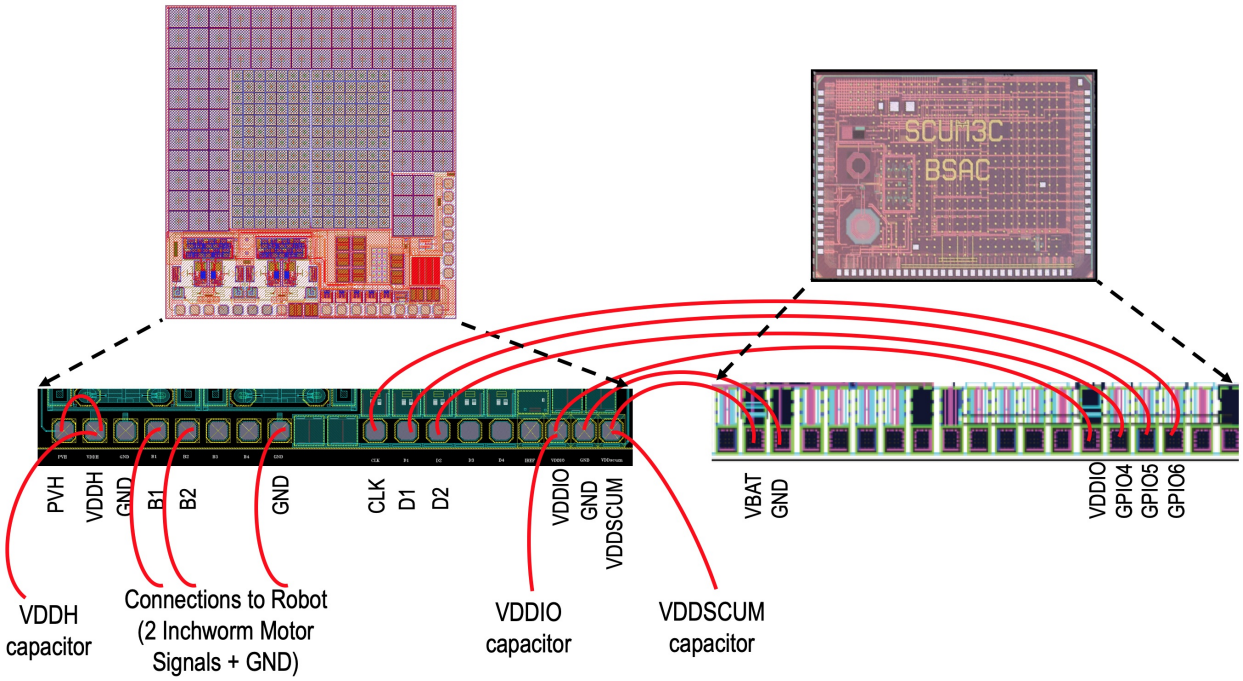

Figure 6.1: The required connections needed to make an autonomous jumping microrobot with a CMOS solar cell chip [34] and CMOS brain [35] with an IEEE 802.15.4 radio transceiver with limited Bluetooth Low Energy transmit capability.

Hollar [17] created one of the first autonomous microrobots by combining a MEMS robot, digital sequencer, and solar cells. However, this robot did not have a general microprocessor

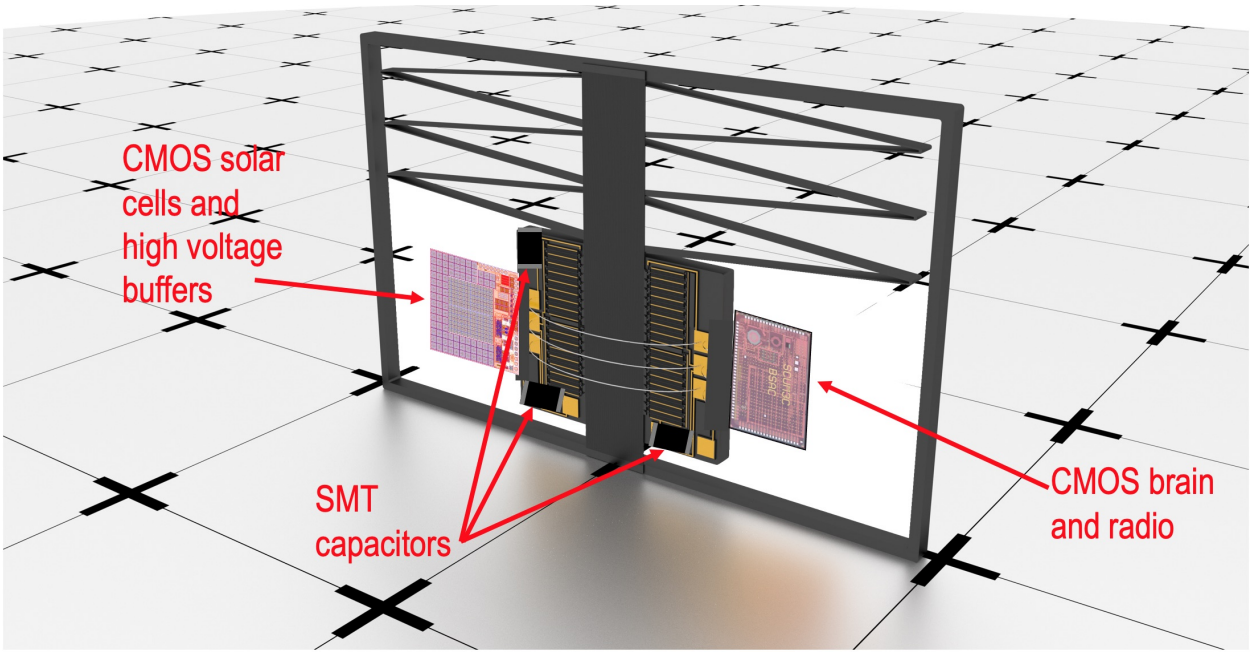

Figure 6.2: A 3D model of a robot integrated with a solar cell chip [34] and CMOS brain [35]. The robot, brain chip, and solar cell chip could be joined with glue or epoxy. Also shown are three SMT capacitors needed for the solar cell supplies. The necessary connections from Fig. 6.1 are not shown.

to run arbitrary programs or control algorithms, and did not have a radio to communicate with other robots or the outside world. Additionally, the fabrication consisted of a polysilicon process in addition to an SOI process.

Recent progress in CMOS solar cells [34] and low power wireless sensor nodes [35] makes possible the realization of autonomous microrobots capable of general computation and wireless communication using the three mask SOI process presented in this dissertation. The solar cell chip in [34] is approximately 3mm×3mm, and has three voltage domains. The wireless sensor node in [35], also known as the "single chip micro mote," or SCμM, is approximately 3mm×2mm, and contains a Cortex-M0 microprocessor and an IEEE 802.15.4 radio transciever with limited Bluetooth Low Energy transmit capability. The three voltage domains on the solar cell chip, VBAT, VDDIO, and VDDH, can supply power to the core SCμM system, the GPIOs on SCμM, and the actuators on a robot, respectively. Under 1 sun of illumination, VBAT supplies approximately 1.5V, VDDIO supplies approximately 3V, and VDDH supplies approximately 120V.

Fig. 6.1 shows the necessary connections that must be made between the solar cell chip [34], wireless sensor node [35], and jumping robot. In addition to the two CMOS chips, three SMT capacitors are needed to prevent the supply voltages from dropping too much when they provide current. While these two CMOS chips have not been fully integrated into a robot yet, the MEMS gripper shown in Chapter 3 has been successfully operated using the solar

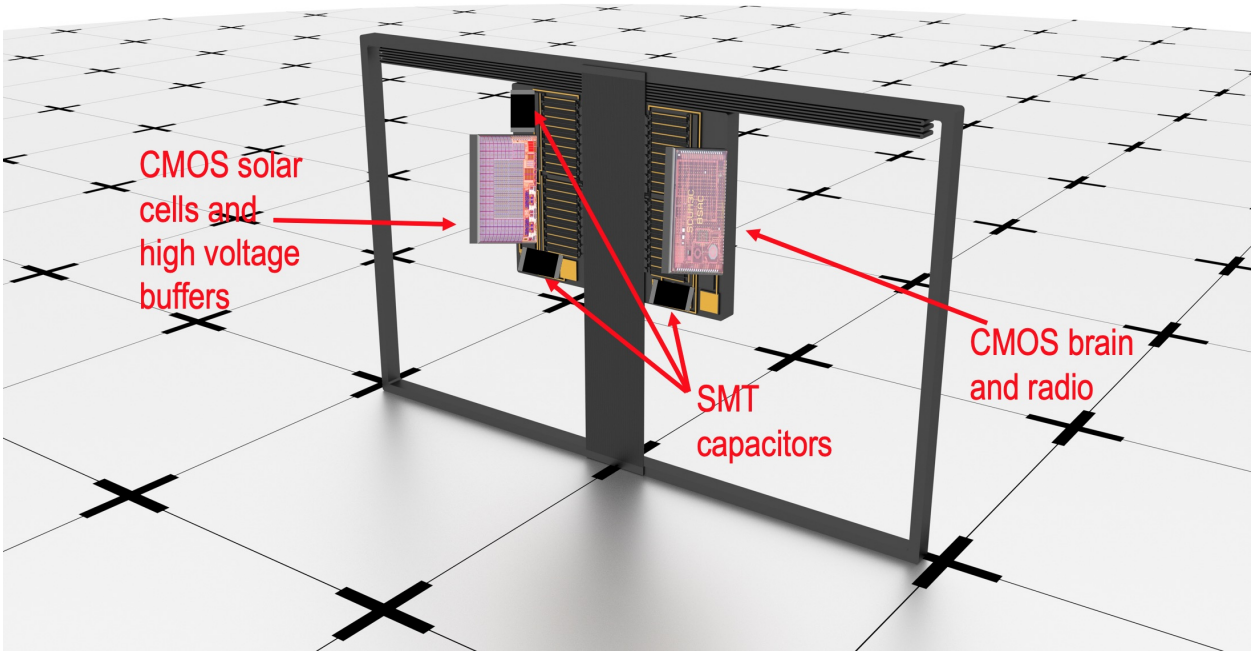

Figure 6.3: A 3D model of a robot integrated with a solar cell chip [34] and CMOS brain [35] using two ZIF sockets [59]. The chips are inserted perpendicularly to the robot. Also shown are three SMT capacitors needed for the solar cell supplies. The necessary connections from the two CMOS chips to the robot shown in Fig. 6.1 are made via the probes on the ZIF sockets. Additional on-board routing can be made with wirebonds or zero-ohm resistors.

cell chip (with approximately 2 suns of illumination) and CMOS brain, with each chip on a separate custom PCB. The capacitor values used were 22μF, 22μF, and 100nF, on VDDIO, VBAT, and VDDH, respectively.

Integrating the two CMOS chips and the robot could be done in multiple ways. The simplest way involves affixing the the two chips to the side of the robot body using glue or epoxy, and subsequently making the ten necessary connections with wirebonds. This type of integration is shown in Fig. 6.2.

Another integration method is to use zero insertion force MEMS sockets [59], also known as ZIF sockets. The sockets would be etched into the robot, and the CMOS chips would be inserted perpendicularly to the robot. The sockets provides mechanical alignment between the robot and CMOS chips, while the spring loaded microfabricated probes etched into the device layer of the sockets make electrical connections with the pads on the CMOS chips. This type of integration is shown in Fig. 6.3. A significant benefit of this integration method is that no wirebonds are needed to connect the pads on the CMOS chips to the robot.

The robot in Chapter 5 operated its motor at a speed of 100μm/s for all tethered jumps performed thus far. Because the substrate spring needs to be displaced approximately 5mm, a speed of 100μm/s means at most one jump can occur every 50s. The motor on the robot has been operated at 1mm/s, hypothetically corresponding to one jump every five seconds.

Other angled arm electrostatic inchworm motors displacing their shuttles at 3.5cm/s have been previously demonstrated [49]. If the inchworm motor on the jumping microrobot in Chapter 5 could achieve a speed of 3.5cm/s then it could displace its substrate spring 5mm in only $1/7^{\text{th}}$ of a second, while requiring approximately 12mW of electrical input power.

The solar cell chip [34] above can provide approximately 0.3mW of power to the inchworm motor under one sun of illumination, corresponding to a shuttle speed of approximately 1mm/s and therefore approximately one jump every five seconds. However, currently SCμM requires two suns of illumination to operate when using the chip from [34]. With a redesigned solar cell chip, SCμM will be able to operate continuously in one sun of illumination.

If a new 3mm×3mm chip completely covered in solar cells was made, and assuming 20% solar to electrical conversion, then it could harness approximately $0.3\text{cm} \times 0.3\text{cm} \times 100\frac{\text{mW}}{\text{cm}^2} \times 20\% = 1.8\text{mW}$ of electrical power, corresponding to a shuttle speed of 5mm/s and one jump per second. If the robot was equipped with 1cm^2 of a thin-film battery capable of storing $6.98\frac{\text{mWh}}{\text{cm}^2}$ [33], then after approximately four hours in one sun of illumination the robot would have stored enough energy to jump one time per second for approximatley four hours straight.

6.2 Designing an Autonomous Microrobot Capable of Vertically Jumping 1 Meter

Energy storage, motors, and robot prototypes capable of kicking weights and tethered jumps were presented in the previous chapters. The future steps required to design and build a 100 milligram robot that can vertically jump 1 meter are summarized. The resulting robot would look very similar to the robot presented above.

1. Design a substrate spring that stores 1.6mJ when stretched 1.3cm. This can be accomplished by making a box spring with $N = 4$, $w = 85\mu\text{m}$, $L = 9.1\text{mm}$, and $T = 550\mu\text{m}$, resulting in a stiffness of $19\frac{\text{N}}{\text{m}}$. The difference between this new spring and the spring currently on the robot would be barely noticeable to the naked eye.

2. Make a motor that can produce 250mN of force. This can be accomplished by removing the $1\mu\text{m}$ final gap in the current motor design, insulating the fingers with alumina, and increasing the applied voltage from 100V to 200V. The resulting motor would have a total finger capacitance of approximately 1.7nF when all gaps are closed and a CV^2f power draw of approximately 20mW when running at 200V and 1.3mm/s. If the robot was equipped with a redesigned 3mm×3mm solar cell chip as discussed above capable of providing 1.8mW of power to a 1cm^2 thin-film battery capable of storing $6.98\frac{\text{mWh}}{\text{cm}^2}$ [33], then after less than 4 hours in one sun of illumination the robot would have stored enough energy to vertically jump 1 meter every ten seconds for approximately 20 minutes.

3. Integrate with SCμM and the solar cell chip. This could potentially be accomplished in many ways: using glue and wirebonds, MEMS ZIF sockets [59], or another yet to be

developed technology. In the future, a combined SOI MEMS-CMOS process [38] could be used to design the robot, CMOS brain and radio, and CMOS solar cells in the same fabrication process.

While much has been accomplished towards the goal of making autonomous jumping microrobots, they still remain elusive. It is the author's hope that this dissertation serves as a starting place and guide for researchers continuing to work towards this goal.

Bibliography

[1] Craig W Reynolds. "Flocks, Herds and Schools: A Distributed Behavioral Model". In: *Proceedings of the 14th annual conference on Computer graphics and interactive techniques*. 1987, pp. 25–34.

[2] Michael Rubenstein, Christian Ahler, and Radhika Nagpal. "Kilobot: A Low Cost Scalable Robot System for Collective Behaviors". In: *2012 IEEE International Conference on Robotics and Automation*. IEEE. 2012, pp. 3293–3298.

[3] Andrew P Sabelhaus, Daniel Mirsky, L Maxwell Hill, Nuno C Martins, and Sarah Bergbreiter. "TinyTeRP: A Tiny Terrestrial Robotic Platform with modular sensing". In: *2013 IEEE International Conference on Robotics and Automation*. IEEE. 2013, pp. 2600–2605.

[4] Justin Werfel, Kirstin Petersen, and Radhika Nagpal. "Designing Collective Behavior in a Termite-inspired Robot Construction Team". In: *Science* 343.6172 (2014), pp. 754–758.

[5] Justin Y Kim, Tyler Colaco, Zendai Kashino, Goldie Nejat, and Beno Benhabib. "mROBerTO: A Modular Millirobot for Swarm-behavior Studies". In: *2016 IEEE/RSJ International Conference on Intelligent Robots and Systems (IROS)*. IEEE. 2016, pp. 2109–2114.

[6] Mathieu Le Goc, Lawrence H Kim, Ali Parsaei, Jean-Daniel Fekete, Pierre Dragicevic, and Sean Follmer. "Zooids: Building blocks for swarm user interfaces". In: *Proceedings of the 29th Annual Symposium on User Interface Software and Technology*. 2016, pp. 97–109.

[7] Richard P Feynman. "There's Plenty of Room at the Bottom". In: *California Institute of Technology, Engineering and Science magazine* (1960).

[8] Anita M Flynn. "Gnat Robots (And How They Will Change Robotics)". In: (1987).

[9] Anita M Flynn, Rodney A Brooks, and LS Tavrow. "Twilight Zones and Cornerstones". In: *Massachusetts Institute of Technology, Cambridge, MA* (1989).

[10] Richard Feynman. "Infinitesimal Machinery". In: *Journal of Microelectromechanical Systems* 2.1 (1993), pp. 4–14.

[11] Sarah Bergbreiter and Kristofer SJ Pister. "Design of an Autonomous Jumping Microrobot". In: *Proceedings 2007 IEEE International Conference on Robotics and Automation*. IEEE. 2007, pp. 447–453.

[12] Wayne A Churaman, Aaron P Gerratt, and Sarah Bergbreiter. "First Leaps Toward Jumping Microrobots". In: *2011 IEEE/RSJ International Conference on Intelligent Robots and Systems*. IEEE. 2011, pp. 1680–1686.

[13] Minkyun Noh, Seung-Won Kim, Sungmin An, Je-Sung Koh, and Kyu-Jin Cho. "Flea-inspired Catapult Mechanism for Miniature Jumping Robots". In: *IEEE Transactions on Robotics* 28.5 (2012), pp. 1007–1018.

[14] Joseph T. Greenspun and Kristofer S. J. Pister. "First Leaps of an Electrostatic Inchworm Motor-Driven Jumping Microrobot". In: *2018 Hilton Head Solid-State Sensors, Actuators and Microsystems Workshop*. 2018.

[15] Palak Bhushan and Claire Tomlin. "An Insect-scale Untethered Laser-powered Jumping Microrobot". In: *arXiv preprint arXiv:1908.03282* (2019).

[16] Craig B Schindler, Joseph T Greenspun, Hani C Gomez, and Kristofer SJ Pister. "A Jumping Silicon Microrobot With Electrostatic Inchworm Motors and Energy Storing Substrate Springs". In: *2019 20th International Conference on Solid-State Sensors, Actuators and Microsystems & Eurosensors XXXIII (TRANSDUCERS & EUROSENSORS XXXIII)*. IEEE. 2019, pp. 88–91.

[17] Seth Hollar, Anita Flynn, Colby Bellew, and KSJ Pister. "Solar Powered 10 mg Silicon Robot". In: *The Sixteenth Annual International Conference on Micro Electro Mechanical Systems, 2003. MEMS-03 Kyoto. IEEE*. IEEE. 2003, pp. 706–711.

[18] Bruce R Donald, Christopher G Levey, Craig D McGray, Igor Paprotny, and Daniela Rus. "An untethered, electrostatic, globally controllable MEMS micro-robot". In: *Journal of microelectromechanical systems* 15.1 (2006), pp. 1–15.

[19] Ken Saito, Minami Takato, Yoshifumi Sekine, and Fumio Uchikoba. "Biomimetics micro robot with active hardware neural networks locomotion control and insect-like switching behaviour". In: *International Journal of Advanced Robotic Systems* 9.5 (2012), p. 226.

[20] Dana Vogtmann, Ryan St Pierre, and Sarah Bergbreiter. "A 25 mg magnetically actuated microrobot walking at$>$ 5 body lengths/sec". In: *2017 IEEE 30th International Conference on Micro Electro Mechanical Systems (MEMS)*. IEEE. 2017, pp. 179–182.

[21] Daniel S Contreras, Daniel S Drew, and Kristofer SJ Pister. "First Steps of a Millimeter-Scale Walking Silicon Robot". In: *2017 19th International Conference on Solid-State Sensors, Actuators and Microsystems (TRANSDUCERS)*. IEEE. 2017, pp. 910–913.

[22] Daniel S Contreras and Kristofer SJ Pister. "A Six-Legged MEMS Silicon Robot Using Multichip Assembly". In: *Hilton Head Workshop*. 2018.

[23] Kevin Y Ma, Pakpong Chirarattananon, Sawyer B Fuller, and Robert J Wood. "Controlled Flight of a Biologically Inspired, Insect-scale Robot". In: *Science* 340.6132 (2013), pp. 603–607.

[24] Daniel S Drew, Nathan O Lambert, Craig B Schindler, and Kristofer SJ Pister. "Toward Controlled Flight of the Ionocraft: A Flying Microrobot Using Electrohydrodynamic Thrust with Onboard Sensing and No Moving Parts". In: *IEEE Robotics and Automation Letters* 3.4 (2018), pp. 2807–2813.

[25] Noah T Jafferis, E Farrell Helbling, Michael Karpelson, and Robert J Wood. "Untethered Flight of an Insect-sized Flapping-wing Microscale Aerial Vehicle". In: *Nature* 570.7762 (2019), pp. 491–495.

[26] Johannes James, Vikram Iyer, Yogesh Chukewad, Shyamnath Gollakota, and Sawyer B Fuller. "Liftoff of a 190 mg Laser-powered Aerial Vehicle: The Lightest Wireless Robot to Fly". In: *2018 IEEE International Conference on Robotics and Automation (ICRA)*. IEEE. 2018, pp. 1–8.

[27] HC Bennet-Clark and ECA Lucey. "The jump of the flea: a study of the energetics and a model of the mechanism". In: *Journal of Experimental Biology* 47.1 (1967), pp. 59–76.

[28] Miriam Rothschild, Y Schlein, K Parker, C Neville, and S Sternberg. "The Flying Leap of the Flea". In: *Scientific American* 229.5 (1973), pp. 92–101.

[29] Miriam Louisa Rothschild, J Schlein, K Parker, C Neville, and S Sternberg. "The jumping mechanism of Xenopsylla cheopis III. Execution of the jump and activity". In: *Philosophical Transactions of the Royal Society of London. B, Biological Sciences* 271.914 (1975), pp. 499–515.

[30] G Hoyle. "Changes in the blood potassium concentration of the African migratory locust (Locusta migratoria migratorioides R. & F.) during food deprivation, and the effect on neuromuscular activity". In: *Journal of Experimental Biology* 31.2 (1954), pp. 260–270.

[31] G Hoyle. "Neuromuscular mechanisms of a locust skeletal muscle". In: *Proceedings of the Royal Society of London. Series B-Biological Sciences* 143.912 (1955), pp. 343–367.

[32] ASTM International. "G173-03-Standard Tables for Reference Solar Spectral Irradiances: Direct Normal and Hemispherical on 37° Tilted Surface". In: *Annual Book of ASTM Standards 2003* 14.04 (2012).

[33] Aminy E Ostfeld, Abhinav M Gaikwad, Yasser Khan, and Ana C Arias. "High-performance Flexible Energy Storage and Harvesting System for Wearable Electronics". In: *Scientific reports* 6 (2016), p. 26122.

[34] Jan S. Rentmeister, Kristofer S. J. Pister, and Jason T. Stauth. "A 120-330V, sub-μA, Optically Powered Microrobotic Drive IC for DARPA SHRIMP". In: *GOMACTech 2020*. 2020.

[35] Filip Maksimovic, Brad Wheeler, David C Burnett, Osama Khan, Sahar Mesri, Ioana Suciu, Lydia Lee, Alex Moreno, Arvind Sundararajan, Bob Zhou, et al. "A Crystal-Free Single-Chip Micro Mote with Integrated 802.15. 4 Compatible Transceiver, sub-mW BLE Compatible Beacon Transmitter, and Cortex M0". In: *2019 Symposium on VLSI Circuits*. IEEE. 2019, pp. C88–C89.

[36] Allen Cowen, Greg Hames, DeMaul Monk, Steve Wilcenski, and Busbee Hardy. *SOIMUMPs Design Handbook, Revision 8.0*. Available at `http://www.memscap.com/__data/assets/pdf_file/0019/1774/SOIMUMPs.dr.v8.0.pdf`. Accessed 2020/01/08.

[37] *XFAB SOI Process Technologies*. `https://www.xfab.com/technology/soi/`. Accessed: 2020-03-24.

[38] Colby L Bellew, Seth Hollar, and KSJ Pister. "An SOI Process for Fabrication of Solar Cells, Transistors and Electrostatic Actuators". In: *TRANSDUCERS'03. 12th International Conference on Solid-State Sensors, Actuators and Microsystems. Digest of Technical Papers (Cat. No. 03TH8664)*. Vol. 2. IEEE. 2003, pp. 1075–1078.

[39] Kurt E Petersen. "Silicon as a Mechanical Material". In: *Proceedings of the IEEE* 70.5 (1982), pp. 420–457.

[40] Joseph Greenspun. "Mechanical Energy Storage for Self-Destructing Motes and Jumping Microrobots". PhD thesis. EECS Department, University of California, Berkeley, Aug. 2018. URL: `http://www2.eecs.berkeley.edu/Pubs/TechRpts/2018/EECS-2018-112.html`.

[41] Matthew A Hopcroft, William D Nix, and Thomas W Kenny. "What is the Young's Modulus of Silicon?" In: *Journal of microelectromechanical systems* 19.2 (2010), pp. 229–238.

[42] John Gosline, Margo Lillie, Emily Carrington, Paul Guerette, Christine Ortlepp, and Ken Savage. "Elastic proteins: biological roles and mechanical properties". In: *Philosophical Transactions of the Royal Society of London. Series B: Biological Sciences* 357.1418 (2002), pp. 121–132.

[43] Stephen D Senturia. *Microsystem Design*. Springer Science & Business Media, 2007.

[44] Sarah Elizabeth Bergbreiter. "Autonomous Jumping Microrobots". PhD thesis. EECS Department, University of California, Berkeley, Dec. 2007. URL: `http://www2.eecs.berkeley.edu/Pubs/TechRpts/2007/EECS-2007-159.html`.

[45] Henry C Bennet-Clark and GM Alder. "The effect of air resistance on the jumping performance of insects". In: *Journal of Experimental Biology* 82.1 (1979), pp. 105–121.

[46] Bruce R. Munson, Donald F. Young, Theodore H. Okiishi, and Wade W. Huebsch. *Fundamentals of Fluid Mechanics. Sixth Edition*. Wiley, 2009.

[47] I Penskiy and S Bergbreiter. "Optimized Electrostatic Inchworm Motors Using a Flexible Driving Arm". In: *Journal of Micromechanics and Microengineering* 23.1 (2012), p. 015018.

[48] Richard Yeh, Seth Hollar, and Kristofer SJ Pister. "Single mask, large force, and large displacement electrostatic linear inchworm motors". In: *Journal of Microelectromechanical Systems* 11.4 (2002), pp. 330–336.

[49] Daniel S Contreras and Kristofer SJ Pister. "Dynamics of electrostatic inchworm motors for silicon microrobots". In: *2017 International Conference on Manipulation, Automation and Robotics at Small Scales (MARSS)*. IEEE. 2017, pp. 1–6.

[50] Daniel Contreras. "Walking Silicon: Actuators and Legs for Small-Scale Terrestrial Robots". PhD thesis. EECS Department, University of California, Berkeley, May 2019. URL: `http://www2.eecs.berkeley.edu/Pubs/TechRpts/2019/EECS-2019-18.html`.

[51] Craig B Schindler, Hani C Gomez, Dillon Acker-James, Daniel Teal, Wei Li, and Kristofer SJ Pister. "15 Millinewton Force, 1 Millimeter Displacement, Low-Power MEMS Gripper". In: *2020 IEEE 33rd International Conference on Micro Electro Mechanical Systems (MEMS)*. IEEE. 2020, pp. 485–488.

[52] Richard Yeh. "Articulated Mechanisms and Electrostatic Actuators for Autonomous Microrobots". PhD thesis. EECS Department, University of California, Berkeley, 2001.

[53] Steffen Paul, Andreas M Schlaffer, and Josef A Nossek. "Optimal Charging of Capacitors". In: *IEEE Transactions on Circuits and Systems I: Fundamental Theory and Applications* 47.7 (2000), pp. 1009–1016.

[54] Peter M Osterberg and Stephen D Senturia. "M-TEST: a test chip for MEMS material property measurement using electrostatically actuated test structures". In: *Journal of Microelectromechanical systems* 6.2 (1997), pp. 107–118.

[55] Minhang Bao and Heng Yang. "Squeeze film air damping in MEMS". In: *Sensors and Actuators A: Physical* 136.1 (2007), pp. 3–27.

[56] Frédéric Marty, Lionel Rousseau, Bassam Saadany, Bruno Mercier, Olivier Français, Yoshio Mita, and Tarik Bourouina. "Advanced etching of silicon based on deep reactive ion etching for silicon high aspect ratio microstructures and three-dimensional micro-and nanostructures". In: *Microelectronics journal* 36.7 (2005), pp. 673–677.

[57] Yemin Tang, Amin Sandoughsaz, Kevin J Owen, and Khalil Najafi. "Ultra Deep Reactive Ion Etching of High Aspect-Ratio and Thick Silicon Using a Ramped-Parameter Process". In: *Journal of Microelectromechanical Systems* 27.4 (2018), pp. 686–697.

[58] Robert J Dufresne, William J Gerace, and William J Leonard. "Springbok: The Physics of Jumping". In: *The Physics Teacher* 39.2 (2001), pp. 109–115.

[59] Hani C Gomez, Craig B Schindler, Harry L Clark, Joseph T Greenspun, and Kristofer SJ Pister. "Zero Insertion Force MEMS Socket: 3d Multi-Chip Assembly for Microrobotics". In: *2019 20th International Conference on Solid-State Sensors, Actuators and Microsystems & Eurosensors XXXIII (TRANSDUCERS & EUROSENSORS XXXIII)*. IEEE. 2019, pp. 1732–1735.

Appendix A

Three Mask Silicon-On-Insulator (SOI) Process Flow

The starting substrate is a silicon-on-insulator wafer with a 40μm silicon device layer, a 2μm buried oxide layer, and a 550μm silicon substrate. The wafer has a (100) surface and <110> flat. The device layer silicon and substrate silicon have a resistivity of 10-20 Ω-cm. The following is the list of design rules for the process. Features drawn in the METAL mask will remain. Features drawn in SOI mask will remain. Features drawn in TRENCH mask will be etched.

1. METAL
    a) 2μm minimum line and space
    b) No metal allowed on top of device silicon that will subsequently be etched during DRIE of the SOI mask
    c) Metal must be at least 5μm away from the edge of a device feature
2. SOI
    a) 2μm minimum line and space
    b) 30% maximum exposed area
    c) Structures less than 10μm in width guaranteed to be released
    d) Structures greater than 50μm × 50μm guaranteed to be anchored
3. TRENCH
    a) Option 1: 200μm minimum line and space
        i. Any line and space is allowed so long as it is greater than or equal to 200μm
        ii. 30% maximum exposed area
        iii. <5μm center-to-center alignment between SOI and TRENCH features

iv. Possible offset of up to 30μm between SOI and TRENCH patterns on the SOI side

v. A checkerboard pattern should be used when exposing die to reduce the total exposed area on the wafer

b) Option 2: 40μm line and 40μm minimum space

i. Only 40μm lines (trenches) are allowed, but any space is allowed so long as it is greater than or equal to 40μm

ii. 10% maximum exposed area

iii. <5μm center-to-center alignment between SOI and TRENCH features

iv. Possible offset of up to 20μm between SOI and TRENCH patterns on the SOI side

v. The entire wafer can be exposed with die

All fabrication was done at the Marvell Nanofabrication Laboratory on the University of California, Berkeley campus. The following is the full list of the process steps.

1. **Picotrack Coater System (Picotrack1):** Deposit 1.2μm of OiR906-12 i-line resist onto the device layer using recipe T1_OiR906_1.2um.

2. **GCA8500 6" Wafer Stepper (gcaws6):** Expose the photoresist for 1.2s with mask METAL.

3. **Picotrack Developer System (Picotrack2):** Develop the photoresist with MF26A developer using recipe T2_PEB120C60s_MF26A60s.

4. **CHA Solution E-Beam Evaporator (cha):** Deposit 50nm of chromium and 500nm of gold.

5. **ASAP-Liftoff M6100 (asap-liftoff):** Liftoff photoresist with recipe 17. Run the recipe twice to make sure all photoresist is removed.

6. **Picotrack Coater System (Picotrack1):** Deposit 1.2μm of OiR906-12 i-line resist onto the device layer using recipe T1_OiR906_1.2um.

7. **GCA8500 Wafer 6" Stepper (gcaws6):** Expose the photoresist for 1.2s with mask SOI.

8. **Picotrack Developer System (Picotrack2):** Develop the photoresist with MF26A developer using recipe T2_PEB120C60s_MF26A60s.

9. **Fusion M200PCU Photostabilizer System (axcelis):** UV hardbake the developed photoresist using recipe “J.”

10. **Surface Technology Systems Advanced Silicon Etch (sts2):** Etch the wafer with high frequency recipe CBSCHIND_HF_6_STEPS until the field is visibly cleared. The color of the features in the field visibly change when looking through the tool eyepiece above the wafer once the etch reaches the oxide. The field will clear first at the edges of the wafer, and then the etch front will move radially towards the center. Once the etch front reaches the center of the wafer, manually terminate the etch. Then, etch the wafer with low frequency recipe CBSCHIND_LF_5_STEPS for half the number of cycles that were required to fully clear the field.

11. **Plasma-Therm Parallel Plate Etcher (ptherm):** Ash photoresist using an O_2 plasma at 80 sccm and 200W for 5 minutes.

12. **OPTIONAL STEP — Oxford Plasmalab System 100 PECVD System (oxfordpecvd3 or oxfordpecvd4):** Deposit approximately 1μm of oxide to protect the device silicon features during the backside lithography and etching steps to follow. Normally this fabrication step was skipped and the device silicon features remained perfectly intact at the end of the fabrication process.

13. **Picotrack Coater System (Picotrack1):** Deposit 12μm of AZ 4620 resist onto the backside substrate using recipe T1_AZ4620_12.0um. Modify the recipe flow so that no edge bead removal is performed, and increase the soft bake time to 200s.

14. **Karl Suss MA6 Mask Aligner (ksaligner):** Expose the photoresist with mask TRENCH. Tool settings: soft contact, 90μm offset, 8.5s exposure, 3 exposures, 30s wait between exposures.

15. **Picotrack Developer System (Picotrack2):** Develop the photoresist with MF26A developer using recipe T2_NoPEB_MF26A2x60s_2Spray. Modify the recipe flow so that four 60s sprays are used (instead of the default two 60s sprays).

16. **Oven:** Hard bake resist at 120C for 60 minutes.

17. Place wafer on a wipe with the device layer facing up. Apply a thin layer (approximately 0.2mm thick) of cool grease around the outer perimeter of the wafer where there are no exposed die, as shown in Fig. A.1. Place an oxidized dummy wafer (with approximately 1μm thermal oxide) on top of the device wafer (the polished side of the dummy wafer should be in contact with the device layer of the device wafer). Place an aluminum sheet on top of a hot plate and then place the wafer stack on top of the aluminum sheet with the photoresist facing upwards. Place a wipe on top of the wafer stack, and then place a weight on top of the wipe. Heat at 55C for 20 minutes.

18. **Surface Technology Systems Advanced Silicon Etch (sts2):** Put the wafer stack into the tool. Etch the wafer with high frequency recipe CBSCHIND_HF_6_STEPS until the field is visibly cleared. If etching less than approximately 200μm features, it is

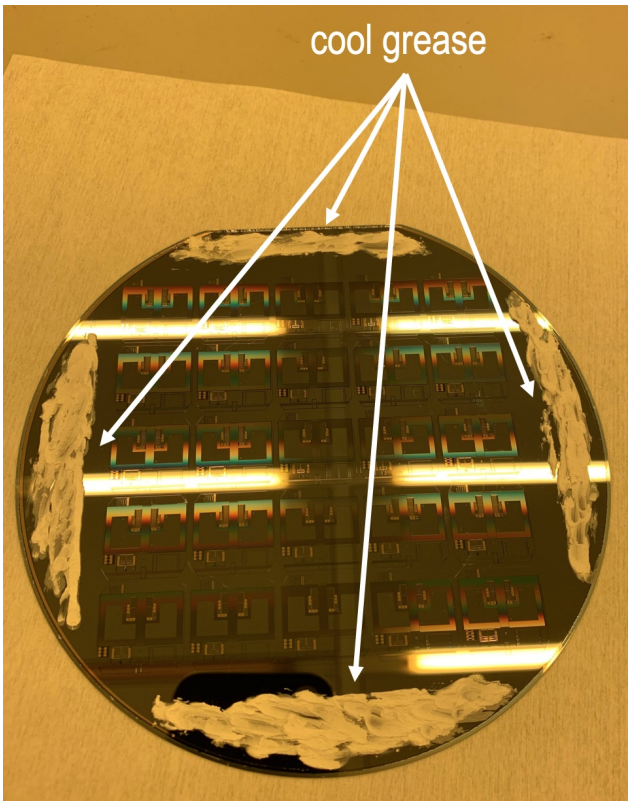

Figure A.1: Cool grease being applied to the device side of a 150mm SOI wafer before it is bonded to an oxidized dummy wafer.

not possible to visually watch the field clear. In this case, the wafer must be removed every so often to monitor the etch depth under a microscope.

19. **Technics C Plasma Etching System (technics-c):** Put the wafer stack into the tool. Ash photoresist using an O_2 plasma at 180 mTorr of pressure and 300W for 30 minutes.

20. **uEtch HF Vapor Release System (primaxx):** Remove chiplets from the wafer stack. If very small trenches are used to singulate the chiplets ($<200\mu$m), the wafer stack may first need to be delaminated. If delaminating the device wafer from the dummy wafer, be careful not to shatter the device wafer by exerting too much torque when trying to separate the wafers. Sliding a razor blade between the wafers is a good strategy for delaminating the wafer stack. Heat chiplets on the primaxx hotplate at 250C for 2 minutes. Make sure the primaxx valve needle (under the hood) is set to 5.5. Place the chiplets on the primaxx hotplate. Use 8 cycles of RECIPE3 with stabilize=120, etch=240, and pump=300. This recipe will laterally etch approximately 8μm of oxide, and was used to release beams less than 10μm in width or structures larger than $50\mu\text{m} \times 50\mu$m with 8μm wide and 14μm center-to-center etch holes.